UNIVERSITÀ DEGLI STUDI DI CATANIA

Dipartimento di Scienze Biologiche, Geologiche e Ambientali, Sezione Scienze della Terra

DOTTORATO DI RICERCA IN GEODINAMICA E SISMOTETTONICA
CICLO XXV

CRUSTAL STRUCTURE AND DYNAMICS IN SOUTHEASTERN SICILY (ITALY) BY USING SEISMOLOGICAL DATA

Dott.ssa Carla Musumeci

Coordinatore

Prof. Carmelo Monaco

Tutor

Prof. Stefano Gresta

Co-tutor

Prof. Stefano Catalano

DICEMBRE 2012

“Un vincitore è semplicemente un sognatore che non si è mai arreso.”

“A winner is just a dreamer who never gave up.”

Nelson Mandela

Table of Contents

Abstract

Introduction: Through receiver function analysis, this study inquires into some of the most basic properties of the crust below southeastern Sicily (Italy), mostly represented by the Hyblean Plateau. *Method*: This is accomplished, using P-to-S receiver function (P-RF) technique which involves coordinate rotation and deconvolution, by stacking waveforms from 335 teleseismic events, magnitude 6.0 and larger, to determine the delay in arrival time for several phases of the P-wave coda, relative to the initial P-wave arrival. This information is used to establish a linear relationship between thickness and V_P/V_S ratio, each of which is stacked using the slant stacking approach for a given station to identify the best-fit thickness and wave speed for the crust below that station. To determine their accuracy these results are compared with previous studies, as well as with synthetically generated receiver functions based on 1D crustal models including dipping layers. *Results*: The good regional coverage and the fairly dense station spacing (~20 km) leaded to a fairly complete image of the crust-mantle boundary over the entire region that shows strong lateral variations of the crustal thickness with Moho depth varying between 29 and 38 km. In particular, a thinner crust is observed in the central-eastern part of the Hyblean Foreland beneath SSY (Solarino) station and thickening further to the south beneath HMDC (Modica) station (up to 38 km) and to the north beneath HLNI (Lentini) station (up to 35 km). Sharp transitions between thinned and thickened crust are most likely the result of complicated 3D structures attributed to regional geodynamics. *Discussion*: Since all the 8 considered broadband stations lie in a geodinamically complex area, reliable estimates of the crustal thicknesses below these stations are key requisite for understanding the geologic and tectonic processes that have been dominant in the region, providing valuable information for the numerous earth science disciplines.

Chapter 1

Introduction

The structure of the Earth's interior is fairly well known from seismology, and knowledge of the fine structure is improving continuously. Seismology not only provides the structure, but also gives information about the composition, crystal structure or mineralogy and physical state.

Earth is conventionally divided into several distinct layers (crust, mantle and core), considered as a system of horizontal layers affecting the seismic energy arriving at a given station (**Fig. 1**). Only the uppermost part of the crust is available for direct sampling from boreholes. At greater depths all information about its composition and structure is indirect.

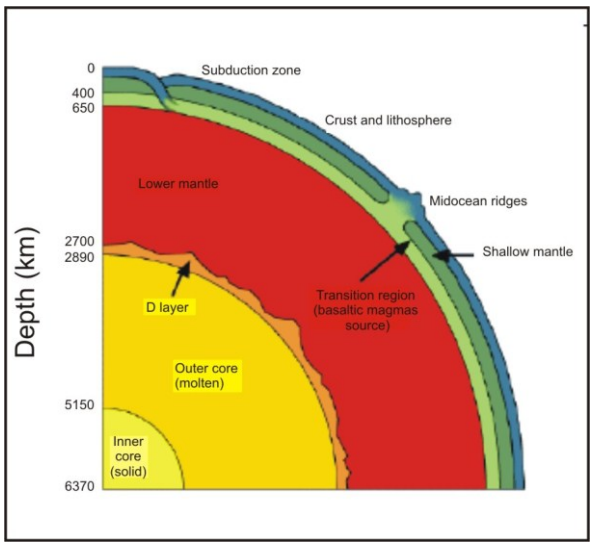

Fig. 1- *Simplified structure model of the Earth*.

Much of the information about the Earth's interior has been derived from the knowledge of the variation of seismic velocities with depth. Consequently, the recorded motion at the earth's surface depends on the elastic parameters, the thickness of these layers, as well as on the existing seismic energy and the recording instrument.

The reconstruction of the Earth's interior, from geophysical observables recorded at the surface, is called an 'inverse problem'. Inverse problem theory has been widely developed in geophysics from earthquakes locations to seismic tomography (Tarantola, 1987; Zhang and Thurber, 2003). One of these inverse problems is the reconstruction of a vertical profile of the elastic properties at depth under a seismic station using P-to-S converted phases generated at subsurface discontinuities (Langston, 1979). With regard

to this, receiver functions (RFs) are time series that contain P-to-S phases, and are computed from teleseismic recordings through the deconvolution of the vertical component of a teleseismic waveform from the horizontal ones. The solution of the RF inverse problem involves locating subsurface seismic discontinuities, reconstructing the elastic properties in the subsurface, and estimating the uncertainties associated with these quantities (Piana Agostinetti and Malinverno, 2010).

The first accurate teleseismic recording was obtained in 1889 in Potsdam (Germany), 15 minutes after an earthquake in Japan (von Rebeur-Paschwitz, 1889), while the beginning of the systematic collection of global seismic data was started in 1892 by John Milne (Milne, 1895). Teleseismic body waves have been used extensively for a long time to retrieve crustal and lithospheric structures beneath recording stations (Phinney, 1964) under the name of 'Crustal Transfer Method'. The method has been subsequently improved by several workers (e.g. Burdick and Langston, 1977; Owens et alii, 1984). It is now commonly referred to as the 'Receiver Function Method', one of the most widely used technique to determine the crustal structure on a regional scale below the recording stations. For this reason, teleseismic receiver functions have been often used to locally determine depth and dip of crustal and upper mantle discontinuities for peninsular Italy (Piana Agostinetti et alii, 2002; Mele and Sandvol, 2003; Lucente et alii, 2005; Margheriti et alii, 2006; Piana Agostinetti and Amato, 2009; Miller and Piana Agostinetti, 2012). Southeastern Sicily, one of the most seismically active areas of the Mediterranean Basin, is poorly covered by these studies. The complex tectonic history and the active tectonics of this region motivated the present research to look at the crustal structure beneath single seismic stations, to infer some more elements useful for geodynamic reconstructions and to infer any correlation between the deeper structure and the surface tectonics. Specifically, the research of this PhD project consisted in the application of the P-to-S receiver function (P-RF) analysis technique to investigate the crustal thickness in southeastern Sicily (Italy), in order to increase the spatial resolution of the Moho maps of the region. This study considered seismograms recorded at 8 broadband stations, deployed in the investigated area, all of which are part of the seismic permanent network currently operated by the Istituto Nazionale di Geofisica e Vulcanologia (INGV, Osservatorio Etneo, Sezione di Catania). These stations overlie several interesting geological provinces in the region, covering Recent Quaternary deposits, Plio-Pleistocene Hyblean volcanics, Appennine-Maghrebian units and Meso-Cenozoic carbonate sediments. Estimates of crustal thickness below these stations are

useful in characterizing the "topography" of the crust-mantle interface, key requisite for geodynamic modelling, for understanding the evolution and state of lithosphere, enhancing the understanding of how ancient tectonic events continue to shape and define the structure of our continent.

Firstly, all previous studies in the area have been reviewed in details to give a starting point to the analysis and to better define the previous knowledge about the seismic structure in this region. Then, the results are discussed, comparing them with previous findings and discussing some original implications for the geological evolution. In particular this manuscript is organized as follows:

- Chapter 2 summarizes the geological and tectonic setting of the investigated area, whose knowledge is important for successive correlations with the analysis results. Instrumental and historical seismicity are also presented in this chapter and the previous geophysical studies are briefly introduced.
- Chapter 3 discusses the receiver function method and describes the different steps of data processing.
- Chapter 4 introduces the dataset. Here, data examples are presented, as well.
- Chapter 5 shows the results in terms of crustal thickness.
- Chapter 6 presents the concluding remarks of this research and the critical conclusions are here discussed. Additional information on the selected events are in Appendix A.

Chapter 2

2.1 Geological Setting of Southeastern Sicily

From a geological point of view, southeastern Sicily is an area of great interest because: 1) it represents an important piece of the collision front between Nubia and Eurasia; 2) it is very close to the biggest European volcano Mount Etna and, 3) it has been hit by strong earthquakes in the past (1169, 1542 and 1693) that struggled the cities of Catania, Siracusa and Ragusa provoking tens of thousands of casualties.

Its geological-structural setting must be considered in the frame of the complex tectonic features of the Mediterranean basin, which is dominated by the ~N20°W Neogene-Quaternary convergence between Nubian plate (the African plate west of the East African Rift) and Eurasia, occurred in the last 100 million years (Faccenna et alii, 2001). Tectonic forces resulting from the relative movements among these plates are transferred into the continental crust, where large structures, as subduction thrusts, major faults and normal detachments, accommodate most of the strain and produce nearly all of the most destroying earthquakes. Regionally speaking, in the whole region of Sicily we may distinguish a northern imbricate mountain chain (Appenninic-Magrebian Chain or Maghrebian Thrust Belt), a deep Neogene basin filled with nappes (Caltanissetta Basin) and a relatively stable carbonate platform to the southeast (Hyblean Plateau) (**Fig. 2**). The evolution of these units can be correlated with two main tectonic phases: (i) a mid Triassic to Cretaceous extensional phase, related to Tethyan rifting; (ii) a Tertiary to recent compressional phase during which the Sicilian segment of the North African continental margin has been affected by continental collision. The extension created horst/graben platforms and basins which were subsequently deformed and overthrusted during the later compressional phase (Catalano et alii, 2010).

Southeastern Sicily is mostly represented by the Hyblean Plateau, a distinct crustal unit located at the northeastern end of the mostly submerged Pelagian Block (Burollet et alii, 1978). The autochthonous sedimentary wedge (about 7 km thick) overlies an "African" continental crust and consists of thick Triassic-Liassic platform and slope-to-basin carbonates, overlain by Jurassic-Eocene pelagic carbonates and Tertiary open shelf clastic deposits (Patacca et alii, 1979; Bianchi et alii, 1987; Grasso et alii, 2004), with intercalated Plio-Pleistocene mafic volcanics at several distinct intervals (Grasso et alii, 1983). Its crustal structure and gravimetric and magnetic anomalies differ from those of adjacent areas of the African Foreland. At the present, the plateau plays the role of a crustal indenter that, confined between the flexured continental thinned-crust area

of the Caltanissetta Basin, to the west, and the oceanic domains of the Ionian Basin (Finetti and Del Ben, 1996), to the east, has impinged against the front of the Maghrebian Thrust Belt (**Fig. 2**).

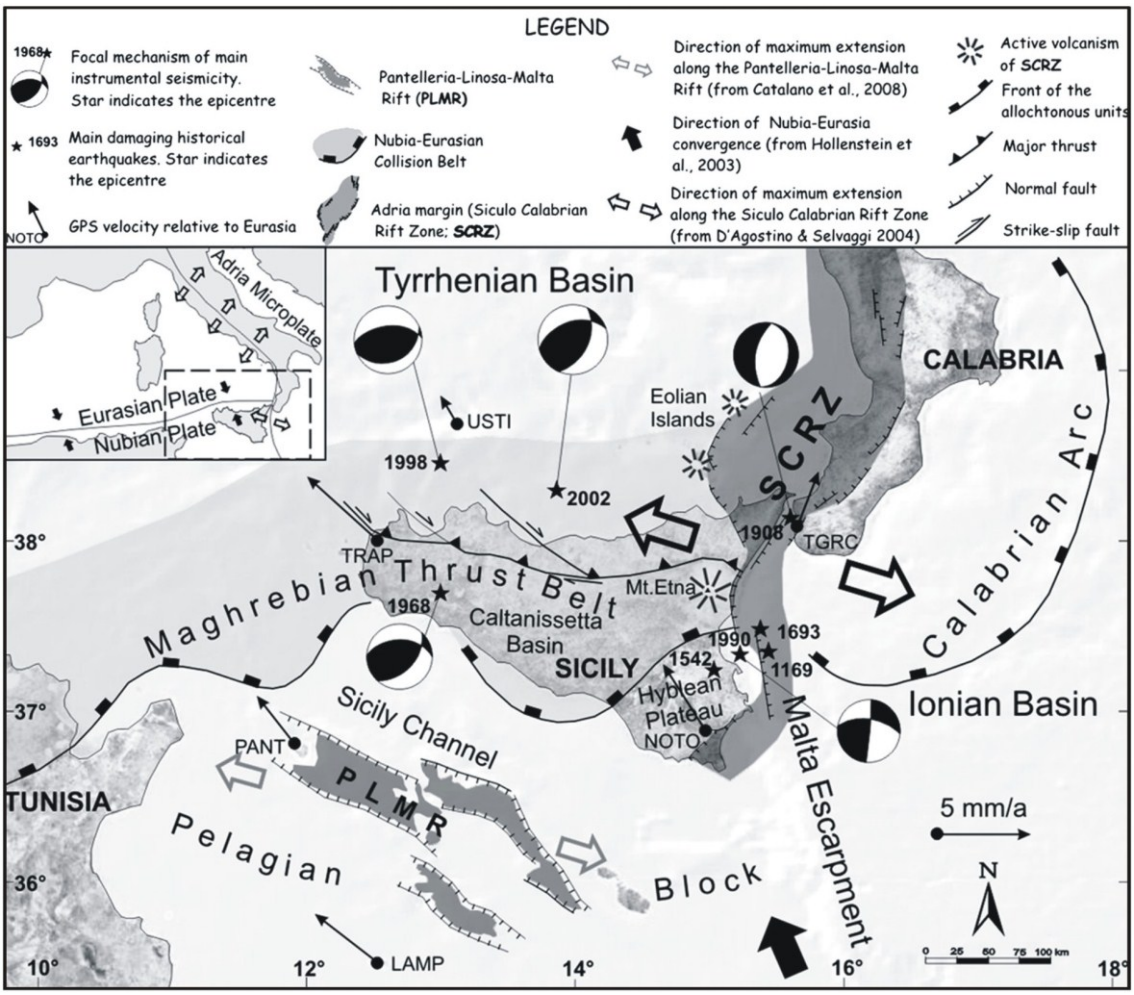

Fig. 2- *Tectonic sketch map of the Central Mediterranean from Tunisia to the Calabrian arc, showing the main Quaternary fault belts and their relation with plate boundaries and incipient rift zones. The inset describes the location of the Nubia-Eurasia convergent plate boundary and of the divergent western margin of Adria. Focal mechanisms are from Anderson and Jackson (1987) and Pondrelli et alii (2002-2004) and GPS velocities are from Hollestein et alii (2003) and D'Agostino and Selvaggi (2004). (From Catalano et alii, 2010).*

The northern and western margins of the Hyblean Plateau are characterized by an older extensional belt (named Gela-Catania Foredeep), that forming a roughly NE-SW alignment, is downbent by a NE-SW fault system under the front of the Appenninic-Maghrebian Thrust Belt (Yellin-Dror et alii, 1997). This narrow and weakly deformed depression (Gela Basin) developed from the Late Pliocene onwards, as suggested by biostratigraphic analyses, and is probably related to the inflection of the carbonate

substrate due to the frontal nappe loading. The basin fill consists of Plio-Pleistocene pelagic marly limestones, and sandy clays unconformably overlying the Messinian evaporites.

To the east, the plateau is indeed bordered by the Malta Escarpment fault system (MEFS) (**Fig. 2**), one of the largest normal fault systems of the Mediterranean basin (e.g., Reuther et alii, 1993; Adam et alii, 2000). Regionally, this normal NNW-SSE trending lithospheric fault system extends from 15 to 50 km offshore and over a length of about 300 km from the eastern coast of Sicily southwards, showing a steep slope that steps down rapidly from 200 m to more than 3000 m below sea level and a width of about 40 km (Ben-Avraham et alii, 1995; Lanzafame and Bousquet, 1997). Since the late Cretaceous onset of African and Eurasian plates convergence, the Malta Escarpment fault system has been converted from a Mesozoic passive margin into a mega-hinge fault system, with an additional sinistral strike-slip component. Since the Pleistocene, sinistral strike-slip deformation and simultaneous normal faulting along this lithospheric fault system have induced the opening of oblique trending onshore grabens at the eastern margin of the Hyblean Plateau (Adam et alii, 2000). According to Bianca et alii (1999) and Azzaro and Barbano (2000), the Malta Escarpment fault system is responsible for the primary seismic activity of the region. Major historically (February 4, 1169; January 11, 1693) destructive earthquakes (M=7) occurred along this fault system (Azzaro and Barbano, 2000), causing tens of thousands of casualties. Weaker shocks (M<6) are due to secondary inland faults striking along an overall NE-SW and NNE-SSW direction (i.e., Scordia-Lentini Graben, Rosolini-Pozzallo and Scicli-Ragusa fault systems). The more recent seismicity of the area is characterized by earthquakes, with magnitudes less than M_L 4.6 (Musumeci et alii, 2005). Zones characterized by nil seismicity involve the central part of the Foreland. In depth, seismicity generally extends to about 30 km, with foci mainly concentrated from 15 to 25 km (Musumeci et alii, 2005). Earthquake focal mechanisms inferred for the study area are characterized by a predominance of normal fault-plane solutions along the Malta Escarpment, and mainly by strike-slip solutions with lesser amounts of both normal and reverse faulting in the plateau. The inversion of these fault plane solutions coherently results in stress tensors which constrain an active NW-SE to NNW-SSE oriented regional compression (Musumeci et alii, 2005).

2.2 Previous Geophysical Studies

In complex tectonics regions, seismological, geophysical and geodynamic modeling require accurate definition of the Moho geometry. Maps of the Moho topography beneath Italy have been published over the years, based on results from different geophysical methods. Morelli et alii (1967) introduced preliminary isobaths for the Moho in Europe. Geiss (1987) produced a map of the Moho topography at the Mediterranean scale, through a least square interpolation of a large number of different geophysical observations. Nicolich and Dal Piaz (1991) presented a simplified sketch map of the Moho isobaths for the Italian region, based only on controlled source seismology (CSS) data. Suhadolc and Panza (1989) and Scarascia et alii (1994) published compilation maps of the Moho isobaths for the European and Italian areas respectively, both based on revised interpretations of CSS profiles. Du et alii (1998) produced the EurID 3-D regionalized model of the European crust and mantle velocity structure including a map of the Moho depth obtained by compiling results of several CSS investigations performed in the area. Pontevivo and Panza (2002) defined the characteristics of the lithosphere-asthenosphere system in Italy based on the analysis of Rayleigh wave dispersion. Piana Agostinetti and Amato (2009) compiled the map of the Moho depth for the Italian peninsula using P receiver functions. Grad et alii (2009) produced a map of the Moho depth beneath Europe based on seismic and gravity data. Waldhauser et alii (1998) proposed a new method to determine the 3D topography and lateral continuity of seismic interfaces and a mean P wave 3D velocity model by using 2D-derived CSS reflector data. Di Stefano et alii (2011) presented a map of the 3D Moho geometry obtained by integrating high-quality CSS data and teleseismic receiver function data. Miller and Piana Agostinetti (2012) investigated the lithospheric structure using S receiver functions. Looking at southeastern Sicily, previous studies on Moho depth geometry have been documented by papers based on wide-angle DSS profiles, gravimetric modeling, deep reflection profiles, receiver function studies and seismic tomography (e.g., Scarascia et alii, 1994; Scarfì et alii, 2007; Piana Agostinetti and Amato, 2009; Miller and Piana Agostinetti, 2011). Although the main features outlined by these studies are robust, large uncertainties are whatever present in the seismic models as an effect of different acquisition and interpretation techniques and/or due to the complexities of the tectonic settings in the area of investigation. A brief review of the main results so far are given in the following sections.

2.2.1 DSS profiles

The seismic exploration method of wide angle reflection-refraction, generally known as Deep Seismic Soundings (DSS), were performed in the Italian peninsula by a cooperation of French, German, Swiss and Italian geophysical research institutions. In particular, under the sponsorship of the European Seismological Commission and the Explosion Seismology Group from 1956 to 1982 and through the European Science Foundation and the European Geotraverse from 1983 to 1989. It has to be called that the only physical parameter that can be determined (with variable accuracy) is the velocity of the P waves. Therefore, petrological and rheological models can be derived only through the assumption of hypotheses on rock composition and with the help of complementary data, like the heat flow. Furthermore, since the maximum depth of the DSS is limited to the crust-mantle boundary, little information was obtained on the continuation with depth of the tectonic structures below that limit.

A description of the techniques of acquisition and processing of the DSS data is out of the scope of this thesis and the discussion is just limited to show the different interpretations and the subsequent modifications that were brought (if they are). In particular, the crust-upper mantle structure of the southeastern Sicily was investigated by the analysis of two DSS profiles acquired during 1984. For the sake of clarity, to the DSS cross sections are assigned the same number and letters that were used in Scarascia et alii (1994) (**Fig. 3**), in Continisio et alii (1997) (**Fig. 4**) and in Cassinis et alii (2003) (**Fig. 5**).

Cross section L-L in **Fig. 3**, along the western coast of Sicily, is located between Egadi Islands and Capo Passero, and extends to the SE towards the Ionian abyssal plain. The part of the section under Sicily was explored by using shots located in the sea near Egadi, Gela and Capo Passero and recorded by land stations. The sea tract was explored with OBS and closely-spaced shots located in the Ionian Sea. The profile is characterized by significant lateral depth changes of both the Moho and the intracrustal interface (Scarascia et alii, 1994). Along the SW Sicilian coastline the thickness of the crust ranges between 35 and 40 km and the shallow layers reach a remarkable thickness (20 km).

The reconstruction of the crustal sections shown in **Fig. 4** comes from the interpretations of Continisio et alii (1997). The profile *c* (**Fig. 4**), acquired along the southern coast (DSS profile as above) crosses the Sicily in a WNW-ESE direction from Marsala on the western coast to Capo Passero on the southern one. In the Caltanissetta

trough, the Moho depth (blue line) reaches 35 km. Beneath the Hyblean Foreland the Moho rises to about 30 km. In the Hyblean Foreland, upper crust velocities of 5.4 km/s were needed for fitting the data. This feature can be accounted for by the thick sequences of rocks with large bulk moduli as those (carbonatic and volcanic) found by drill-holes in the Hyblean area (e.g. Longaretti and Rocchi, 1990).

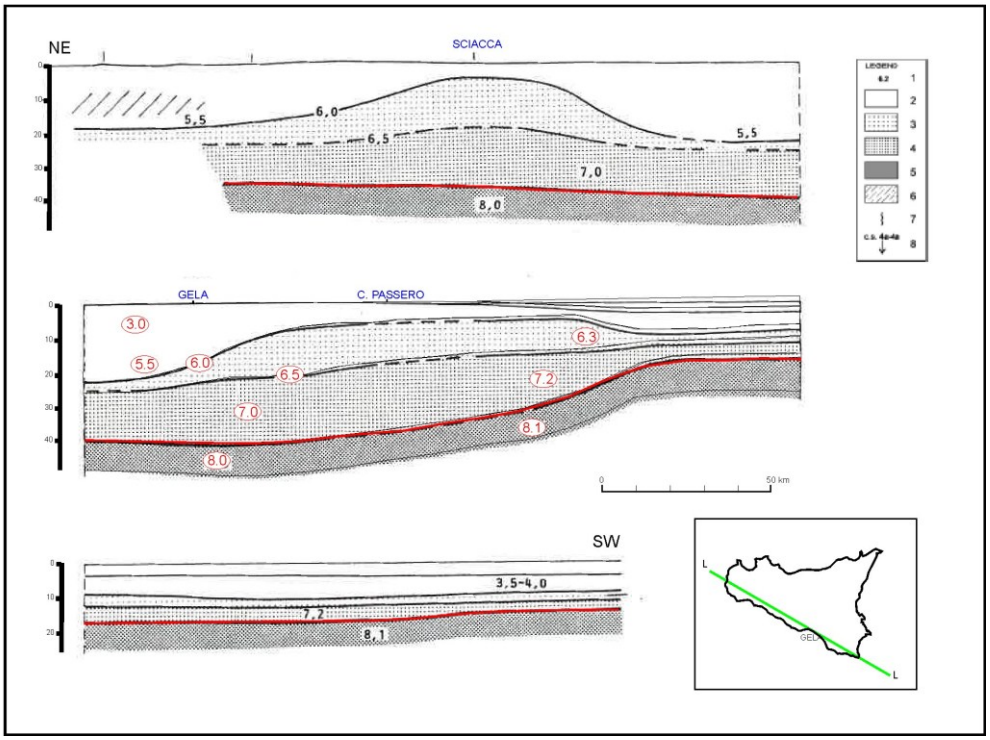

Fig. 3- *Interpretative cross-section Egadi Islands-Capo Passero-Ionian Sea. Legend: 1=Velocities in km/s; 2=Surface layers (V<6.0 km/s); 3=Upper or undifferentiated crust (V=6.0-6.5 km/s); 4=Lower crust (6.5-7.5 km/s); 5=Upper mantle (V>7.5 km/s); 6=Low velocity layers; 7=coastline. (From Scarascia et alii, 1994).*

The profile *b* (**Fig. 4**), acquired in the central Sicily (striking NNE-SSW), starts near Milazzo, on the Tyrrhenian coast, crosses the Sicilian-Maghrebian chain in the north, the Caltanissetta trough in central Sicily, and ends on the southern coast near Gela, close to the outcroppings of the Hyblean plateau. The crustal structure (Continisio et alii, 1997), is characterized by a Moho depth (red line) of less than 20 km offshore the northeastern margin of Sicily, in the Tyrrhenian sea, 30 km beneath the Peloritani chain, and 35 km in the Caltanissetta trough. In the Gela-Catania Foredeep the Moho rises to 22 km, whereas in the Hyblean Foreland it reaches 30 km. The main Moho flexure zones along the profile are located beneath each transition from one major structural domain to another (Tyrrhenian Sea-to-Chain, Chain-to-Foredeep and Foredeep-to-Foreland).

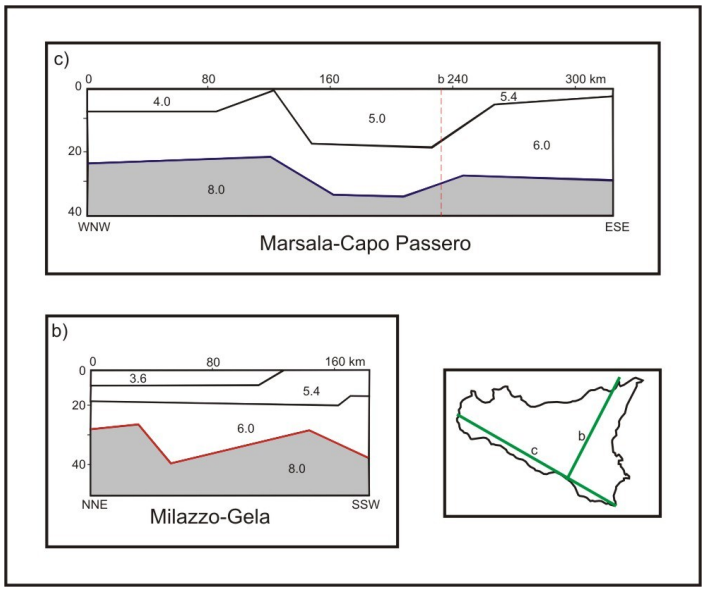

Fig. 4- *Location of the DSS profiles (b and c) and interpretative cross-sections. (From Continsio et alii, 1997).*

Recently, the processing and interpreting work was continued through new procedures (digitalization of the old analogically-recorded data, use of synthetic seismograms, seismic modeling). Thus updated interpretations of individual cross sections and more detailed maps of the Moho boundary were proposed. Section 12-12 (**Fig. 5**) from Cassinis et alii (2003) confirmed a crust-mantle discontinuity at depth of about 35-40 km beneath southeastern Sicily.

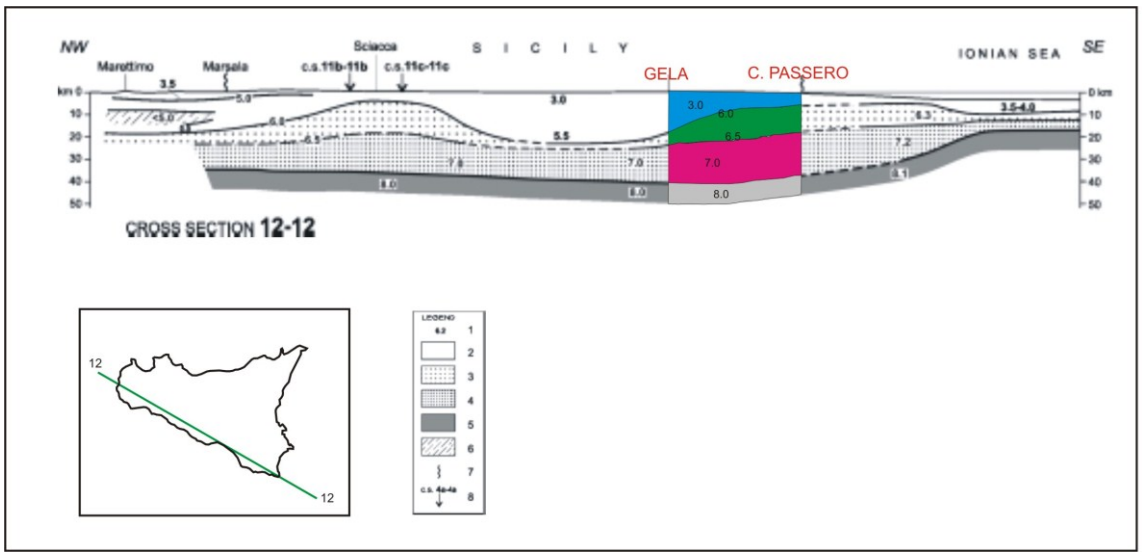

Fig. 5- *Interpretative cross-section. Legend: (1) Velocities in km/s; (2; blue) Surface layers (V<6.0 km/s);(3; green) Upper or undifferentiated crust (V=6.0-6.5 km/s); (4; fuchsia) Lower crust (6.5-7.5 km/s); (5; gray) Upper mantle (V>7.5 km/s); 6) Low velocity layers; 7) coastline. (From Cassinis et alii, 2003).*

In this image the velocity ranges that characterizes the studied area have been shaded differently: the shallower layers, with velocity below 6.0 km/s, are in blue; green area indicates layers with velocity values ranging from 6.0 to 6.5 km/s (upper crust); fuchsia area indicates layers with velocity values ranging from 6.5 to 7.5 km/s (lower crust); gray area indicates upper mantle layers, with velocity values over 7.5 km/s.

Fig. 6 shows the Moho-depth contour map obtained by the synthesis of all data available in the Italian Seas and adjacent onshore areas (Cassinis et alii, 2003). In particular, the central-southern Sicily is characterized by a total thickness ranging between 22 and 40 km.

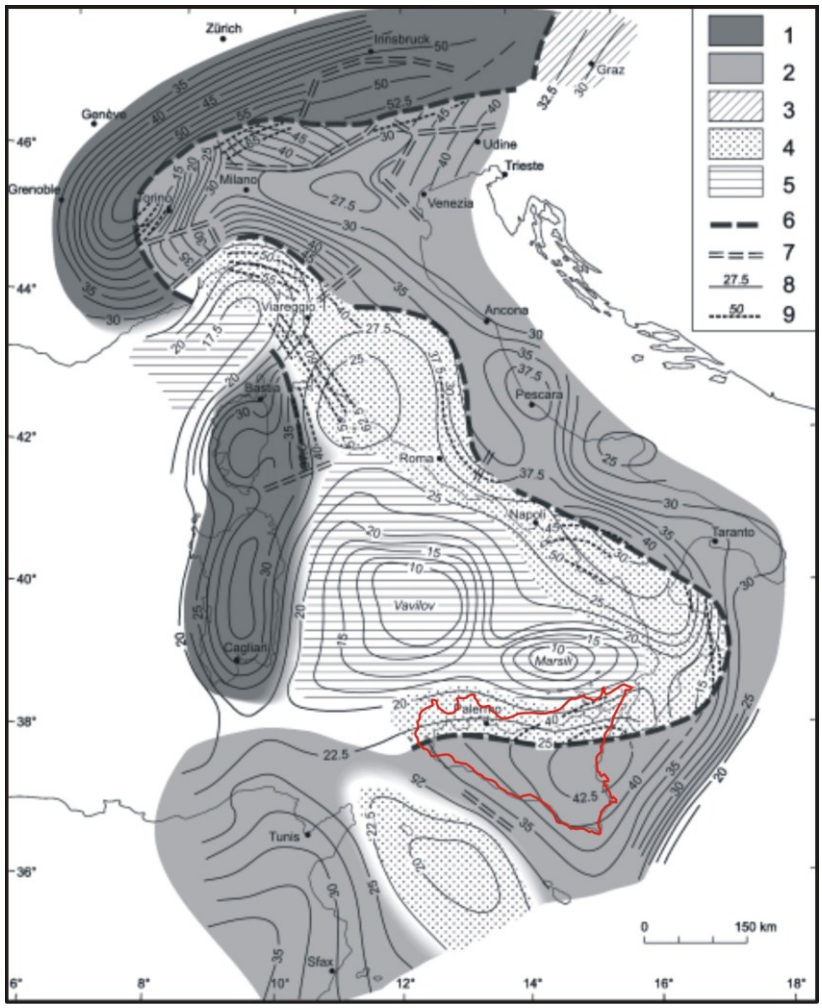

Fig. 6- *Depth contour-lines of the Moho boundary. Contour interval 2.5 km. (From Cassinis et alii, 2003, see the text for the legend and a detailed description).*

The thickness of the crust under eastern Sicily and the Moho topography beneath the Ionian Sea has been reinterpreted by Nicolich et alii (2000). The Authors used the results of the processing of an augmented grid of profiles at sea tying in all the Etna profiles and the Streamers Ionian profiles (Cernobori et alii, 1996) with offshore-

onshore wide angle control, in order to distinguish elements of the whole structure of the crust. Looking from the basin towards land (**Fig. 7**), the Moho deepens both towards Calabria in the north and Sicily in the south-west with depth of 30 km beneath the central Hyblean Plateau, rising to 22 km in the Gela-Catania Foredeep and to 21-18 km just offshore Catania (Nicolich et alii, 2000). Towards Calabria the Moho depth resumes a value on the order of 25 km or greater.

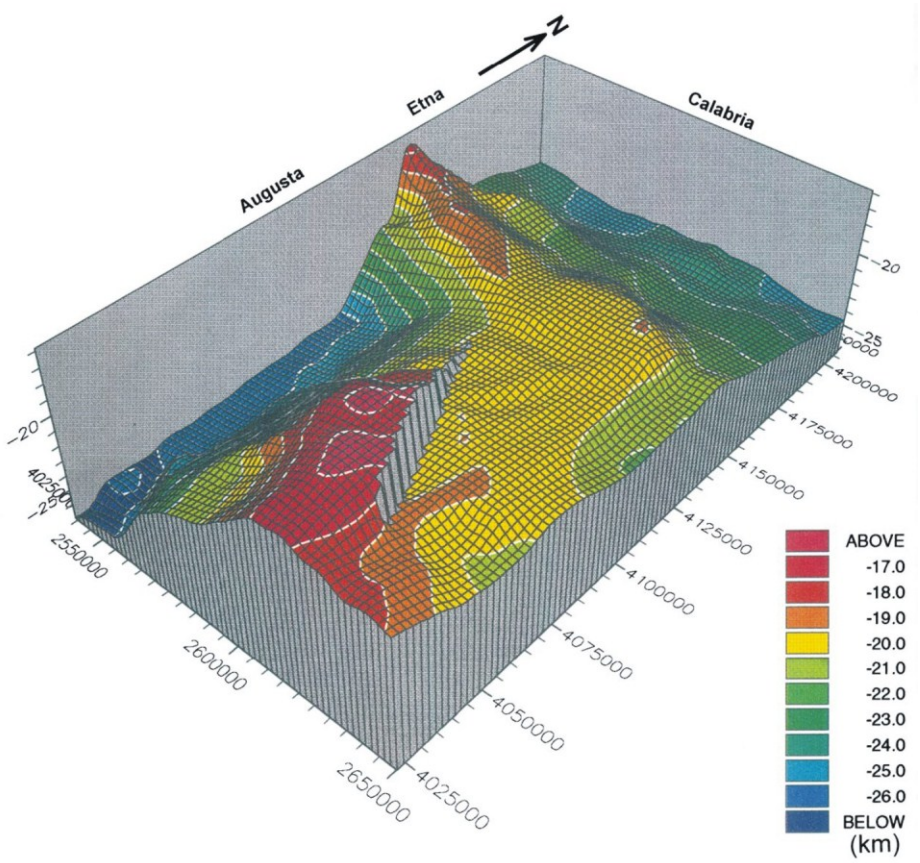

Fig. 7- *Perspective view of Moho topography looking from the Ionian basin to NNW. Etna is located on the NW prolongation of the mantle upwarp. (From Nicolich et alii, 2000).*

For further regional geological and geophysical profiles across Sicily see also Bello et alii (2000), Chironi et alii (2000), Finetti (2005), La Vecchia et alii (2007) and reference therein.

2.2.2 Tomographic models

Among the tomographic models available for the area, those of Scarfi et alii (2007) and Brancato et alii (2009) are the most recent ones. Descriptions of the velocity structure in the crust-upper mantle are provided below.

Scarfì et alii (2007) applied the adaptive mesh double difference tomography (Zhang and Thurber, 2005) to determine three dimensional V_P, V_S and V_P/V_S variations and event locations in southeastern Sicily (Italy). P-wave velocity (V_P) values ranged from 2.0 to 5.0 km/sec in the upper crust, increasing to ≥6.0 km/sec in the deeper crust (**Figs. 8** and **9**).

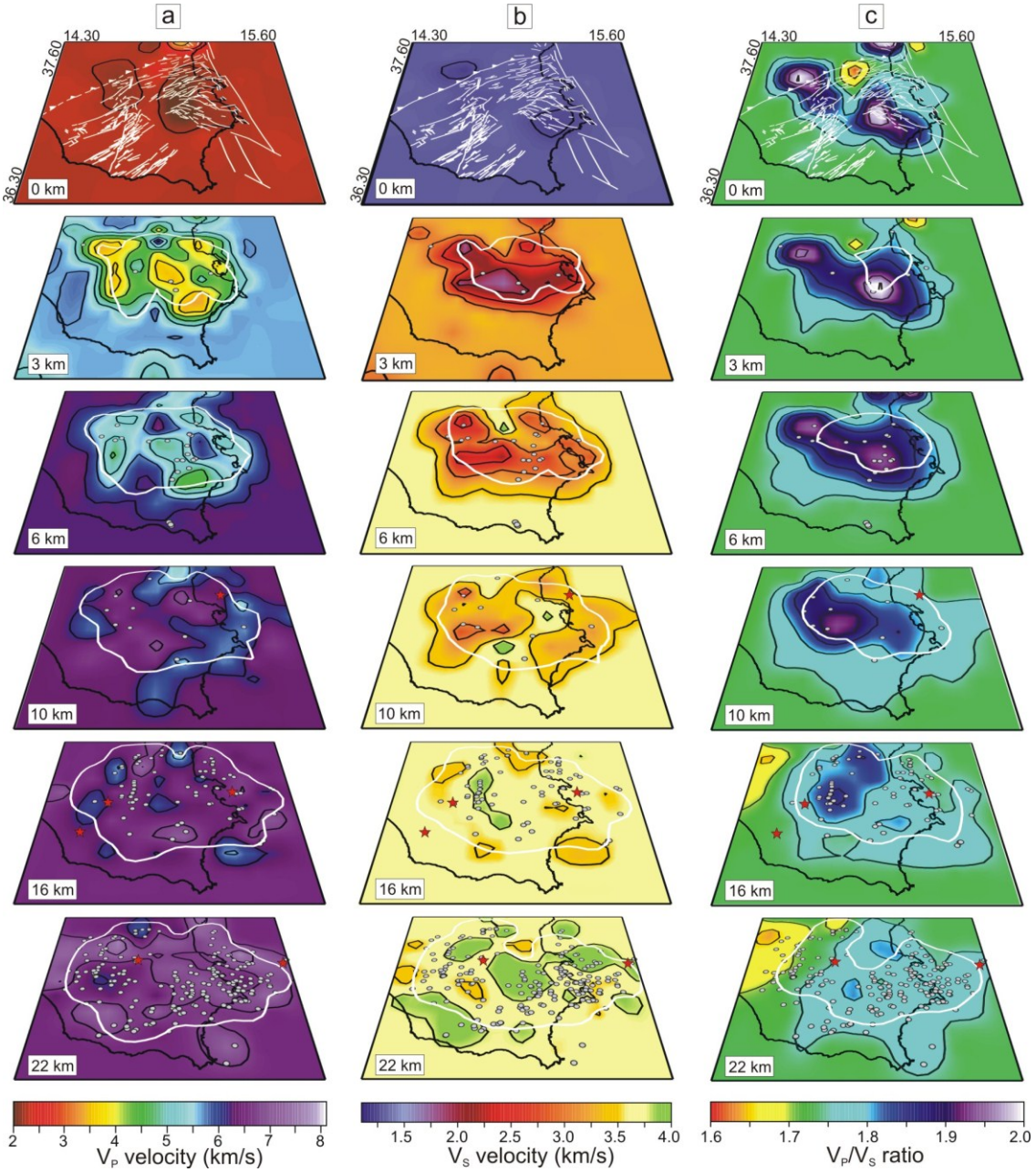

Fig. 8- *V_P (a), V_S (b) and V_P/V_S (c) models for six representative layers resulting from the 3D inversion. Contour lines are at interval of 0.5 km/s for V_P and V_S, and 0.05 for V_P/V_S. On the 0 km layer the main structural features are reported with white lines. Grey circles (M_L<3.5) and red stars (M_L≥3.5) represent the relocated earthquakes within half the grid size of the slice. The zones with DWS>100 (a) and DWS>50 (b and c) are circumscribed by white contour lines. (From Scarfì et alii, 2007).*

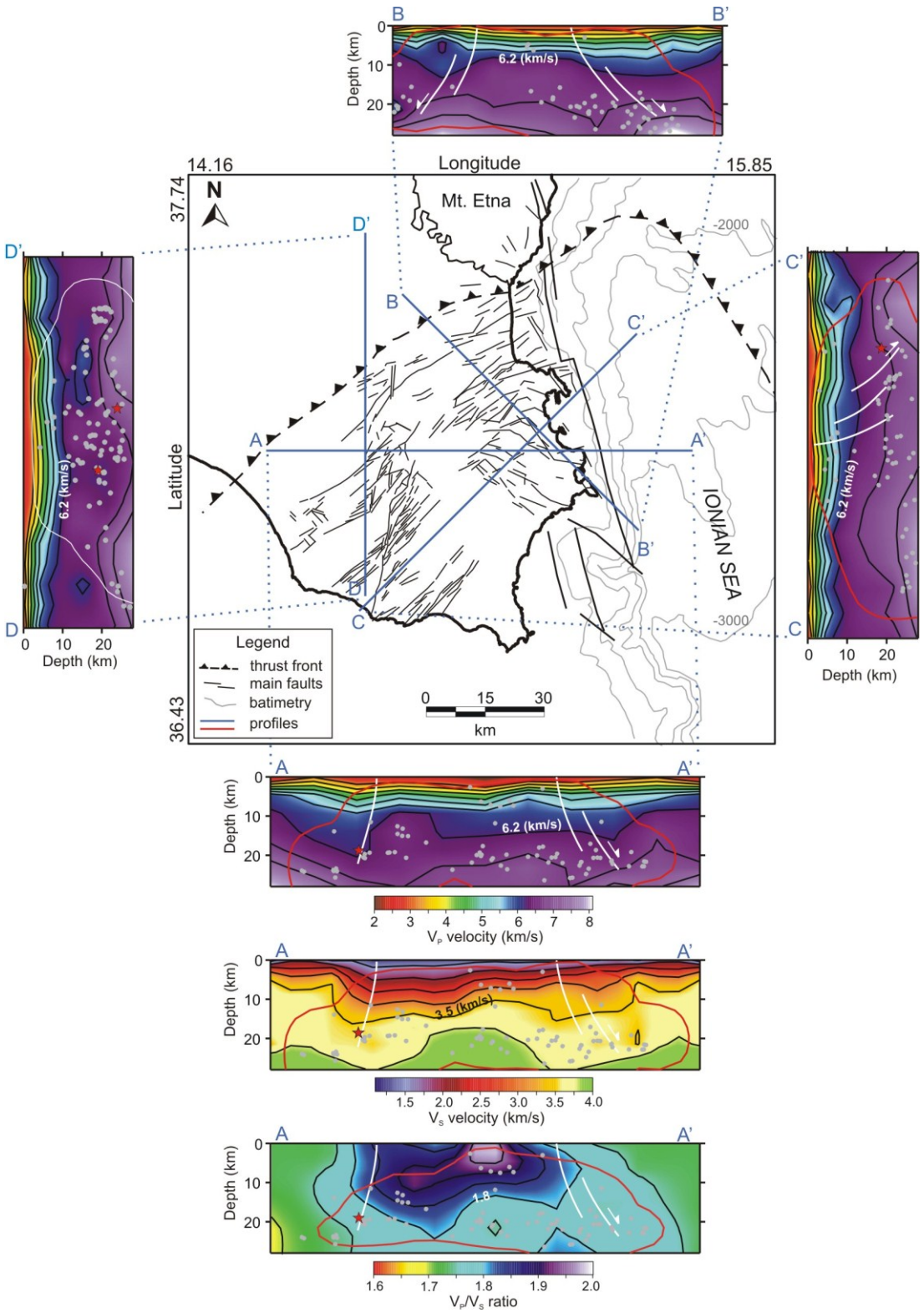

Fig. 9- *Vertical sections through the V_P, V_S and V_P/V_S models. The traces of sections are reported in the sketch map (AA', BB', CC' and DD'). Contour lines are at an interval of 0.5 km/s for V_P and V_S, and 0.05 for V_P/V_S. Red curves contour the zones with DWS>100 for V_P and DWS>50 for V_S and V_P/V_S. White lines indicate the main structural features (the geometry of the fault planes are purely an indication). Relocated earthquakes, within ±10 km from the AA', BB', CC' sections and within ±20 km from the DD' section, are plotted as grey circles (M_L<3.5) and red stars (M_L≥3.5). (From Scarfì et alii, 2007).*

A high V_P/V_S anomaly of 1.8-2.0, mainly corresponding to a low V_P and V_S zone, is imaged in the central region down to a depth of 16 km. The high V_P/V_S anomaly has been interpreted in terms of increase of crack density and presence of saturated fractures, which may decrease both P- and S-wave velocities and increase V_P/V_S ratios.

Map views from Brancato et alii (2009) are shown in **Fig. 10**.

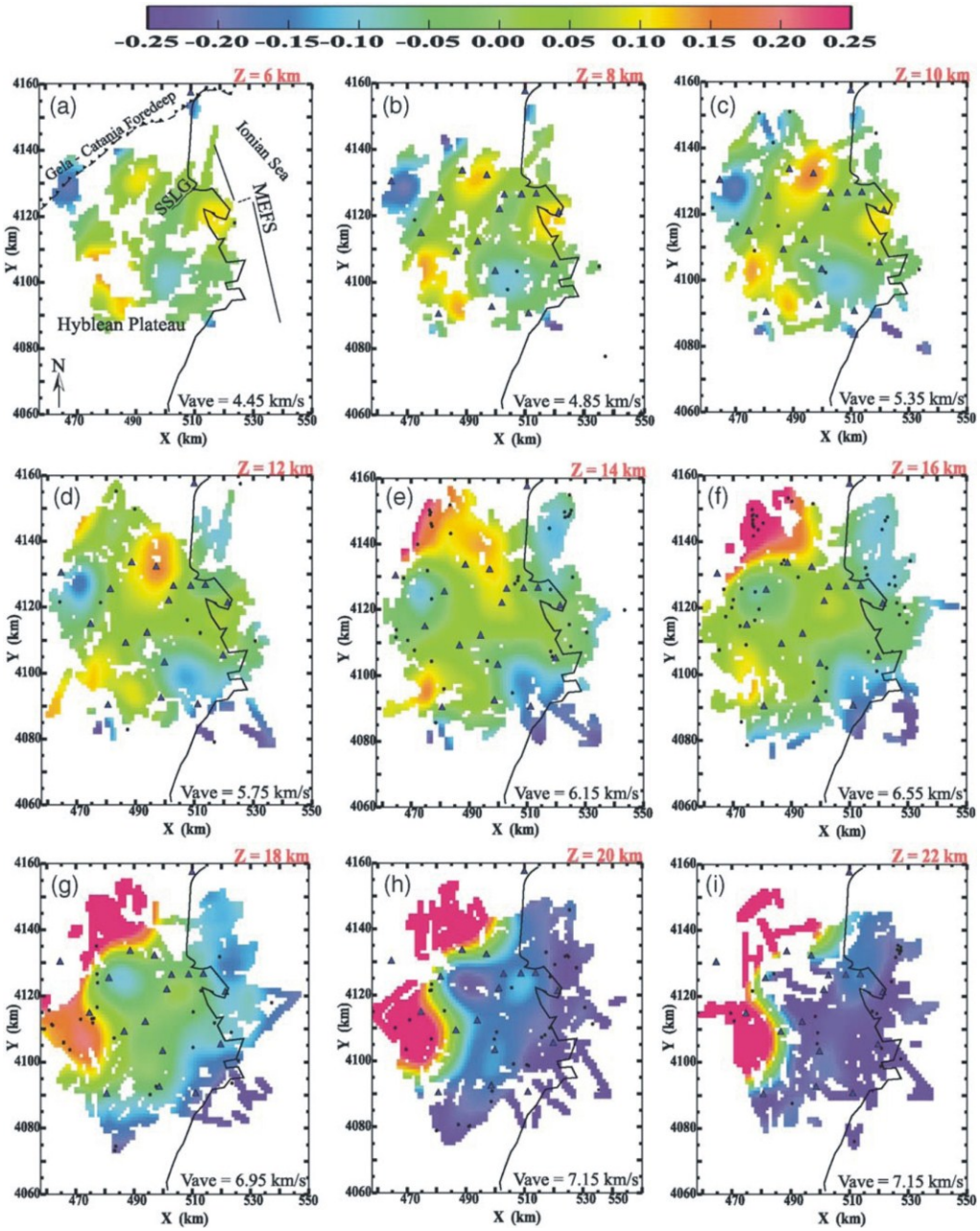

Fig. 10- *Depth slices through the tomographic seismic velocity model (smoothed 10×10×4 km). Triangles indicate seismic stations. (a) The surface locations of major fault systems and thrust fronts (seismic stations are removed for clarity). Earthquakes within 1 km above and below each slice are shown as black dots. The average velocities are also indicated in the bottom corner of each panel. The colour scale bar, at the top, represents the deviation from average velocities (in km/sec). Depths (Z) are relative to the sea level. (From Brancato et alii, 2009).*

Depth slices through the tomographic seismic velocity model show that down to a depth of 10 km the average V_P is relatively low (≤5.35 km/sec; **Fig. 10c**). For depths greater than 10 km, average velocity increases from 5.35 to 7.15 km/sec, then remains relatively constant below 20 km (**Fig. 10c-i**). An east-west velocity gradient in the midcrust is the most significant result supported by data. Below a depth of 12 km, P wave velocity (east of the Malta Escarpment fault system, MEFS) is lower than the average V_P obtained for the Hyblean Plateau (**Fig. 10d-g**). The velocity contrast is more evident at greater depth, where a variation >0.5 km/sec is observed (**Fig. 10h,i**). The best results correspond to the depth range 14-22 km. A high-velocity zone (**Fig. 10e,f**), between 14 and 16 km below sea level (north-northwest), is interpreted to be related to basaltic volcanic rocks and diffuse seismicity. A wide low velocity region, at greater depth (18-22 km below sea level), extends eastward from the buried front of Gela-Catania Foredeep to the MEFS (**Fig. 10g-i**). The variation is probably due to magmatic intrusions, which may induce a slight change (from ductile to brittle) in the physical properties of the rocks. These P-wave velocities are slightly different from those of Scarfì et alii (2007). In particular, P-wave velocities along the MEFS are as much as ~10% lower down to a depth of 10 km and ~4% lower deeper in the crust.

2.2.3 Recent Receiver Function studies and Local Seismicity

In the following, information on the previous receiver function (RF) studies in the area is provided in order to give a starting point to this analysis and to better define the previous knowledge about the seismic structure in this zone. Previous estimates of crustal thickness in southeastern Sicily were given by Piana Agostinetti and Amato (2009) by analyzing P-to-S conversion by the P-receiver function (P-RF) method; more recently S-receiver function (S-RF) method was applied by Miller and Piana Agostinetti (2011, 2012). Piana Agostinetti and Amato (2009) described and discussed a dataset of Moho depth and V_P/V_S estimates for peninsular Italy applying the stacking method of Zhu and Kanamori (2000). They found areas of average Moho depth (30-35 km) beneath southeastern Sicily with Moho depth ranging from the shallowest in the northeast (SSY=28.6±6.8 km) and west (HMDC=34±1.5 km, HVZN=33.5±9.3 km) to the deepest in the southeast (HAVL=41.5±11 km) (**Fig. 11**; see also **Fig. 22** for station location). More recently, Miller and Piana Agostinetti (2011, 2012) stacked S receiver functions providing lithospheric scale images of the structure of the continental material of the Hyblean Foreland. For each of the stacked S-RFs (**Fig. 12**), the picks for the

Moho and LAB interfaces (blue and red dashes, respectively) and a color-shaded (red-to-blue) filled circle beneath the Moho and LAB symbols indicate the sharpness of the relative pulse in the stacked S-RF. Grey diamonds show previous estimates of the Moho depth picked from P receiver functions (Piana Agostinetti and Amato, 2009).

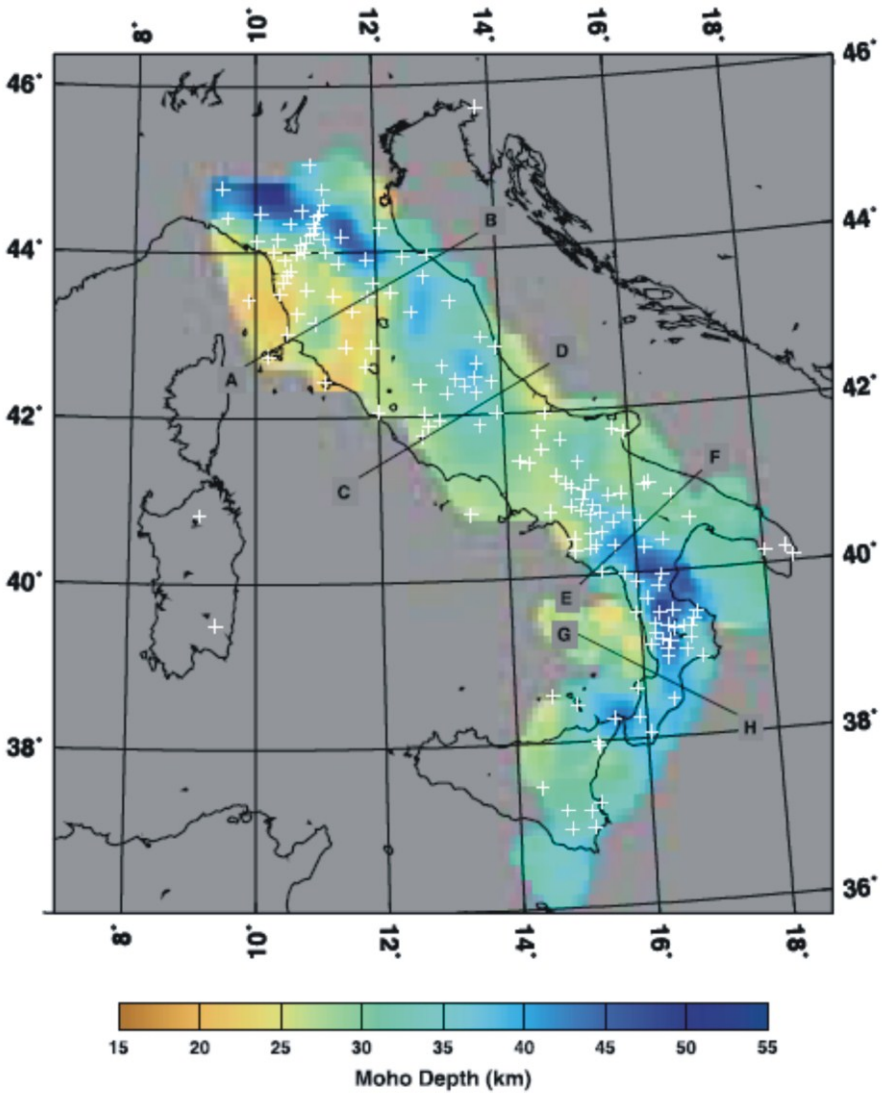

Fig. 11- *Map of Moho depth in peninsular Italy. Crosses indicate seismic stations. Results from Zhu and Kanamori's (2000) technique were weighted according to quality class and standard deviation from bootstrap analysis. (From Piana Agostinetti and Amato, 2009, see text for details).*

Moho depth ranges from the shallowest in the southeast (25 km) to the deepest in the northwest (~35 km). In particular, the Moho lies at a depth of 23 km below HAVL, 28 km below HMDC and 35 km below HVZN. The Moho depth estimates obtained by S receiver functions show a thicker crust toward the northwest, which is in disagreement with the previous P-RFs results (Piana Agostinetti and Amato, 2009) for station HAVL, that shows the largest discrepancy in interpretation of the Moho depth (~15 km). The

discrepancy in the two receiver function results can be the result of various factors (see Miller and Piana Agostinetti, 2011 for the explanation).

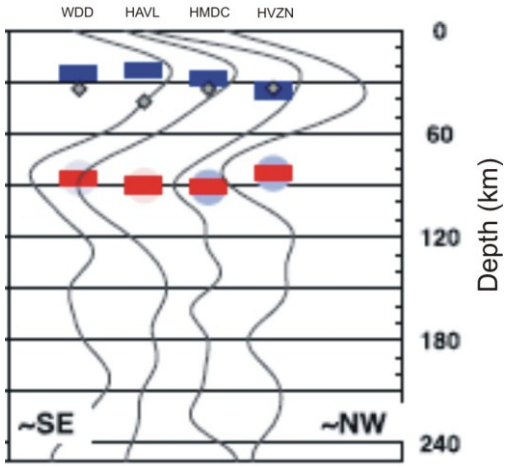

Fig. 12- *S-RF stack for the stations HAVL, HMDC and HVZN. Blue and red lines indicate S_P from the Moho and S_P from the LAB. Grey diamonds represent Moho depth estimates from P-RF analysis by Piana Agostinetti and Amato (2009). (From Miller and Piana Agostinetti, 2011).*

In the following the spatial distribution (work in progress) of 885 earthquakes (1.0≤ Ml≤ 4.6), recorded from January 1994 to June 2012 in southeastern Sicily by the seismic permanent Network currently operated by the Istituto Nazionale di Geofisica e Vulcanologia (INGV, Osservatorio Etneo, Sezione di Catania), is shown.

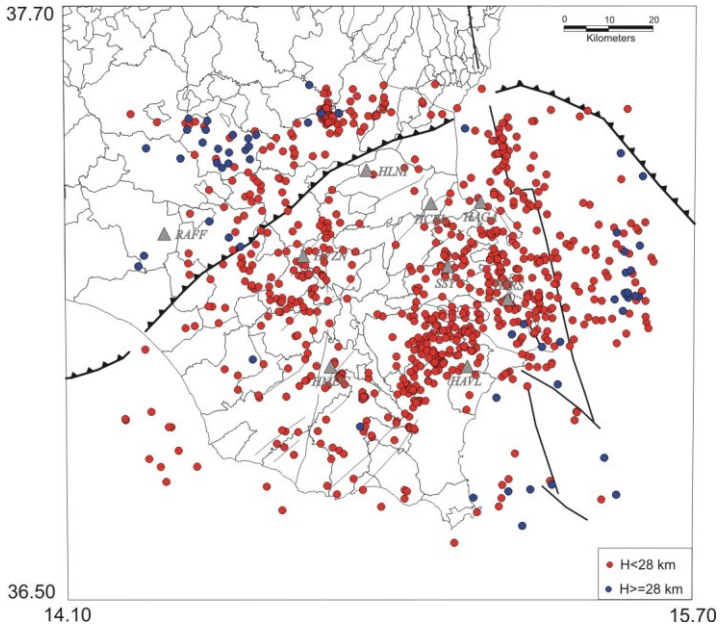

Fig. 13- *Map of the 885 seismic events recorded between 1994 and 2012. Red circles show the earthquakes with H<28km, while blue circles display deeper (≥28 km focal depth) seismicity.*

The main features revealed by the instrumental seismicity are shown in **Fig. 13** (map) and **Fig. 14** (cross sections). Depth seismicity generally extends down to 40 km, with events mainly concentrated from 15 to 25 km and no located earthquakes in the very shallow region (0-3.0 km). Events with depth greater than 30 km seem more widely spread. The observed pattern clearly displays a trend that shallows from north to south. Moreover, it should be noted the seismicity pattern along the W-E cross section shows earthquakes getting shallower in the central part of the region and earthquakes getting deeper shifting westwards and eastwards.

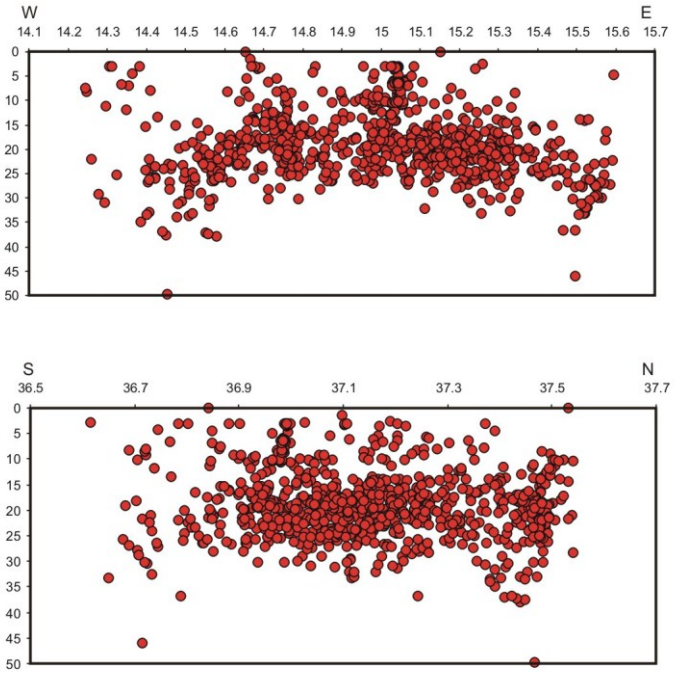

Fig. 14- *Cross-sections of the 885 seismic events recorded between 1994 and 2012.*

In the light of the above reported points, the results of this study will be discussed for understanding the geologic and tectonic processes that have been dominant in the region, enhancing the understanding of how ancient tectonic events continue to shape and define the structure of our continent and discussing also some original implications for the geological evolution of this complex tectonic region.

Chapter 3

In Receiver function technique the teleseismic body waveforms are used to image the crustal structures underneath isolated seismic stations (e.g. Langston, 1977; Owens and Zandt, 1985; Ammon et alii, 1990; Ammon, 1991). These waveforms contain information related to the source time function, propagation effect through the mantle and local structures underneath the recording site. The method aims to eliminate source-related and mantle-path effects, enhancing P_S conversions and reverberations associated with crustal and mantle structure near the receiver. The derived "receiver function" (RF) (Burdick and Langston, 1977) primarily consists of phases associated with discontinuities (such as the Moho) beneath the receivers (Owens and Zandt, 1985).

The basic aspect of this method is that as seismic rays cross discontinuities, the energy of the incoming ray is partitioned between reflected and refracted rays (**Fig. 15**).

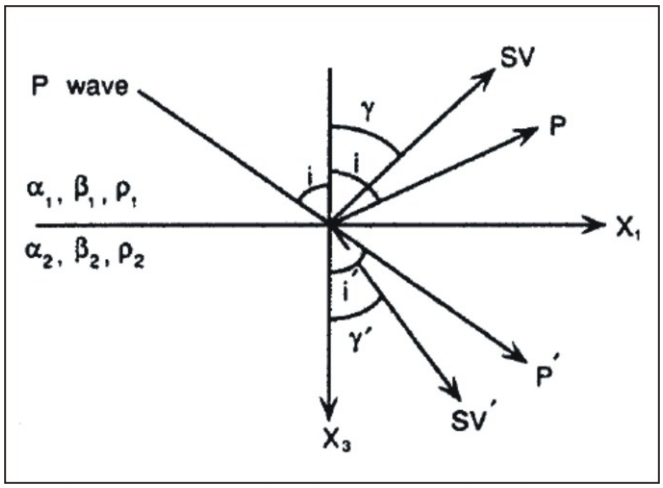

Fig. 15- *The ray geometry for an incident P wave on a solid-solid interface and the resulting four derivates: refracted P (P'), reflected P (P), refracted SV (SV'), reflected SV (SV). α, β and ρ represent P wave velocity, S wave velocity and density, respectively.*

The geometry of the incident P wave and its derivatives is governed by Snell's law:

$$(Sin\, i)/\alpha_1 = (Sin\gamma)/\beta_1 = (Sin\gamma')/\beta = (Sin\, i')/\alpha_2 \qquad (\mathbf{3.1})$$

whereas the amplitudes of the partitioned energy are determined by wave-field theory and represented by reflection and transmission coefficients. Receiver function method is a way to detect, isolate and enhance P-to-SV conversion mode which is produced as teleseismic P waves cross a seismic discontinuity (**Fig. 16**). Basically, the S waves travel slower than the P waves, so, a direct measure of the depth of the discontinuity is calculated by the time difference in the arrival of the direct P wave and the converted

phase (P_S), provided the velocity model is known. In addition to the direct P_S converted phases, the multiples resulting from the discontinuity and free surface, are also seen on the receiver function traces (**Figs. 16** and **17**).

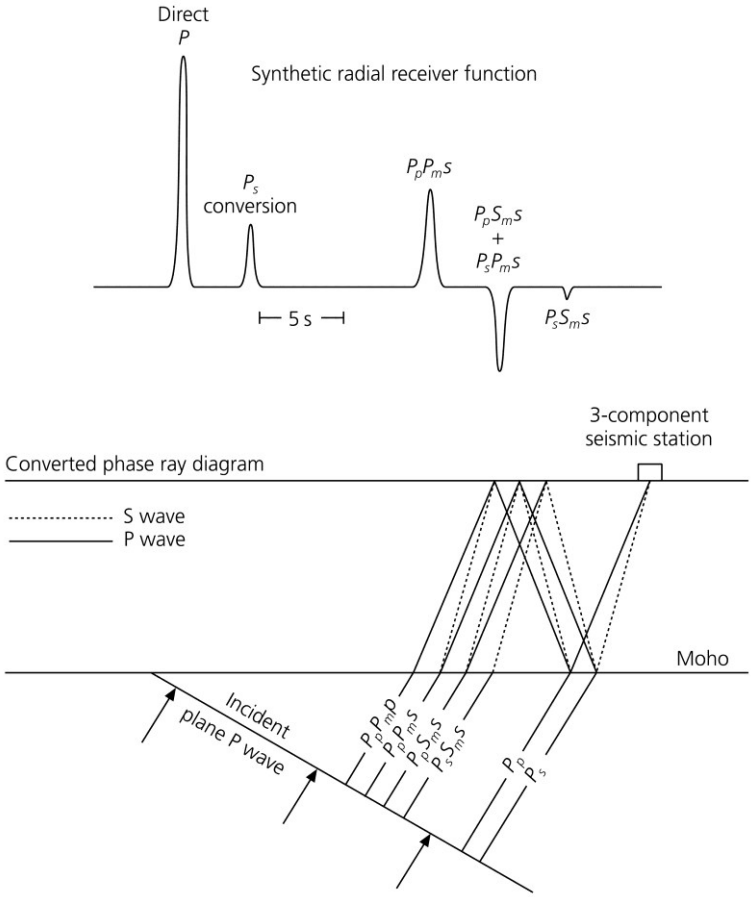

Fig. 16- *Sketch illustrating the major P_S converted phases for a layer over a half space model (bottom). Simplified R-component receiver function corresponding to the model, showing the direct P and P_S conversions from the Moho and its multiple (top). (From Owens et alii, 1987).*

The amplitudes of these phases depend on the incidence angle of the impinging P wave, the velocity contrast across the discontinuities and the gradient of the velocity changes. The relative arrival times of the converted phases and multiples depend on the depth of the velocity discontinuities, and the P and S velocity structure between the discontinuity and the surface. Radial RFs primarily provide information about changes in the S-wave velocity in the crust and upper mantle, whereas transverse RFs can provide information on anisotropy and help to identify dipping structures. Simple 3D structures, like dipping interfaces and layers containing hexagonally anisotropic materials, generate periodic patterns in the RF dataset, as a function of BAZ (Levin and Park, 1998). The analysis of such periodicity has been used to infer the presence of

anisotropy in the subsurface (e.g. Bianchi et alii, 2008) or dipping interfaces (e.g. Lucente et alii, 2005). A thorough numerical investigation of effects on receiver functions is described by Cassidy (1992). In this chapter, the methods, which were applied to the data are briefly introduced.

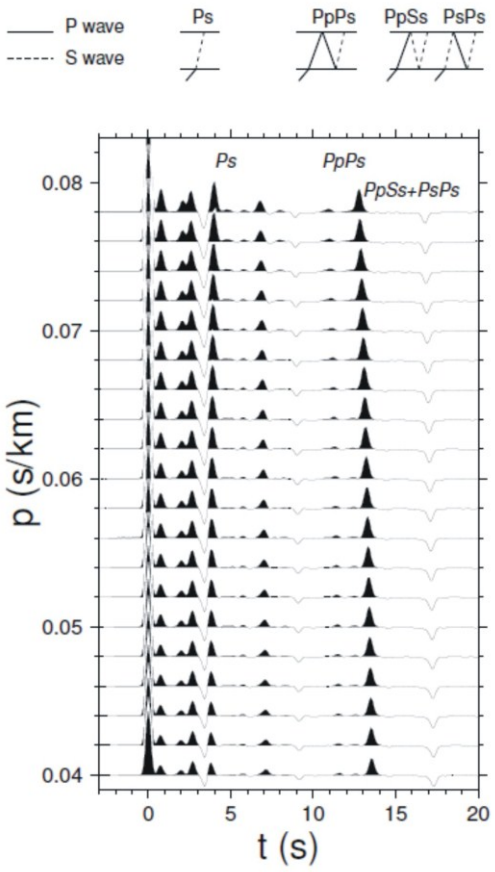

Fig. 17- *Moho converted phase P_S (Moho at 32 km depth) and multiples P_PP_S, P_PS_S+P_SP_S on the radial receiver function (bottom) and their ray paths (top). (From Zhu and Kanamori, 2000).*

3.1 Methods

3.1.1 P-to-S receiver function method

The teleseismic P receiver function method has become a popular technique to constrain crustal and upper mantle velocity discontinuities under a seismic station (e.g., Langston, 1977; Owens et alii, 1984; Kind and Vinnik, 1988; Ammon, 1991; Kosarev et alii, 1999; Yuan et alii, 2000). Langston (1977) showed that if the incident P waves arrive at a high angle to the surface, deconvolving the vertical component (on which P wave energy will dominate) from the horizontal radial component (on which the SV waves produced by P-to-S conversions will be recorded) will yield a deconvolved time

series (termed ‘‘receiver function’’ or source equalized trace) on which the major features are S wave arrivals related to P-to-S conversions and reflections in the crust and uppermost mantle beneath the station. P wave energy on the radial component, that is coherent with energy on the vertical component, will be compressed by the deconvolution into a single spike at zero lag time. On the receiver function, all subsequent arrivals after direct P have times calculated relative to the coherence peak, so that peak is commonly referred to as the direct P wave arrival. Because of the large velocity contrast at the crust-mantle boundary, the Moho P-to-S conversion (P_S) is often the largest signal following the direct P. The amplitude, arrival time, and polarity of the locally generated P_S phases are sensitive to the S-velocity structure beneath the recording station. By calculating the time difference in arrival of the converted P_S phase relative to the direct P wave, the depth of the discontinuity can be estimated using a reference velocity model. Preparing the broadband teleseismic data involved a series of quality checks and multiple processing steps in order to isolate, detect and enhance the SV phases hidden in the P coda of teleseismic earthquakes.

Initially each seismogram was rotated from the NEZ (**Fig. 18a**) to the RTZ (radial/transverse/vertical) (**Fig. 18b**) coordinate system (using the event’s backazimuth), where R (radial) is calculated along the great circle path between station and event epicenter (positively-directed from event to station), T (transverse) is 90° clockwise from R and Z is vertical (positive up).

The vertical and radial components of motion (Z(t) and R(t), respectively), restituted after the rotation, can be theoretically represented by:

$$Z(t) = \sum_{k=0}^{n} z_k s(t - t_k) \qquad (\mathbf{3.2})$$

$$R(t) = \sum_{k=0}^{n} r_k s(t - t_k) \qquad (\mathbf{3.3})$$

where *s(t)* is the source time function; t_k is the arrival time of the k_{th} ray (k = 0 is the direct P wave); and the sum over *n* represents a sum over *n* rays. The amplitude of the k_{th} arrival of each component is described by z_k and r_k. The source equalization procedure of Langston (1979) consists of a simple deconvolution of the vertical component from the radial component of motion:

$$H(\omega) = \frac{S(\omega)R(\omega)}{S(\omega)Z(\omega)} = \frac{R(\omega)}{Z(\omega)} \tag{3.4}$$

S(ω) is the source spectrum; H(ω) is the Fourier transform of the receiver function, h(t); ω is radial frequency; and

$$R(\omega) = r_0 \sum_{k=0}^{n} \hat{r}_k \, e^{-i\omega t_k} \tag{3.5}$$

$$Z(\omega) = z_0 \sum_{k=0}^{n} \hat{z}_k \, e^{-i\omega t_k} \tag{3.6}$$

where $\hat{z}_k$ represents the amplitude of the k_{th} arrival normalized by the amplitude of the direct P wave on the vertical component, $\hat{z}_k = z_k / z_0$, and similarly, $\hat{r}_k = r_k / r_0$.

Equation (3.4) is the defining equation for what is frequently called the receiver function.

The receiver function is the time series corresponding to the complex spectral ratio of the radial response to the vertical response. In plane-layered media, for steeply incident plane waves, the receiver function maintains many of the properties of a seismogram. In fact, individual peaks and troughs on the receiver function correspond to individual arrivals on the radial component response to the incident plane wave. Details of the background behind the technique, together with examples, are given by Ammon (1991).

In this study receiver functions were computed using the technique developed by Ligorria and Ammon (1999) through a time-domain deconvolution of the vertical component of a teleseismic waveform from horizontal radial (along path) and tangential components (at 90° to the direction of propagation) of a seismogram for a particular earthquake (**Fig. 19**). The deconvolution procedure extracts the P_S phases (S waves converted from P at refracting interfaces) with amplitudes of the conversions depending upon the impedance contrast across the interface and the incidence angle. The time domain approach consists of approximating the deconvolution response through a series of Gaussian pulses with adjusted amplitudes and time lags. This technique circumvents stability problems intrinsic to spectral division, leads to a causal response, and generally produces more stable results in the presence of noise (Ligorria and Ammon, 1999).

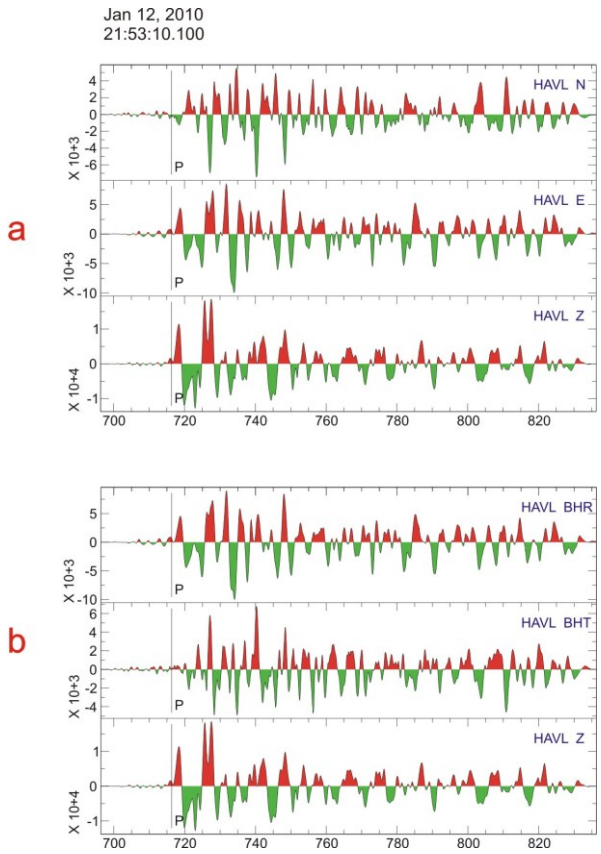

Fig. 18- *Three-component recordings (a) and rotated horizontal components (b) of the January 12, 2010 (Mw=7.0) seismic event (Haiti region; epicentral distance=77°; backazimuth= 283°). Z, N-S, and E-W represent the recorded vertical, north-south, and east-west components.*

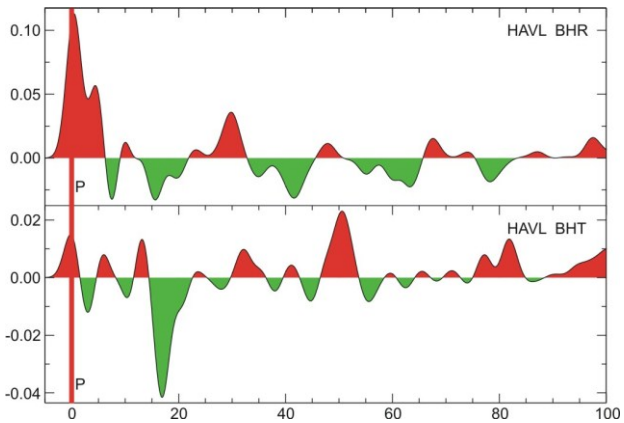

Fig. 19- *Radial and transverse receiver functions of the January 12, 2010 event shown in Fig. 18. The naming convention is that the character, 'R' or 'T', indicates whether this is the P-wave receiver function for the radial or transverse component. For a plane-layered velocity model and no noise, the 'T' should be zero. If it is not small this indicates that the original data were bad, or that the structure is not plane-layered and isotropic.*

RFs from a single station span a range of azimuths and incidence angles illuminating

subsurface refractors at different points. Positive amplitudes in the receiver function reveal a velocity increase with depth, while negative amplitudes indicate a velocity decrease with depth. Including multiples paths in the receiver function analysis (it they are properly identified) gives additional information about the exact depth of the Moho discontinuity and the crustal Poisson's ratio (Zhu and Kanamori, 2000; Yuan et alii, 2002). However, the presence of significant sediments may alter the primary P_S converted phases and make the estimation of the discontinuity depth difficult. An other problem occurs if a dipping interface changes the ray geometry or an anisotropic layer causes shear wave splitting effects. In both cases converted energy is expected to be observed on the T components (Cassidy, 1992; Levin and Park, 1997).

A crucial feature of the receiver function method is that the source equalized traces for events clustered at roughly the same distance and azimuth can be stacked to improve signal-to-noise ratio. However, successful alignment and constructive summation of conversion phases requires that the receiver functions be equalized in terms of their ray parameters. Aligning the move-out corrected receiver functions according to the epicentral distances Δ (or ray parameters p) not only helps to distinguish the direct conversions, but also allows for enhancement of conversions by constructive summation (stacking) of amplitudes direct conversion whereas the multiples will be substantially suppressed. Move-out correction can also be applied to crustal reverberations. Applying the correction to each multiple and aligning the corrected seismograms by epicentral distance (or ray parameter) leads to straight appearance of the multiples whereas the direct conversions are inclined. After the correction is applied those reverberations which have similar ray parameters appear parallel to each other made. As example, **Fig. 20** illustrate the amplitude and arrival-time variations as a function of BAZ and ray parameter (p) for a P_S phase generated at an eastward-dipping boundary (strike=N0°E, dip angle=20°) at 60 km depth (Cassidy, 1992). The most rapid variation in both the amplitude and arrival time of a P_S phase generated at a dipping interface occurs along the strike direction of the boundary. As stated in Cassidy (1992), P_S amplitudes always increase for decreasing Δ (or increasing ray parameter; see **Fig. 20**). In contrast, the amplitude of the reverberations may remain constant or even decrease with decreasing Δ (or increasing ray parameter). This may be useful to discriminate between reverberations and P_S conversions. Additionally, reverberations and scattered energy may be identified by their rapid variations in either amplitude or arrival time over a small range of BAZ or Δ. Thus, for reverberations associated with dipping interfaces,

the variation in the polarity, amplitude, and arrival time as a function of BAZ and Δ, and the large lateral sampling area (relative to P_S phases), suggests that it would be extremely difficult to accurately model such phases. It is obvious that formal inversion techniques, which attempt to match all arrivals in a waveform, must be applied with extreme caution. It would be prudent to begin by forward modeling only for those phases whose amplitude and arrival time variations as a function of both BAZ and Δ are indicative of P_S.

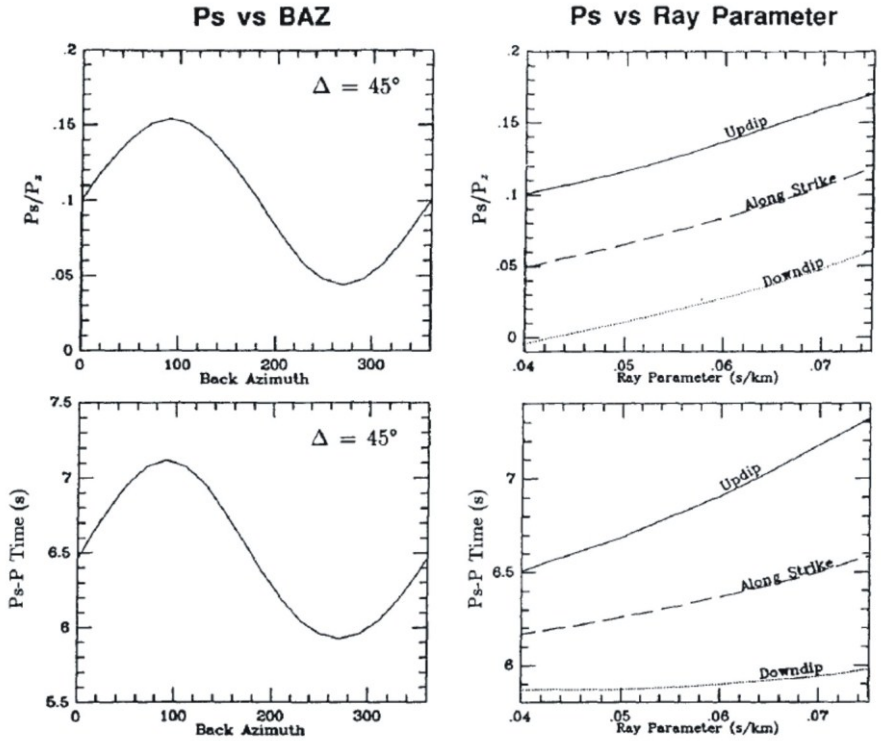

Fig. 20- *Amplitude and arrival time variation as a function of backazimuth and ray parameter (from Cassidy, 1992).*

Chen and Liu (2000) investigated the effects of laterally inhomogeneous crustal structure with planar dipping interfaces on the teleseismic receiver function. In case of a single dipping interface the receiver functions vary regularly with azimuths. The regularity of the variations could be summarized into the following main points: (1) The variations of the amplitude and arrival time of each arrival with azimuths have axis clear symmetry for the radial components and asymmetry for the tangential components of the receiver function about the dipping direction of the interface under station. (2) The amplitude ratio of the P wave between the radial and vertical component of the receiver function varies regularly with azimuths. This ratio becomes minimized along the dipping direction and maximized along the inversely dipping direction. A similar

regularity also appears on the tangential component of the receiver function. This phenomenon is caused by the dipping discontinuity under the station. The incident angle at the dipping interface and the emergent angle on the surface are different for different azimuths. (3) On the radial component of the receiver function the phase delay of the P_S converted wave and multiple reflections have the same variation regularity with azimuths. Their phase delays relative to the direct P wave become maximal in the dipping direction and minimal in the inverse dipping direction of the interface. In case of several different dipping interfaces, the wave energy distributions of the receiver function on the vertical, radial and tangential component are changed also, when varying the dipping angle of the interface under the station. These can be summarized into the following main points: the radial and tangential components of the receiver function is no longer symmetric with the azimuth; the arrival time of each phase have no longer consistent regularity of variations with azimuths; there is no incident azimuth, in which the amplitude of the tangential component of the receiver function becomes zero. Therefore, when several different dipping interfaces exist in the receiver structure, the wavefield of the receiver function become much more complicated. Nevertheless, under this complicated case we can find also some of regularities: (1) According to the polarization direction of the first arrival in the tangential component, we can infer the apparent dipping direction of the laterally inhomogeneous structure. So-called apparent dipping direction is not the accurate dipping direction of each interface, but an overall direction of different dipping interfaces. This is only a very rough estimation, but valuable for the further inversion study. (2) Although the amplitudes of the P_S converted waves at each interface are influenced each other, the variations of the P_S converted wave at the second interface are still clear. Therefore, the dipping direction and dipping angle of the second interface can still be estimated.

For theoretical background of the technique used to analyse the waveforms around the world see Kosarev et alii (1987), Kosarev et alii (1993), Kind et alii (1995), Yuan et alii (1997), Sandvol et alii (1998) and Ramesh et alii (2002).

3.1.2 Estimation of crustal thickness and V_P/V_S ratio

As stated above, receiver functions are created by deconvolving the vertical component from the radial and tangential components of a seismogram for a particular earthquake. Effectively, it turns three different axes of motion from each event into just one seismogram so one can more easily investigate several earthquakes at once. In

particular, using RFs makes it easier to identify the incoming P-wave to S-wave conversions like P_S, P_PP_S, and the combined P_PS_S+P_SP_S, all of which involve conversions of seismic P- and S- waves as they interact with the crust-mantle boundary. By comparing the difference in arrival times between any of these converted phases and the initial P-wave, we can determine the amount of time it takes a certain type of wave to traverse the thickness of the crust. With this information, the velocity and distance travelled can then be determined using a linear relationship. When the linear relationships between all three arrivals for each earthquake are combined, the point of intersection indicates the unique solution to the three lines and it represents the best-fit thickness and wave speed for the crust below that station.

Zhu and Kanamori (2000) proposed a stacking algorithm which sums the amplitudes of receiver functions at the predicted arrival times of the Moho conversion phase and its multiples (P_S, P_PP_S, and P_PS_S+P_SP_S) for different crustal thickness H and V_P/V_S ratios. Consequently, time domain receiver functions are mapped into H vs. V_P/V_S domain without the necessity to read phases.

Using the time difference between the P_{SMoho} phase and the first arrival, the depth to Moho can be estimated based on the following equation:

$$H = t_{ps} \Big/ \left(\left(1/Vs^2 - p^2\right)^{1/2} - \left(1/Vp^2 - p^2\right)^{1/2} \right) \qquad (\mathbf{3.7})$$

where H is the depth to Moho, t_{ps} is the time delay between the first arrival and the Moho phase, V_S is the S wave velocity, V_P is the P wave velocity, and p is the ray parameter.

However, since the delay time of the S leg is dependent on the shear velocity of the medium, the crustal thickness trades off strongly with the seismic wave velocity (Zhu and Kanamori, 2000). Incorporating multiply reflected phases such as P_PP_S and P_PS_S+P_SP_S helps to reduce this trade off significantly. The time delays (t_{PpPs} and $t_{PpSs+PsPs}$) for P_PP_S and P_PS_S+P_SP_S phases and H can be expressed in the following equations:

$$H = t_{PpPs} \Big/ \left(\left(1/Vs^2 - p^2\right)^{1/2} - \left(1/Vp^2 - p^2\right)^{1/2} \right) \qquad (\mathbf{3.8})$$

$$H = t_{PpSs+PsPs} \Big/ 2\left(1/Vs^2 - p^2\right)^{1/2} \qquad (\mathbf{3.9})$$

To further enhance the signal/noise ratio and reduce lateral variations, multiple receiver functions are stacked in the time domain. Zhu and Kanamori (2000) developed a straightforward approach that adds the amplitudes of the P_{SMoho} and multiples at the predicted time by varying H (crustal thickness) and the V_P/V_S. This "slant stacking"

approach essentially transforms the receiver function stacks from the time domain to the H-V_P/V_S domain. The H-V_P/V_S domain stacking is defined by:

$$S(H,Vp/Vs) = w_1 r(t_{ps}) + w_2 r(t_{PpPs}) - w_3 r(t_{PpSs+PsPs}) \quad \textbf{(3.10)}$$

where the $r(t_i)$ are the receiver function amplitude at the time t_{Ps}, t_{PpPs} and $t_{PpSs+PsPs}$ and w_1, w_2, and w_3 are the weighting factors for each phase that sum to unity.

The function *S(H,* V_P/V_S*)* reaches a maximum when all three phases (P_S, P_PP_S, and P_PS_S+P_SP_S) are stacked coherently (**Fig. 21**).

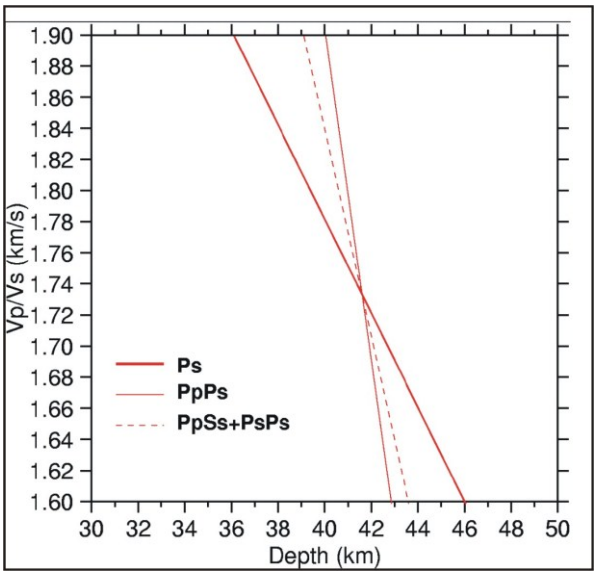

Fig. 21- *Contributions of* P_S *and its multiples to the stacked amplitude as a function of crustal thickness (H) and* V_P/V_S *ratio.*

The obtained H (crustal thickness) and V_P/V_S ratio are also considered as the best combination underneath the assumed station if the multiples are clear enough. The main advantage of this technique is that there is no need to pick the arrival times of the Moho or the multiples, making this technique more objective than having to manually identify these various phases. This approach also removes the effects of different ray parameters (*p*) on the moveout of the listed P-to-S converted phases. When receiver functions contain clear Moho conversions and Moho crustal multiples and spread over broad epicentral distances this method is able to detect the crustal depth as well as average V_P/V_S ratio with rather high precision. By combining such point data over a seismic network it is possible to produce maps of crustal thickness and V_P/V_S ratios which are indispensable for structural studies.

Chapter 4

4.1 Data and Methods

In choosing observations to use for computing receiver functions (RFs), we selected teleseismic events recorded between January 2004 and April 2011 at 8 broadband seismic stations (red triangles in **Fig. 22;** coordinates and equipments in **Table 1** and **2**) deployed in southeastern Sicily (Italy), all of which are part of the seismic permanent Network currently operated by the Istituto Nazionale di Geofisica e Vulcanologia (INGV, Osservatorio Etneo, Sezione di Catania). HSRS station (black triangle in **Fig. 22**), equipped with a short period seismometer, was not used for Moho depth estimation.

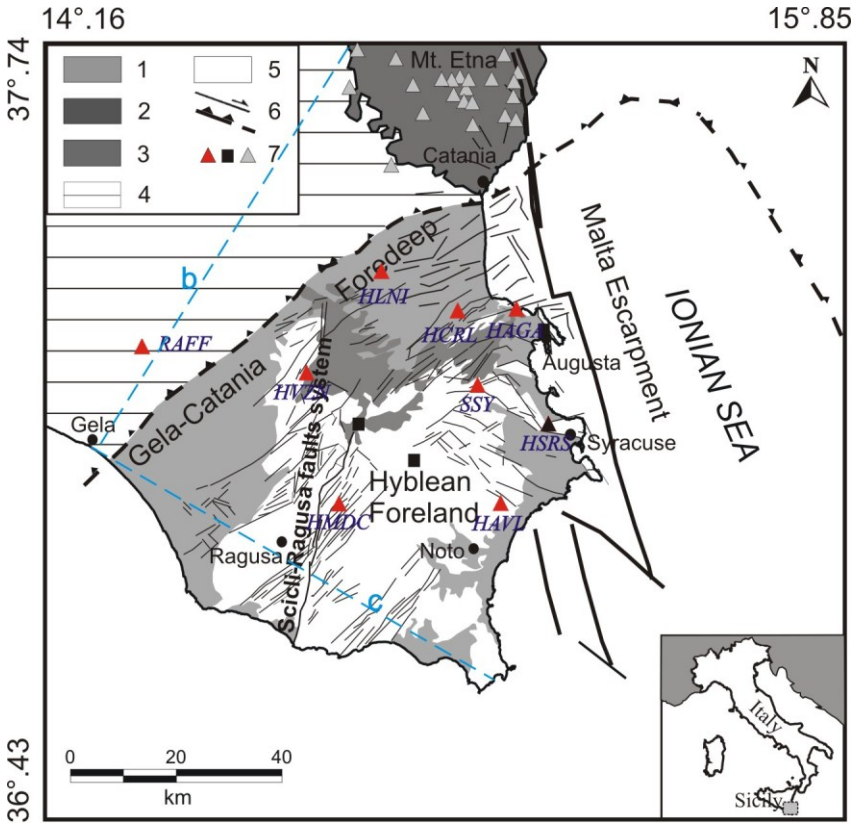

Fig. 22- *Geological sketch map of southeastern Sicily (modified from Azzaro and Barbano, 2000). 1=Recent-Quaternary deposits; 2=Late Pleistocene-Holocene Etnean volcanics; 3=Plio-Pleistocene Hyblean volcanics; 4=Appennine-Maghrebian units; 5=Meso-Cenozoic carbonate sediments; 6=normal, strike-slip faults and main thrust fronts; 7=seismic stations (red and black triangles, Sicilian Network; black squares, Italian National Network; gray triangles, Etnean Network). (b) and (c)= traces of the interpretative cross sections shown in Fig. 4.*

These stations overlie several interesting geological provinces in the region, covering Recent Quaternary deposits, Plio-Pleistocene Hyblean volcanics, Appennine-Maghrebian units and Meso-Cenozoic carbonate sediments (**Fig. 22**). The seismic

stations, with an average station spacing of 20-25 km, are set up in Augusta (HAGA), Avola (HAVL), Carlentini (HCRL), Lentini (HLNI), Modica (HMDC), Vizzini (HVZN), Raffadali (RAFF) and Solarino (SSY).

Table 1- *Station names and locations*

Station	Lat.N	Long.E	Elevation (m)	Location	Geology
HAGA	37.285	15.155	126	Augusta	Plio-Pleistocene Hyblean volcanics
HAVL	36.96	15.122	503	Avola	Meso-Cenozoic carbonate sediments
HCRL	37.283	15.032	190	Carlentini	Plio-Pleistocene Hyblean volcanics
HLNI	37.348	14.872	147	Lentini	Recent Quaternary deposits
HMDC	36.959	14.783	600	Modica	Meso-Cenozoic carbonate sediments
HVZN	37.178	14.715	788	Vizzini	Plio-Pleistocene Hyblean volcanics
RAFF	37.222	14.362	510	Raffadali	Appennine-Maghrebian Units
SSY	37.158	15.074	602	Sortino	Meso-Cenozoic carbonate sediments

Most stations were active from 2005 (with a few exception of SSY since 2004 and RAFF and HLNI since 2006 and 2009, respectively) and provided good quality recordings of numerous teleseismic earthquakes from around the world. Seismometer Network consists of Nanometrics Trillium 40s velocimetric sensors that measure ground motion over a wide frequency range with a flat response to velocity from 0.025 to 50 Hz; data are digitized at a rate of 100 samples per second by a 24 bit analog-to-digital converter (**Table 2**).

Table 2- *Instrumentations*

Station	Year	Tipology	Sensor	Sensitivity	Bandwitdth	Sps	Transmission
HAGA	2005	Dig. 3C BB	T40s	1500 V/m/s	0.025-50 Hz	100	Radio wireless
HAVL	2005	Dig. 3C BB	T40s	1500 V/m/s	0.025-50 Hz	100	Radio UHF
HCRL	2005	Dig. 3C BB	T40s	1500 V/m/s	0.025-50 Hz	100	Satellite Transmission VSAT
HLNI	2009	Dig. 3C BB	T40s	1500 V/m/s	0.025-50 Hz	100	Satellite Transmission VSAT
HMDC	2005	Dig. 3C BB	T40s	1500 V/m/s	0.025-50 Hz	100	Radio UHF
HVZN	2005	Dig. 3C BB	T40s	1500 V/m/s	0.025-50 Hz	100	Satellite Transmission VSAT
RAFF	2006	Dig. 3C BB	T40s	1500 V/m/s	0.025-50 Hz	100	Satellite Transmission VSAT
SSY	2004	Dig. 3C BB	T40s	1500 V/m/s	0.025-50 Hz	100	Satellite Transmission VSAT

Year=Installation year. Sps stands for Samples per second.

Dataset, selected by searching the IRIS-DMC catalogue, includes 335 teleseisms (see **Appendix A**) with moment magnitude (Mw) 6.0 and larger and epicentral distance (great circle arc between source and station) between 30° and 95°. The distributions, according to their epicentral distance, are given in **Fig. 23** and geographic locations are given in **Fig. 24**.

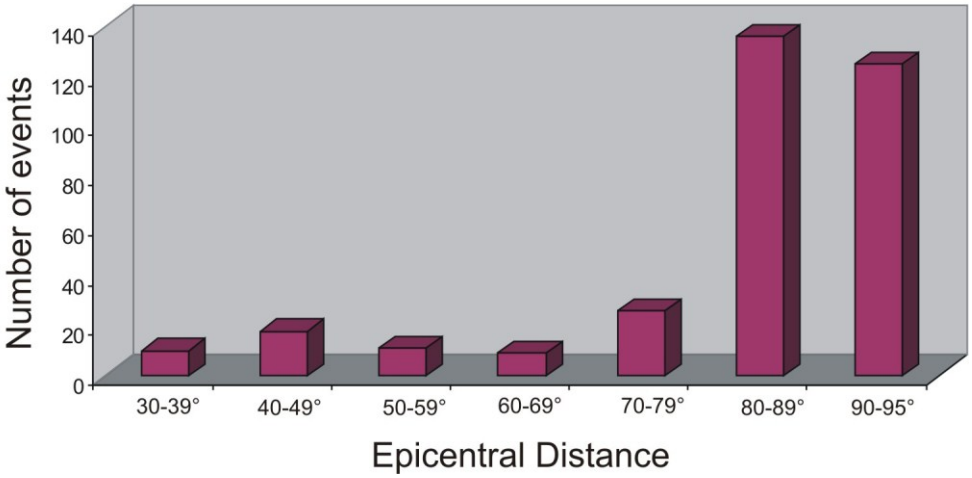

Fig. 23- *Distribution of events according to their epicentral distance.*

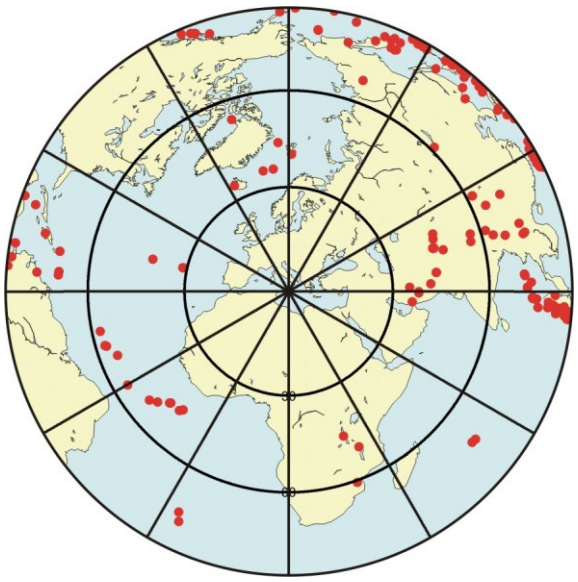

Fig. 24- *Stereographic projection of the Earth centred on SSY station showing the locations of teleseismic events collected between January 2004 and April 2011 (Mw greater than or equal 6.0 occurring between 30 and 95 degrees).*

The magnitude has to be adequately high in order to ensure a large signal to noise ratio, while the spatial constraints on this search are to ensure a steep incidence angle on

the incoming ray path, which maximize incoming wave energy, allow for the transmission of S-waves, and minimize disruptions due to lateral inconsistencies and vertical velocity contrasts (Hobbs and Darbyshire, 2012). The application of these selection criteria resulted in the acquisition of a adequate number of recordings for each station.

After a first visual inspection, through which we excluded seismic waveforms with a low signal to noise ratio, we obtained a dataset of about 1600 three-component records, with a minimum of 117 (HMDC) and a maximum of 297 (RAFF) three-component records for each station.

Receiver functions were computed using the technique developed by Ligorria and Ammon (1999) through a time-domain deconvolution. To improve the signal-to-noise ratio, receiver functions obtained for individual earthquakes were binned, moveout corrected and subsequently stacked. The method has been described in detail in Chapter 3. RFs were derived using 120 s time windows (starting 20 s before the P arrival; 20 s pre-event and 100 s post-event). RFs have been band-passed using a Gaussian filter to smooth high frequency (Ligorria and Ammon, 1999). Four different Gaussian filters, with parameter a=0.5, a=1, a=2.5 and a=5 which exclude frequencies higher than about 0.24, 0.5, 1.24 and 2.5 Hz, respectively, have been used. This permitted to subsequently examine frequency dependences in the observed RFs (Owens and Zandt, 1985; Cassidy, 1992). In the following, the estimated RFs described have frequency cut-offs of 1.24 Hz, unless specifically mentioned otherwise. This frequency band is adequate for crust-scale receiver function analysis. We collected an average of 66 RFs with a high signal-to-noise ratio for each station (receiver functions have been calculated only for earthquakes with a signal-to-noise ratio larger that 2). A better signal-to-noise ratio was achieved by stacking the RFs coming from the same backazimuth direction (Park et alii, 2004). Bins are computed every 10° in BAZ using a 50% overlapping scheme, so each bin shares its events with the two adjacent bins. The spread of event epicentral distance for any one bin was small. In the following, the radial (R) and transverse (T) components of all the receiver functions are sorted by backazimuth and corrected by Ps moveout, along with the backazimuth of each trace (named BAZ). The term ‘backazimuth’ is used to refer to the direction from the station towards the earthquake epicentre, measured clockwise from north. The aim of the moveout correction is to equalize differences in ray parameters in the phase arrival times to allow for direct comparison of receiver functions for earthquakes from different distances. We used a

ray parameter of 0.052 s/km as reference. This representation gives information about laterally varying structures and the complexity of the discontinuities (i.e., presence of dipping, scattering and/or anisotropy). Positive amplitudes are shaded in red and indicate an increasing velocity with depth, whereas negative amplitudes (shaded in gray) show velocity decreasing downwards. The P onset is fixed to be as zero time. The sum traces, in the upper panels, present the stacked P receiver function for each station. Stacking all RF from different BAZ directions suppresses features in the dataset which are generated from local heterogeneities and highlights the bulk 1D structure under the station. The R receiver functions, sorted by the ray parameter, are also shown. We stacked them into bins of 0.002 s/km, moving the bin every 0.001 s/km. This representation helps us to distinguish between converted and multiple phases (Cassidy, 1992). The converted phases exhibit a positive moveout and an increase in amplitude with respect to the direct P with increasing ray parameter, while the multiples present a negative moveout and a constant amplitude with the ray parameter (Cassidy, 1992). It should be pointed out, however, that multiples, conversion interference and data noise also affect pulse amplitudes in complex ways, therefore an error could be introduced into the resulting images.

In principle, we used the simplest and straightforward approach that consists in identifying the P_S phase converted at the crust-mantle boundary and computed crustal thickness from the P_{SMoho}-P time delay, given a bulk crustal velocity. The identification of the Moho P_S conversion is made mainly with two criteria: (1) its expected delay of ~4-5 s with respect to the direct arrival for the Hyblean Foreland where the crust is estimated to be on average about ~30-40 km thick and (2) its moveout with ray parameter (or epicentral distance).

Then, we examined the first seconds of RFs, since shallow crustal structures always strongly influence the first seconds, and dipping high-velocity contrast interfaces and/or anisotropic layers with tilted symmetry axis produce characteristic BAZ patterns of direct P waves and P_S converted phases (Levin and Park, 1997). Therefore, looking at the azimuthal variation in the tangential receiver functions, we looked for polarity flips of the converted phases that are consistent with anisotropic or dipping-interface effects. Several workers have investigated the effects of anisotropy and layer dip on teleseismic wave propagation (Langston, 1977; Cassidy, 1992; Levin and Park, 1998; Savage, 1998; Piana Agostinetti et alii, 2008). Both factors lead to backazimuthal variations in the impulse response, involving traveltime and amplitude, as well as the rotation of P-SV

energy onto the transverse component. Hexagonal anisotropy with a horizontal symmetry axis (i.e. azimuthal anisotropy) typically produces four-lobed backazimuthal patterns with 180° symmetry. However, an axis of symmetry that dips at ~45° produces a two-lobed pattern reminiscent of the effect of a dipping interface (Levin and Park, 1997). An isotropic dipping layer will produce a similar 360° periodicity in azimuth, and also causes rotation of energy from an initial P or SV arrival onto the transverse component (Frederiksen and Bostock, 2000). On the other hand, in the radial components, the amplitudes of converted phases in anisotropic structures will vary with incident backazimuth, but their polarity will not change (Levin and Park, 1998). Some of the features we will see in the following RFs, invite interpretation in terms of either inclined boundaries, or else anisotropic seismic velocity. In this thesis, for all stations, polarity flips of pulses will be interpreted as produced by dipping interfaces.

Afterwards, we applied the slant stacking technique of Zhu and Kanamori (2000) to try to constrain the bulk crustal V_P/V_S and validate the estimate of crustal thickness. The slant stacking approach essentially transforms the receiver function stacks from the time domain to the H-V_P/V_S domain. The average V_P used in the grid search was obtained from previous refraction profiles in the area (Continisio et alii, 1997; Cassinis et alii, 2003) and from tomographic inversions (Scarfì et alii, 2007). Two assumed P-wave velocity of 5.7 and 6.2 km/s have been considered. An a posteriori comparison of the two computed values provided an estimates of the stability of the results. Also, a fixed set of weights (0.6, 0.3 and 0.1) for the three converted and reverberated phases (P_S, P_PP_S, and P_PS_S+P_SP_S phases, respectively), for all stations have been chosen to obtain a more homogeneous result for all the station, both in depth and in error estimates. These weights are proportional to the signal/noise ratios for the three phases (among them, the P_S has the highest signal/noise ratio, so it is given a higher weight than the other two). When certain phases were not well observed, we were forced to modify the default weighting factors. In these cases we used weightings of 0.8, 0.1, 0.1 for w_1, w_2, and w_3, respectively. Because this method compares arrivals of the P-wave coda to the initial P-wave arrival it is robust to different V_P values, meaning that the results should not vary greatly for different assumed P-wave speeds. In order to test the stability of the results, two standard deviations for H and V_P/V_S have been estimated for the trials by using the bootstrap approach (Efron and Tibshirani, 1991). For each station, data have been resampled by randomly selecting individual receiver functions to create a set of 200 bootstrapped receiver function stacks. Each new data set contains the same number of

RF as in the original one but may contain duplicates of receiver functions. The grid search is repeated for each new dataset and a standard deviation of the highest values forms the error estimate for the original grid search result. The covariance matrix is then obtained by applying the standard formulae for the mean, variance, and covariance to the bootstrap estimates. While this process gives good results in fairly simple region (i.e., where we expect subhorizontal interfaces and where the observation of multiples permits a more reliable determination of the V_P/V_S ratio and crustal thickness), it could be biased in complex region, due to inhomogeneous BAZ sampling of the P wave dataset (Zandt and Ammon, 1995; Zhu and Kanamori, 2000; Tomlinson et alii, 2006). As observed in other regions, the receiver function stacking method has limitations in the presence of a dipping Moho, a gradient-type crust-mantle boundary instead of a sharp, or in sedimentary environments, where the multiples from the sediment-bedrock interface may overlap with the P_S-converted phase at the Moho. For the stations for which the above methodology is not applicable, the grid search maxima are poorly constrained or indicate implausible values due to the superposition of unrelated phases. In these cases, information on the crustal thickness and V_P/V_S ratio from nearby stations or other sources can help to resolve the ambiguity. In general, the application of Zhu and Kanamori method to dipping structure leads to an underestimation of the Moho depth and an overestimation of the V_P/V_S ratio (see Lombardi et alii, 2008).

As a last step, forward modelling for calculation of synthetic receiver function was achieved using the approach of Frederiksen and Bostock (2000). This approach allows the inclusion of dipping layers in simple models to replicate the main features of the RFs. Information on depth of the Moho, intracrustal discontinuities and sedimentary layers, provided by the grid search method, have been used to construct simple initial models for layered crustal structure. Additional discontinuities were added if remaining peaks in the RF indicated additional *P*-to-*S* converted phases.

4.2 Data Examples and Crustal Thickness Calculation

Subject to data availability for each station, we analyzed between 2 and 8 years of seismicity, which resulted in a number of usable receiver functions from 36 (HLNI) to 99 (RAFF). Those extremes reflect mainly different (1) microseismic noise in a coastal setting and at remote inland stations, together with some technical problems for some of the stations, (2) short or long recording period, (3) tectonic environment and (4) location.

For the study area, the selected teleseisms provided an uneven coverage in both backazimuth and epicentral distance (**Figs. 23** and **24**), as the global seismicity recorded in Italy samples mostly backazimuths in the NE (southeastern Asia) and SW (central and south America) quadrants and the largest epicentral distances (>70°) in the range useful for RF analysis (usually 30-95°), while northwestern and southeastern backazimuths are less represented. Nevertheless, the seismic events recorded at each station sample all four of the backazimuth quadrants and there are several selected teleseisms with epicentral distance less than 70°.

Hereafter, the discussion of the results have been organized into three groups (first group includes SSY, HCRL, HAGA, HVZN stations; second group includes HMDC, HAVL stations; third group includes HLNI, RAFF stations) based on the different recording period, tectonic environment and location. We highlighted the main characteristics of the observed RFs for all the 8 considered broadband stations and the most important results. Moho depth under each station was obtained by subtracting the station elevation from the computed crustal thickness.

4.2.1 Results by Stations

4.2.1.1 SSY

Firstly, we analyze data from SSY station (one of the best stations used in this study), where the seismic longest recording period (since 2004; see **Table 2**) has been observed. Of the many teleseismic events processed (335) from 8 years of data, 53 events with appropriate backazimuth and distance range (**Fig. 25**) were chosen for further analysis. Backazimuth information between 100 and 150, 170 and 230, 290 and 350 degrees are nevertheless not available. This station, located in the central-eastern part of the Hyblean Foreland on solid bedrock (calcarenitic limestone), shows great intracrustal complexity and relevant signal in the transverse component of the receiver functions. The stacked P receiver function (upper panel in **Fig. 26)**, displays a relatively high amplitude first arriving P-wave (T=0.0 s), followed by a large phase at approximately 2.0 seconds (s) and a relatively lower amplitude wave arrival at 3.9 s. A strong negative pulse with large amplitude is observed 9 s after the initial pulse. In the image, red are positive and gray are negative conversions.

By considering the radial and tangential component traces we observe several notable features:

- A strong, clean, direct P pulse (at T=0.0 s) with no phase lag below 120°

backazimuth. A time shift of ~0.4 s, between 160 and 290 degrees backazimuth, is observed. Delay of the pulse (from zero time) indicates low velocities in the near-surface layer beneath the station. This delay results from the superposition of the direct P wave and P-to-S converted (P_S) waves generated at the basement-sediment interface.

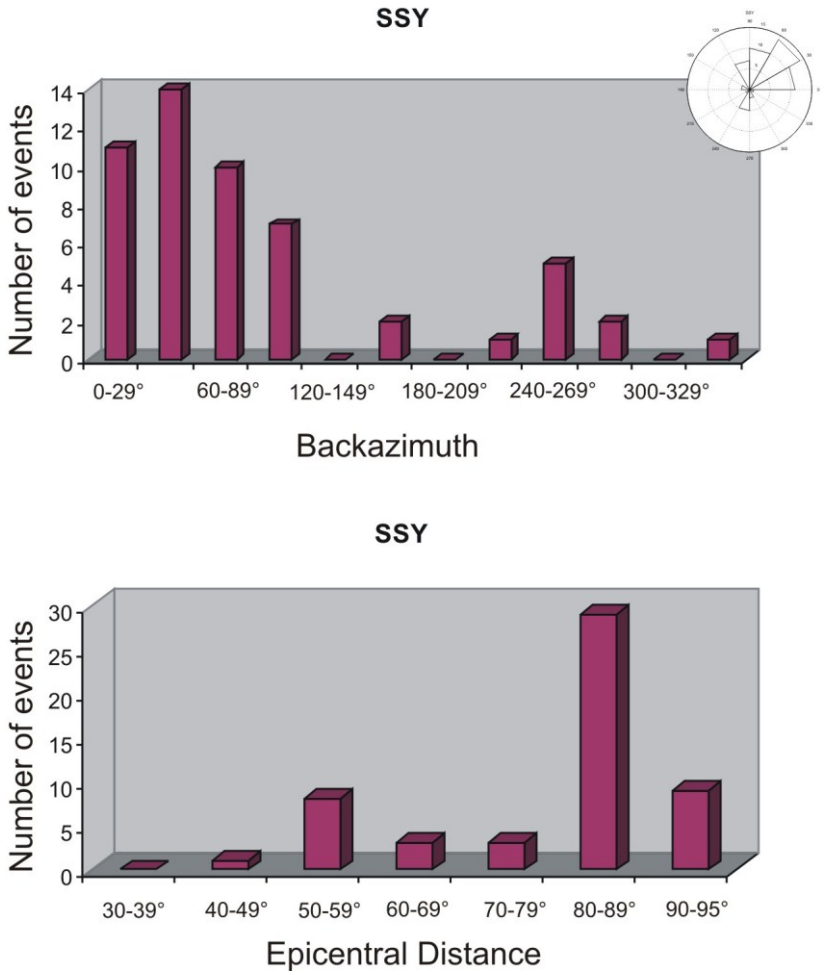

Fig. 25- *Distribution of events according to their (a) backazimuth, (b) epicentral distance with respect to SSY station.*

- A first positive pulse at 2 s (the largest pulse after the P onset). This phase is seen for some but not all of the backazimuths (missing in the restricted backazimuth range of 230°-300°) on the RFs, suggesting lateral variation of the crustal structure beneath the station.

- Then, a positive low amplitude phase at about 3.9 s. It can be related to the P_S conversion at a roughly 30 km depth Moho. Its low amplitude can be due to a weak velocity contrast and/or to a deterioration caused by crustal multiples. If we convert the P_S delay times to crustal thickness assuming an average P-wave crustal velocity between 5.7 and 6.2 km/s (surface geology and previous studies were used as a priori

information on the velocity profile at each station) and a V_P/V_S of 1.73, the depth of the discontinuity generating the 3.9 s pulse is found at ~29-32 km (**Table 3**).

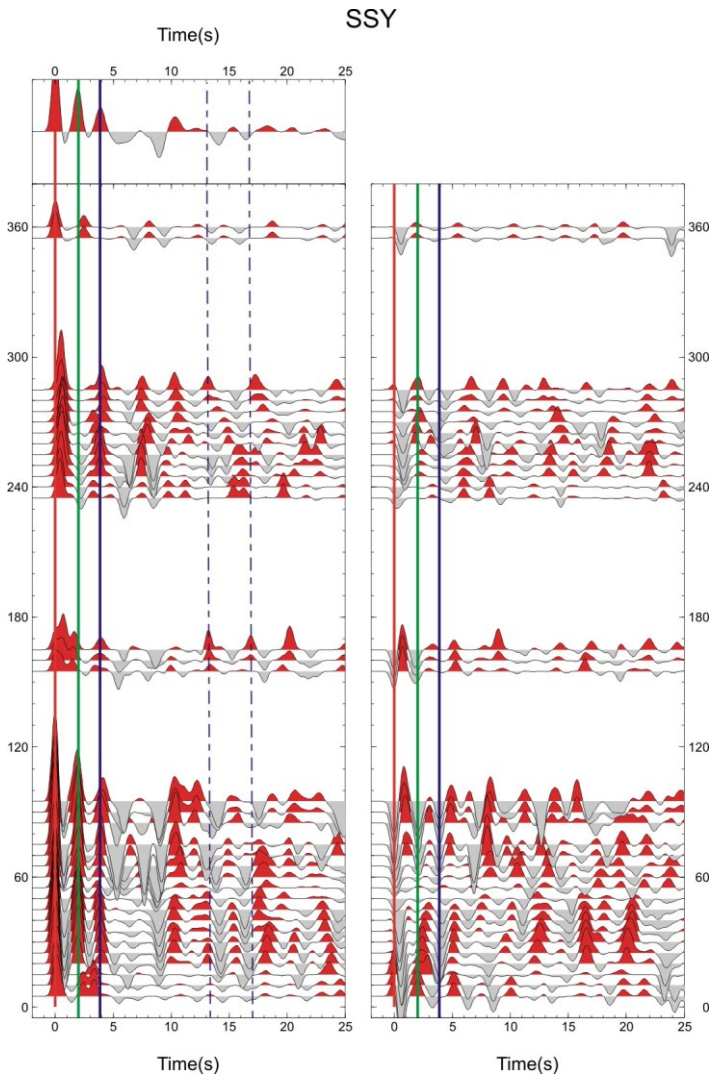

Fig. 26- *Binned RF dataset for Radial (left) and Transverse (right) components plotted as a function of the time (s) and the BAZ (°) at SSY station. The direct P-wave arrival time is taken as the origin time. Red and gray areas indicate negative and positive pulses, respectively. Upper panel displays the average RF. Blue line marks the pulse related to the crust-mantle transition (see text for details).*

This assumption is in agreement with Moho-depth estimates from previous receiver function studies (Piana Agostinetti and Amato, 2009). The first and second Moho multiples (P_PP_S=1M=positive multiple at roughly 13.5 s and P_SP_S+P_PS_S=2M=negative multiple at about 17.5 s) are not significantly visible in the data (dashed blue lines in **Fig. 26**). The P_S phase has a relatively constant arrival time for most azimuths, although it appears to arrive slightly latest, at ~4.1-4.2 s, for backazimuths between 270 and 290°. Such changes in the time of the radial P_S with backazimuth may indicate the presence of

dipping structure (Cassidy, 1992; Levin and Park, 1997). The latest arrival time (approaching from BAZ=270°) indicates either that waves arriving from the west are travelling updip, or that the average crustal velocity is slightly slower to the west of the station (Cassidy, 1992); on the other hand, waves travelling downdip (BAZ=90°) generate the smallest and earliest arriving P_S phases.

Table 3- *Delay times observed and computed and depth values.*

Station	Vp/Vs	Vp	H	Ps	PpPs	PpSs+PsPs	Vp/Vs	Vp	H	Ps	PpPs	PpSs+PsPs
HAGA (Ps=3.7s)	1.73	5.7	28	3.69	13.02	16.71	1.73	6.2	31	3.71	12.96	16.68
HAVL (Ps=4.9s)	1.73	5.7	37	4.87	17.2	22.08	1.73	6.2	40	4.87	17	21.88
HCRL (Ps=4.0s)	1.73	5.7	30	3.95	13.95	17.9	1.73	6.2	33	4.02	14.03	18.05
HLNI (Ps=4.2s)	1.73	5.7	32	4.22	14.88	19.1	1.73	6.2	35	4.2	14.66	18.87
HMDC (Ps=5.1s)	1.73	5.7	39	5.14	18.13	23.28	1.73	6.2	42	5.12	17.85	22.97
HVZN (Ps=4.8s)	1.73	5.7	37	4.81	16.97	21.78	1.73	6.2	40	4.81	16.79	21.61
RAFF (Ps=4.4s)	1.73	5.7	34	4.41	15.58	19.99	1.73	6.2	36	4.38	15.3	19.69
SSY (Ps=3.9s)	1.73	5.7	30	3.89	13.71	17.61	1.73	6.2	32	3.9	13.6	17.5

In the tangential component traces (**Fig. 26**), considerable energy indicating a degree of structural complexity is visible. Qualitative analysis of RF features, such as moveouts and polarity flips with source backazimuth, highlights the probable dip and anisotropy of the crustal and mantle layers beneath this station. In particular, we can observe:

- Some transverse energy at T=0.0 s. The polarity of this pulse appears to change from positive to negative between 40 and 240°.
- The positive pulse at about 2 s displays a flip of polarity near 40° backazimuth; opposite to this direction (220° or -140° backazimuth) the polarity of these phases flips as well. The transverse amplitude is generally zero for arrivals from the updip or downdip directions and largest for arrivals travelling along the strike direction of the interface (40+90=130° or 310° in this example). This phase suggests different hypotheses: (a) it is a crustal multiple; (b) it is a P_S converted phase from a dipping interface at sub-crustal depth. If we assume an average P-wave crustal velocity of 3.4 km/s and a V_P/V_S ratio of 1.73, the phase at 2 s could be the first multiple of a shallow interface located at a depth of ~2.5 km (if H=2.5 km and V_P =3.4 km/s: P_S=0.54 s, P_PP_S=1M=1.98 s, P_SP_S+P_PS_S=2M=2.53 s). However, from geological interpretative cross-sections we have some suggestions about the crustal structure (**Fig. 4**, profile b).

Continisio et alii (1997), beneath the Hyblean Foreland, find 3 layers in which V_P velocities are 3.6 km/s for the first 2.0 km, 5.4 km/s until 10 km, 6.0 km/s until 30 km depth, and then they find mantle velocities. In this case, if we assume an average P-wave crustal velocity of 4.7 km/s (an average value up to 10 km) and a V_P/V_S ratio of 1.73, the phase at 2 s could be the P_S of a shallow interface located at a depth of ~12.5 km (if H=12.5 km and V_P =4.7 km/s: P_S=1.97 s, P_PP_S=1M=7.13 s, P_SP_S+P_PS_S=2M=9.10 s). In this case, we propose the presence of a mid-crustal interface (H=12.5 km) with P_S conversion arriving with the multiples from the shallow discontinuity at ~2.5 km depth. The reverberations from this proposed interface interfere destructively with the Moho signal underneath the station, explaining the weak amplitudes identified in the radial component (**Fig. 26**).

- The phase at 4 s shows an amplitude on the T component not null, however the fact that this phase is not associated with a prominent phase on the transverse RFs suggests a subhorizontal Moho geometry with weak or zero anisotropy at the crust-mantle transition layers. The strike of this interface is constrained by the minimum time-delay of this phase at about 90° backazimuth to be roughly 180°, while determining its dip is more tricky. Accordingly with this observation, in the following modelling stage, we constrain the Moho dip to be 10°. It is clear that the uneven coverage in the backazimuth could hide the polarity changes and/or the conversions and reverberations associated with the surface sedimentary layers could potentially overwhelm the P_S conversion from the Moho discontinuity.

To check if those phases are the converted and/or the multiple, in **Fig. 27** we plot the stacked receiver functions sorted by the ray parameter. As we can observe, the selected phases (at 2 and 4 s) follow a positive moveout with increasing ray parameter. In particular the amplitude of the P_S increases with the ray parameter (and also the arrival time), while the multiples shows constant amplitude and decreases in time arrival (Cassidy, 1992).

As stated above, the RFs for SSY station are generally consistent with a mid-crustal discontinuity at about 12 km and with a Moho interface at about 30-33 km, although there is some inconsistency with the dip direction of this discontinuity. At the least the changes in the transverse RFs suggest lateral changes in crustal structure beneath the station. Clearly, simple estimates of crustal thicknesses based on P_S-P times cannot uniquely define detailed crustal models.

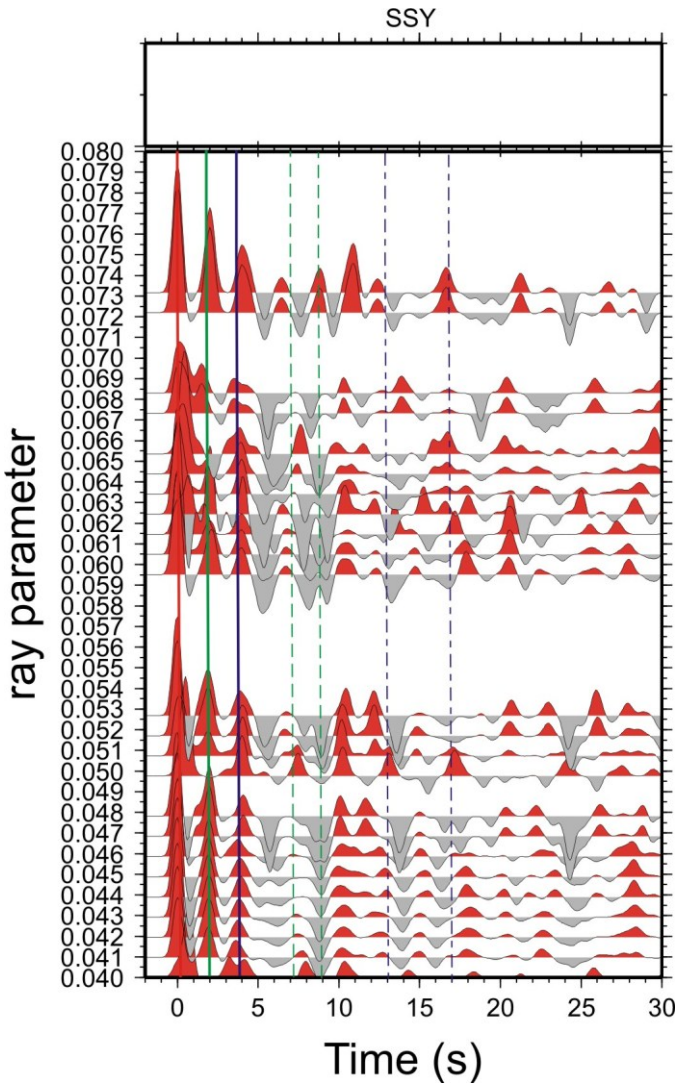

Fig. 27- *Radial receiver functions sorted by the ray parameter, computed at SSY station. Blue line marks the pulse related to the crust-mantle transition (see text for details).*

Then, we applied the receiver function stacking technique developed by Zhu and Kanamori (2000), involving a grid search in the H and V_P/V_S space (**Fig. 28**). We used steps of 0.1 km and 0.01, respectively. We searched for the maximum-stacked amplitude in the Moho depth (H) versus V_P/V_S domain in the interval of 23 to 43 km depth and 1.6 to 1.90 for the V_P/V_S ratio. Primary phase and the two multiple conversions were weighted with the values of 0.8, 0.1, 0.1, respectively. In **Fig. 28**, we show the grid search result using a fixed crustal V_P value of 5.7 km/s. The yellow shaded area displays the stacking function, from blue (lower) to yellow (higher) values. For this station, we found that the stacking function has two clearly distinct maxima at depth. The first peak identifies V_P/V_S at 1.87 and H at 25 km; for the second peak: V_P/V_S=1.66 and H=33 km. In the case of multiple peaks in $S(H, V_P/V_S)$, information on the crustal thickness and V_P/V_S ratio from nearby stations or other sources can help to resolve the ambiguity.

In this case, first peak shows an average value of the V_P/V_S closer to those ones obtained from Scarfì et alii (2007) and Piana Agostinetti and Amato (2009). The bootstrap re-sampling technique (Efron and Tibshirani, 1991) was used to test the stability of the slant stacking result. We base the statistics on 200 bootstrap replications which means we repeat the stacking procedure 200 times with a resampled dataset selected randomly from the original dataset. The stacking surface (normalized to 100%) is shown in **Fig. 28** along with the 1σ confidence ellipses (red) from the bootstrap analysis. This station yields a V_P/V_S of 1.87±0.06 and thickness of 25.0±2.1 km.

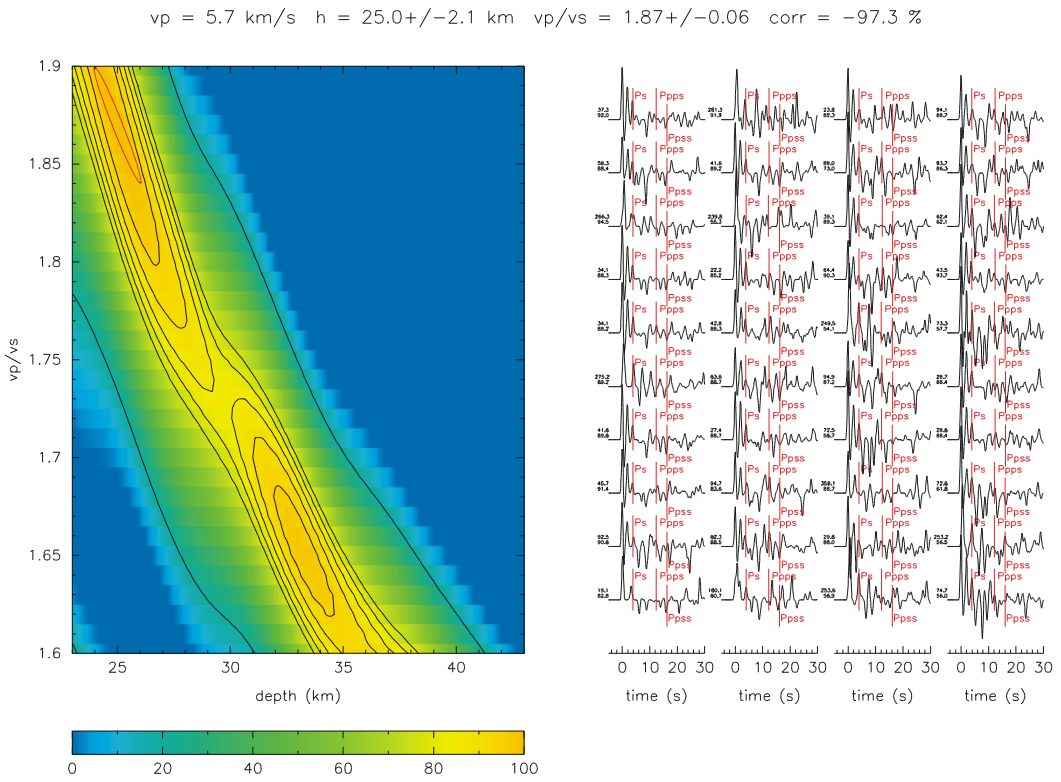

Fig. 28- *Grid search results for SSY station according to Zhu and Kanamori (2000) method. A fixed crustal V_P value of 5.7 km/s was assumed.*

The correlation coefficient (the covariance matrix cross term) exhibits a large and negative value (-97.3 %). This means that even though the usage of the arrival times of three different phases in the stacking technique reduces the trade-off degeneracy in the determination of H and V_P/V_S (Zhu and Kanamori, 2000), this trade-off is still present with different degrees in the analysis. The large correlations imply that the estimated values for V_P/V_S and H do not vary independently within the uncertainty limits. In **Fig. 29** the grid search result using a fixed crustal V_P value of 6.2 km/s is shown. Even in

this case, two distinct maxima at depth have been found.

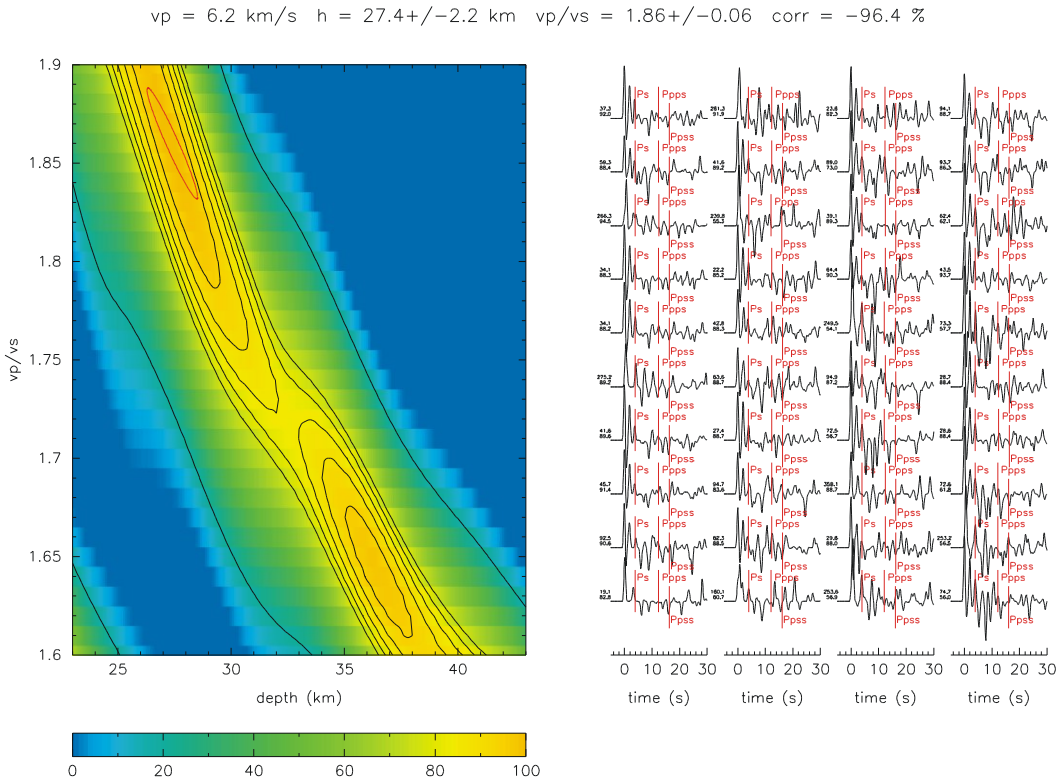

Fig. 29- *Grid search results for SSY station according to Zhu and Kanamori (2000) method. A fixed crustal V_P value of 6.2 km/s was assumed.*

To decipher the crustal parameters, we performed forward modelling (**Fig. 30**) for a number of simple crustal models by using the approach of Frederiksen and Bostock (2000), which allows for including dipping planar interfaces. For the purposes of this study, we used a model parameterization (layer thickness and dip) derived from the qualities retrieved in the above observations, while published and averaged velocities for the crust and upper mantle have been used. After multiple trials the following result has been achieved: • The shallower layer is modelled at 2.5 km depth and shows northwest striking (N160°), south-west dipping interface. • A mid-crustal discontinuity is modelled at 12.5 km. • The Moho is modelled at 30.5 km depth and dips 10° westwards (strike N190°). Subtracting the station elevation (602 m) from the crustal thickness, the Moho is modelled at roughly 30 km.

The principal features of the RFs analysis can be summarized into the following main points: (1) The stacking of the 53 receiver functions for station SSY gives a crustal thickness of 25.0±3.1 km with a crustal V_P/V_S ratio of 1.87±0.08. (2) The predicted

Moho P_S arrival time agrees with the receiver function profile which shows a strong converted phase at 3.9 s following the direct P arrival. (3) This phase has the expected increase of amplitude and time delay with ray parameter for a primary converted phase. (4) The synthetic models (**Fig. 30**), based on a simple-layered structure including dipping layers reproduce the major characteristics of the real data (**Fig. 26**). (5) There is a good correlation between previous studies, stacked values and synthetically modelled estimates. The inferred crustal thickness of 30 km is slightly greater than the value of 28.6±6.8 km found from Piana Agostinetti and Amato (2009) just beneath this station.

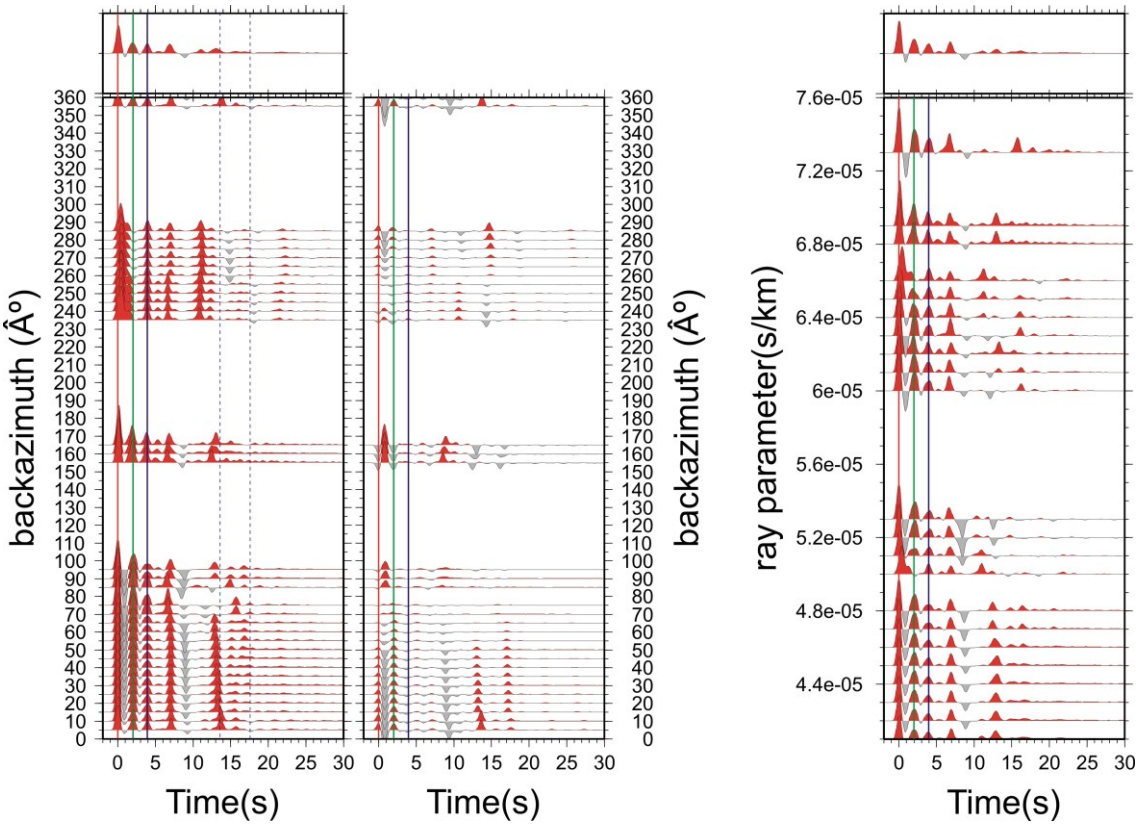

Fig. 30- *Synthetic radial and transverse RF components vs. backazimuth (on the left), computed at SSY station by using the approach of Frederiksen and Bostock (2000). Synthetic radial RF component vs. ray parameter (on the right).*

4.2.1.2 HCRL

HCRL seismic station is located about 15 km northwards from SSY station. It includes 77 events with appropriate backazimuth and distance range (**Fig. 31**). Backazimuth information between 100 and 120, 170 and 220, 290 and360 degrees are nevertheless not available. As SSY station, HCRL shows great intracrustal complexity and relevant signal in the transverse component of the receiver functions. The stack

(**Fig. 32**) is characterized by a relatively high amplitude first arriving P-wave, followed by a large phase at approximately 2.0 s and two relatively lower amplitude wave arrivals at approximately 4.0 and 5.0 seconds (s). The identification of the pulse corresponding to the Moho conversion is unclear as two pulses (4 and 5 s) are present within the time range of possible Moho conversions, nevertheless the pulse at 4 s shows a positive moveout with increasing ray parameter (**Fig. 33**), while the pulse at 5 s decreases with increasing ray parameter. The identification of the Moho with the earlier pulse leads to a shallower Moho and to a smoother transition toward the surrounding stations (see SSY station), whereas the later pulse is assumed to be related to a subcrustal discontinuity.

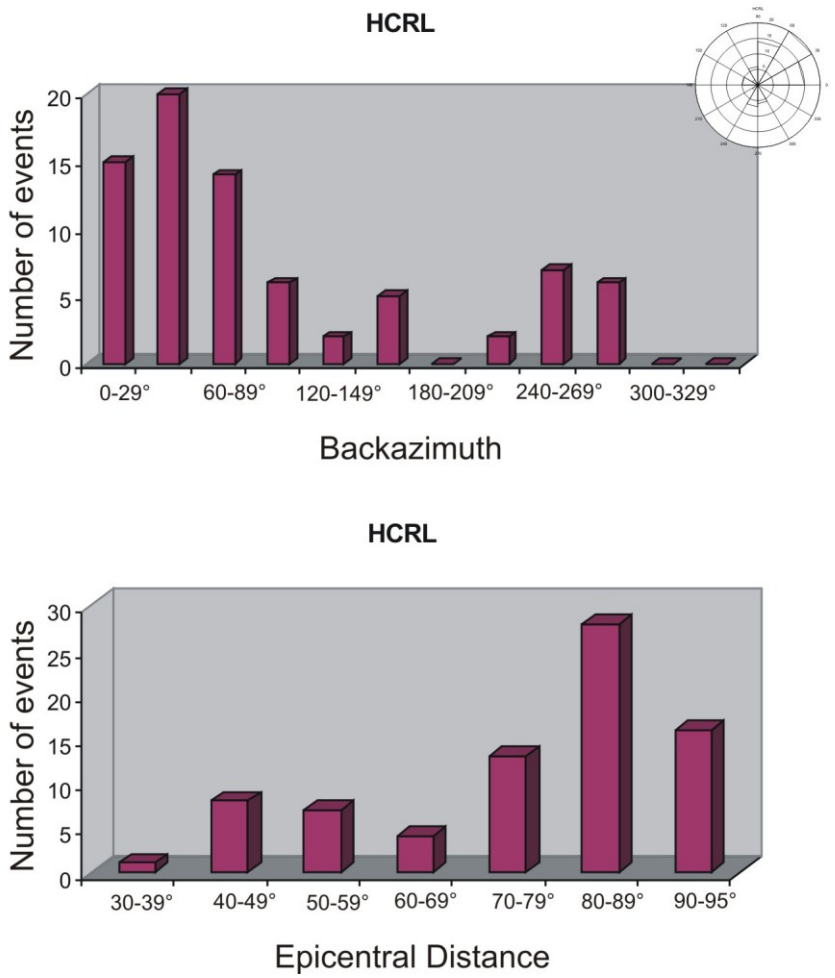

Fig. 31- *Distribution of events according to their (a) backazimuth, (b) epicentral distance with respect to HCRL station.*

By considering the radial and tangential component traces we observe:

- Radial RFs (**Fig. 32**) are very complex in the first 1.5 s, with a large amplitude pulse 0.5-1.5 s after the direct P arrival in the restricted backazimuth range of 40-100°.

We interpret this large pulse to represent a P_S converted pulse from the bottom of a thick deposit of low-velocity sediments. Where the sedimentary layer is thinner, the interference of the P_S conversion and the direct P arrival produce a composite peak which is shifted in time from 0 seconds. Reverberations inside the sedimentary layers contribute to the pulse complexity over 1-3 s.

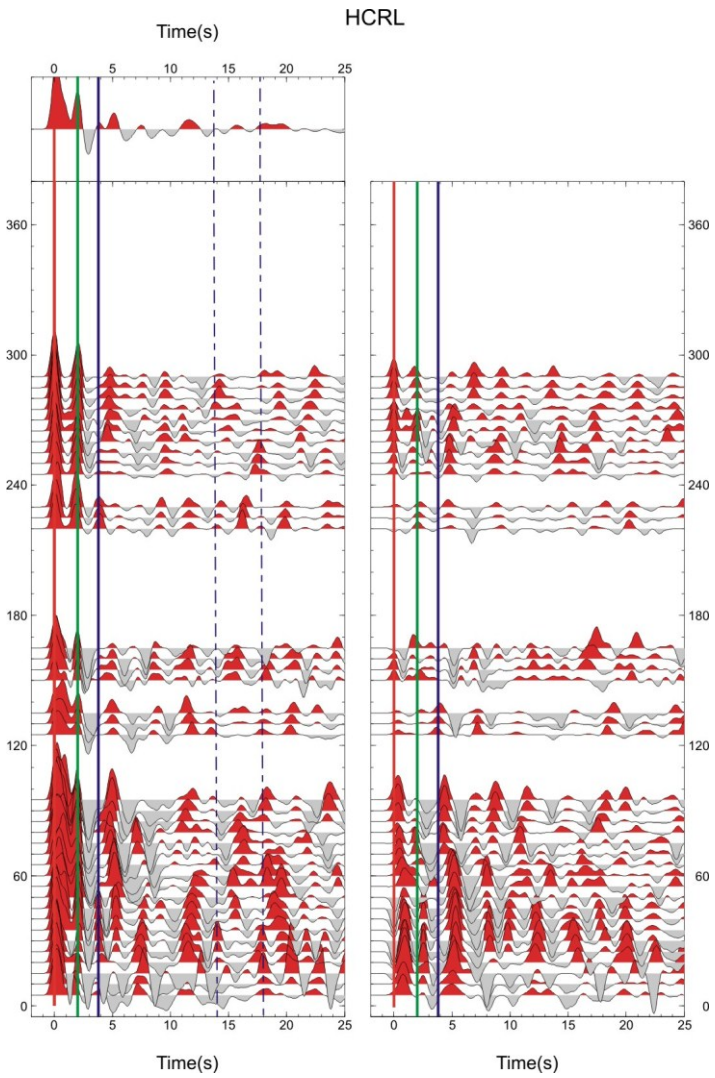

Fig. 32- *Binned RF dataset for Radial (left) and Transverse (right) components plotted as a function of the time (s) and the BAZ (°) at HCRL station. The direct P-wave arrival time is taken as the origin time. Red and gray areas indicate negative and positive pulses, respectively. Upper panel displays the average RF. Blue line marks the pulse related to the crust-mantle transition (see text for details).*

- A first positive pulse at 2 s (the largest pulse after the P onset). This phase is seen for all of the backazimuths and it can be related to a shallow discontinuity.
- Then, we observe a positive pulse at 4.0 s behind the direct arrival. Its low amplitude can be due to a weak velocity contrast and/or to a deterioration caused by

crustal multiples arriving in the same time interval. If we translate into depth the arrival time of the converted phase using an average V_P/V_S ratio of 1.73 and an average P-wave crustal velocity of between 5.7 and 6.2 km/s, its crustal thickness is ~30-33 km (**Table 3**). The first and second Moho multiples (P_PP_S=1M=positive multiple at ca. 14.0 s and $P_SP_S+P_PS_S$=2M=negative multiple at ca. 18.0 s) are not clear (dashed blue lines in **Fig. 32**), since strong velocity jumps in the uppermost crustal layers might hide the deeper Moho conversion and multiple reflections. The P_S phase has a relatively constant arrival time for most azimuths, although it is not observable in the all available backazimuths.

- Then, we observe a pulse positive still clearer at 5.0 s. We attribute this pulse to be the first multiple of a subcrustal discontinuity 8.5 km depth. If we assume an average P-wave crustal velocity of between 4.7 and 5.0 km/s, and a V_P/V_S ratio of 1.73, the P_S, the first and second multiples of a subcrustal discontinuity 8.5 km depth should be observed at ca. P_S=1.4 s, P_PP_S at ca. 4.9 s and $P_SP_S+P_PS_S$ at ca. 6.2 s. The phase at 5 s has a relatively constant arrival time for most azimuths, although it appears to arrive slightly latest, at ~5.1–5.2 s, for backazimuths between 20° and 60° and earliest for backazimuth of 260-290°.

Considerable energy is visible in the tangential component traces. In particular:

- Some transverse energy is present at 0 s.
- The phase at 2.0 s shows an amplitude on the T component not null and varies with the backazimuth angle (polarity change occurs at N150° and N150+180=N330°). Strike of the dipping interface is 150+90=240° or 60° in this example. This phase could be the first multiple of a shallow interface (H=2.7 km and V_P=3.4 km/s: P_S=0.58 s, 1M=2.14 s, 2M=2.73 s).
- The phase at 4.0 s shows an amplitude on the T component not null and a polarity change occurring at roughly 80°. It is clear that the uneven coverage in the backazimuth could hide the polarity changes and/or the conversions and reverberations associated with the surface sedimentary layers could potentially overwhelm the P_S conversion from the Moho discontinuity.

Then we plot the stacked receiver functions sorted by the ray parameter (**Fig. 33**). As we can observe, the selected converted phase (at 0.5 and 4.0 s) follow a positive moveout with increasing ray parameter, while a constant moveout at 2.0 s and a negative moveout at 5 s (first multiples) are observed. The pulse at 1.4 s (P_S of a subcrustal discontinuity 8.5 km depth) could potentially overwhelm.

Trying to estimate the Moho depth and V_P/V_S for HCRL station (**Fig. 34)**, we encountered some problems with the slant stacking technique (Zhu and Kanamori, 2000). We used steps of 0.1 km and 0.01, respectively. We searched for the maximum-stacked amplitude in the Moho depth (H) versus V_P/V_S domain in the interval of 29 to 41 km depth and 1.6 to 1.9 for the V_P/V_S ratio. Primary phase and the two multiple conversions were weighted with the values of 0.8, 0.1 and 0.1, respectively. The yellow shaded area displays the stacking function, from blue (lower) to yellow (higher) values. For this station, the receiver function stacking technique does not provide a stable solution, showing two maxima at depth.

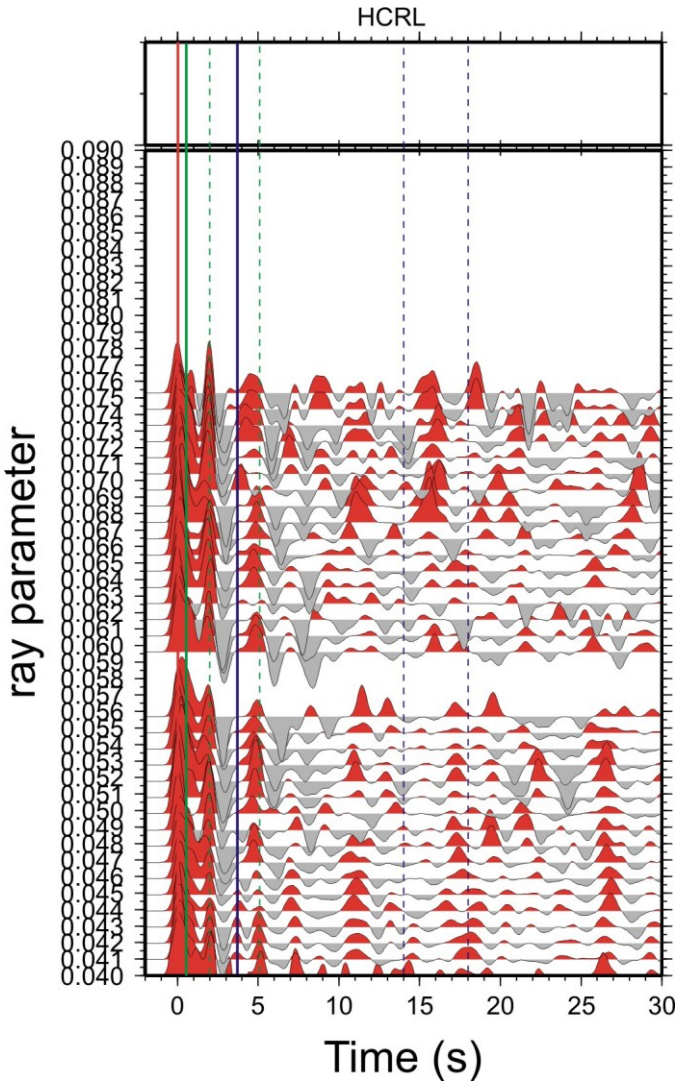

Fig. 33- *Radial receiver functions sorted by the ray parameter, computed at HCRL station. Blue line marks the pulse related to the crust-mantle transition (see text for details).*

For the first peak: V_P/V_S=1.83 and H=33.1 km; for the second peak: V_P/V_S=1.71 and H=38.6 km. First peak (V_P/V_S=1.83 and H=33.1 km) agrees with the receiver function

profile which shows a strong converted phase at 4.0 s and it is closer to the average value of the V_P/V_S obtained for this area by Scarfì et alii (2007) and Piana Agostinetti and Amato (2009). Similar values are found at the neighbouring stations (SSY and HAGA). To estimate the uncertainties, we used a bootstrap approach (Efron and Tibshirani, 1991). We base the statistics on 200 bootstrap replications which means we repeat the stacking procedure 200 times with a resampled data set selected randomly from the original data set. This station yields a V_P/V_S of 1.83 ±0.06 and thickness of 33.1±2.7 km. The correlation coefficient (the covariance matrix cross term) exhibits a large and negative value (-97.9 %).

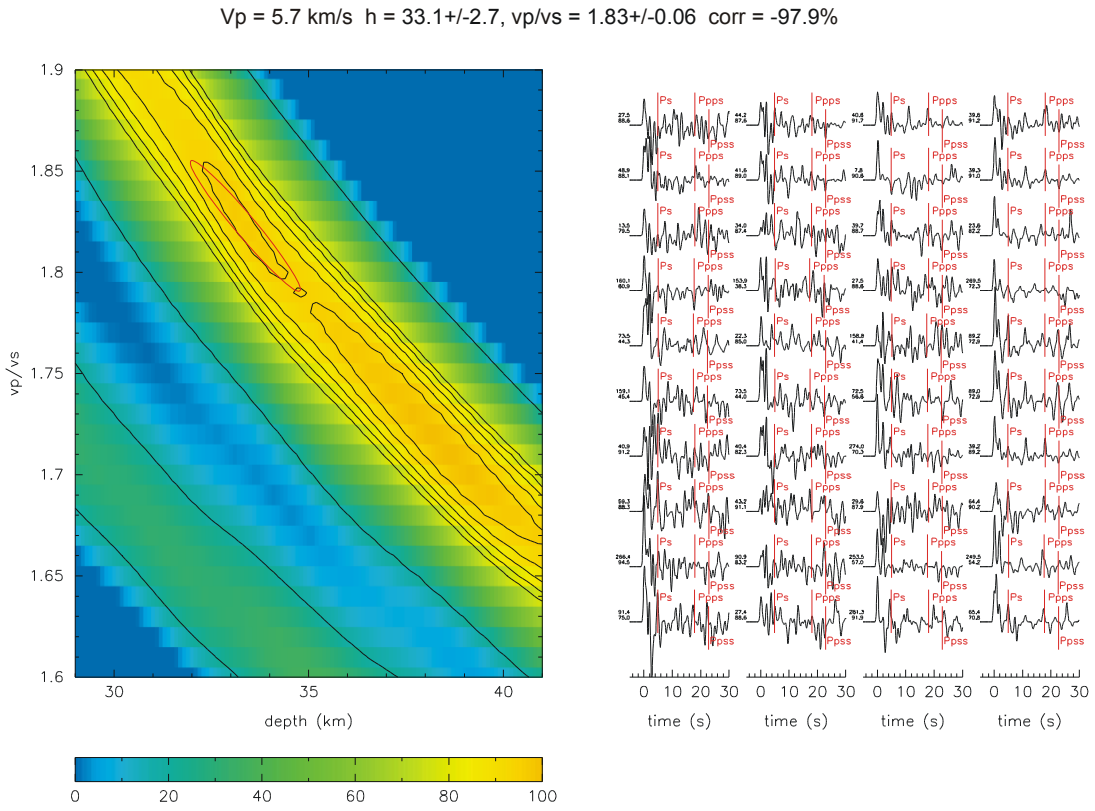

Fig. 34- *Grid search results for HCRL station according to Zhu and Kanamori (2000) method. A fixed crustal V_P value of 5.7 km/s was assumed.*

To decipher the crustal parameters, we performed forward modelling (**Fig. 35**) for a number of simple crustal models by using the approach of Frederiksen and Bostock (2000). We used a model parameterization (layer thickness and dip) derived from the qualities retrieved in the above observations, while published and averaged velocities for the crust and upper mantle have been used. After multiple trials the following result has been achieved: • The shallow layer is modelled at 2.7 km depth and shows northeast

striking (N50°), 15° southeast dipping interface. • A mid-crustal discontinuity is observed at 8.7 km, while the Moho is modelled at 30.7 km depth and dips 10° west (strike N190°). Subtracting the station elevation (190 m) from the crustal thickness, the Moho is modelled at 30.5 km.

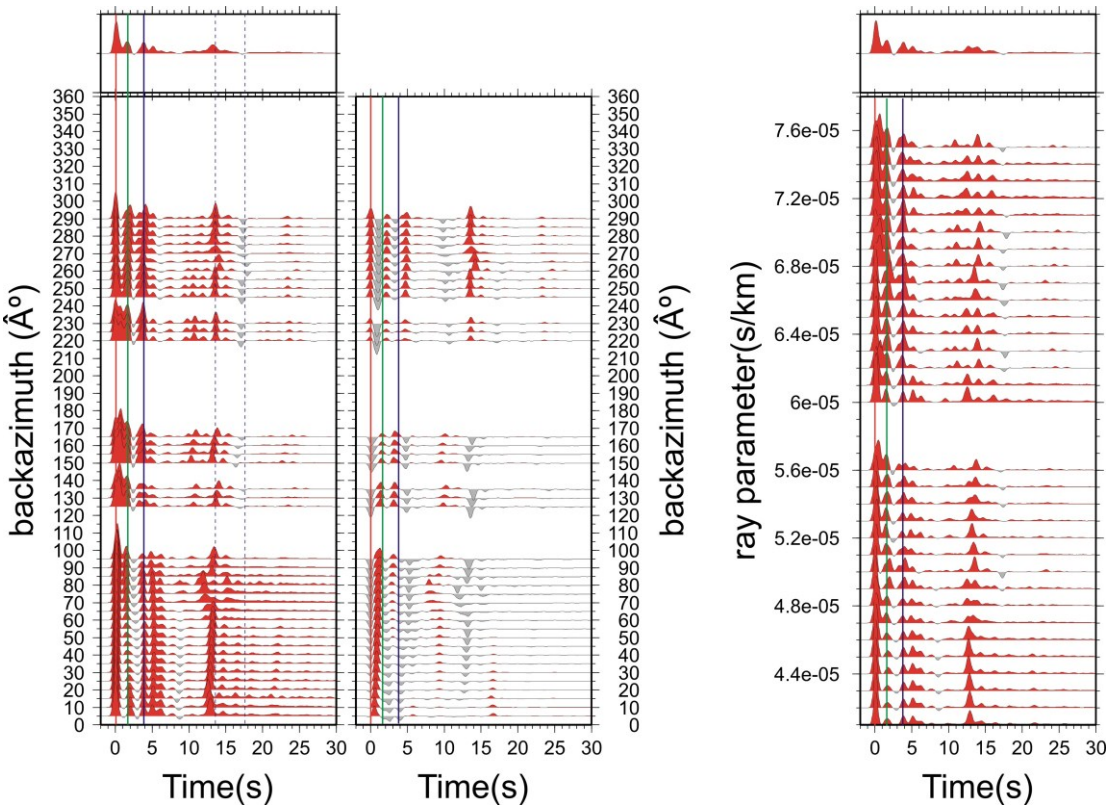

Fig. 35- *Synthetic radial and transverse RF components vs. backazimuth (on the left), computed at HCRL station by using the approach of Frederiksen and Bostock (2000). Synthetic radial RF components vs. ray parameter (on the right).*

The principal features of the RFs analysis can be summarized into the following main points: (1) The stacking of the 77 receiver functions for station HCRL gives a crustal thickness of 33.1±2.7 km with a crustal V_P/V_S ratio of 1.83 ±0.06. (2) This value agrees with the receiver function profile which shows a converted phase at 4.0 s following the direct P arrival, which (3) has the expected increase of amplitude and time delay with ray parameter for a primary converted phase. Nevertheless, its low amplitude and the complicated receiver functions are to attribute to the interference of the P_{SMoho} phase with multiples from the sedimentary layer(s). (4) The synthetic models (**Fig. 35**), based on the simple-layered structure including dipping layers, reproduce the major characteristics of the real data (**Fig. 32**). (5) There is a good correlation between stacked values and synthetically modelled estimates. It should be pointed out, however, that no

estimate from previous work is available for HCRL. The value calculated here, 30.5 km, therefore cannot be tested against previous work.

4.2.1.3 HAGA

Station HAGA is located in the central-eastern part of the Foreland, along the coastal setting, about 16 km from SSY station and 11 km from HCRL station. This station includes 97 events with appropriate backazimuth and distance range (**Fig. 36**). Backazimuth information between 100 and 120, 170 and 220, 290 and 360 degrees are nevertheless not available.

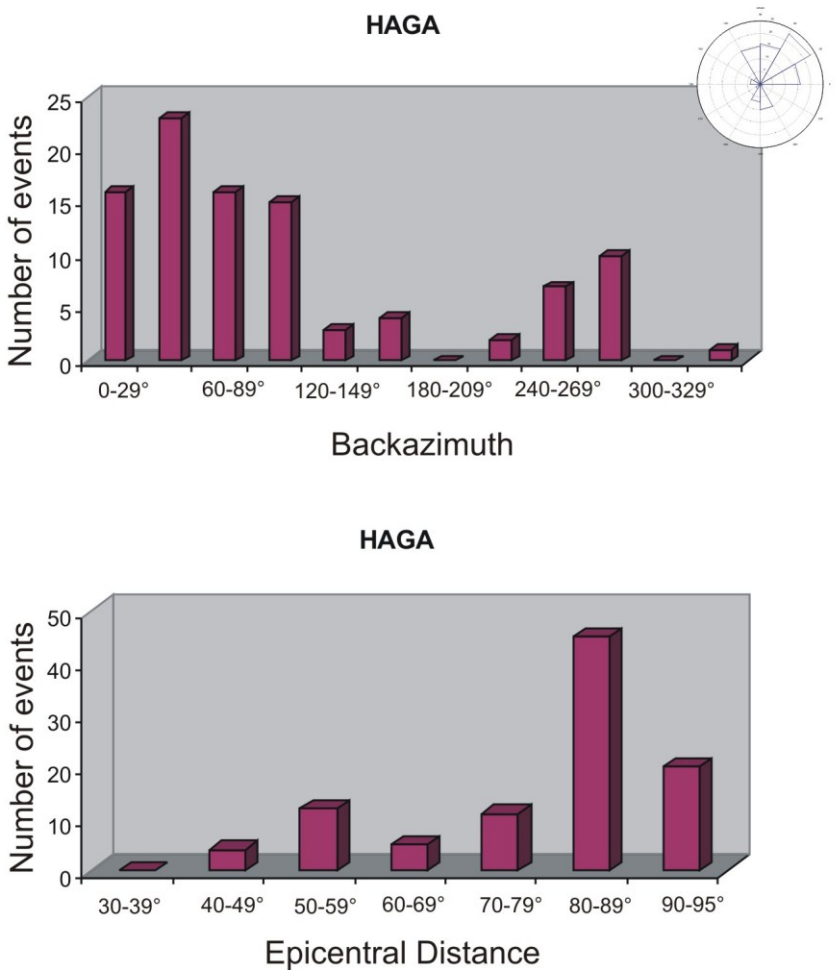

Fig. 36- *Distribution of events according to their (a) backazimuth, (b) epicentral distance with respect to HAGA station.*

The stack (**Fig. 37**) is characterized by a relatively high amplitude first arriving P-wave, followed by a relatively low amplitude peak at approximately 2.5 s and a higher amplitude phase at 3.7 s.

By considering the radial and tangential component traces we observe:

• A really strong P (at T=0.0 s) direct pulse with a time shift of ~0.4 s, between 240 and 290 degrees backazimuth (as observed at SSY station). Delay of the pulse (from zero time) indicates low velocities in the near-surface layer beneath the station. This delay results from the superposition of the direct P wave and P-to-S converted (P_S) waves generated at the basement-sediment interface.

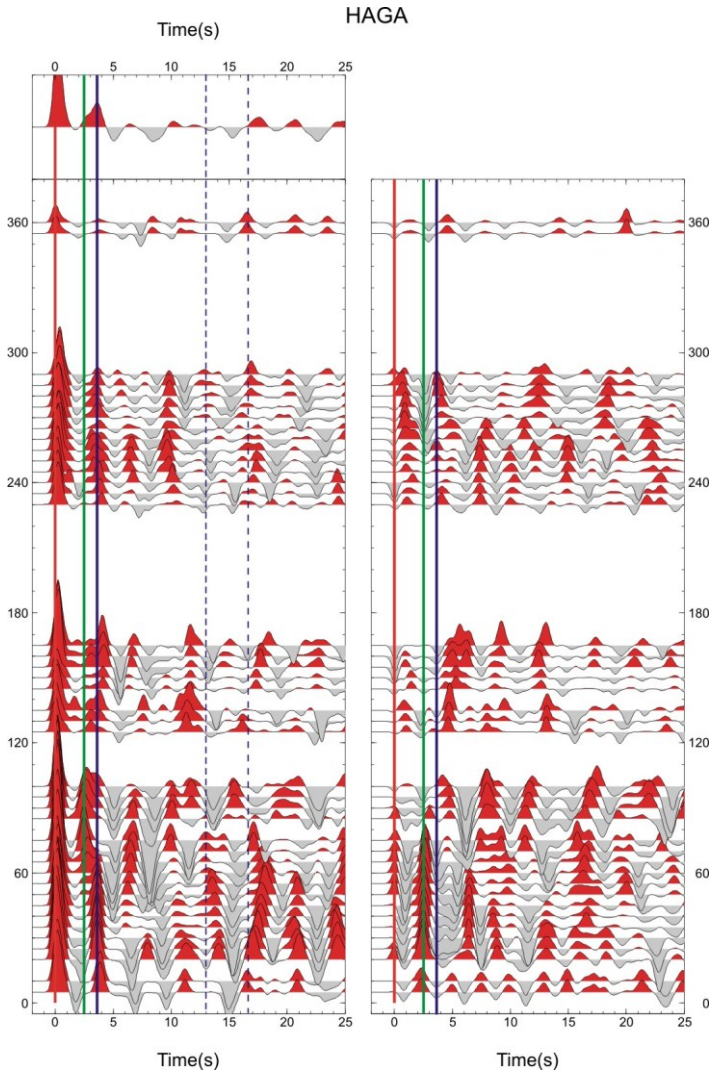

Fig. 37- *Binned RF dataset for Radial (left) and Transverse (right) components plotted as a function of the time (s) and the BAZ (°) at HAGA station. The direct P-wave arrival time is taken as the origin time. Red and gray areas indicate negative and positive pulses, respectively. Upper panel displays the average RF. Blue line marks the pulse related to the crust-mantle transition (see text for details).*

• A first positive peak at 2.5 s. This phase is seen for some but not all of the backazimuths (missing in the backazimuth range of 0-50° and 240°-360°) on the radial RFs, suggesting lateral variation of the crustal structure beneath the station.

- Then, we observe a clear and coherent positive pulse at 3.7 s behind the direct arrival (**Fig. 37**). It can be interpreted as the P_S phase (**Fig. 38**) resulting from the Moho discontinuity beneath the station. If we assume an average P-wave crustal velocity of between 5.7 and 6.2 km/s, and a V_P/V_S ratio of 1.73, then the crustal thickness generating the 3.7 s pulse is ~28-30 km (**Table 3**). The first and second Moho multiples (P_PP_S=1M=positive multiple at ca. 13.0 s and $P_SP_S+P_PS_S$=2M=negative multiple at ca. 17.0 s) are not clear (dashed blue lines in **Fig. 37**), since strong velocity jumps in the uppermost crustal layers might hide the deeper Moho conversion and multiple reflections. This phase has a relatively constant arrival time for most azimuths, although it appears to arrive slightly latest, at ~4.1 s, for backazimuths between 120° and 170° and earliest for backazimuth 250-260°. Such changes in the time of the radial P_S with backazimuth may indicate the presence of dipping structure (e.g. Cassidy, 1992; Levin and Park, 1997).

In the tangential component traces (**Fig. 37**), considerable energy indicating a degree of structural complexity is visible. In particular, we can observe:

- Some transverse energy is present at T=0.0 s. The polarity of this pulse appears to change from positive to negative between 100 and 280°. The direct P arrival appears in a two-lobed pattern, an effect produced by the dipping interface, as indicated by the fact that its polarity remains unchanged after a 90°.

- The positive pulse at about 2.5 s shows a two lobed disposition with polarity change occurring at N100° and N100°+180°=N280°. The transverse amplitude is generally zero for arrivals from the updip or downdip directions and largest for arrivals travelling along the strike direction of the interface (100°+90°=190° or 10° in this example). In particular, if we assume an average P-wave crustal velocity of 3.4 km/s, and a V_P/V_S ratio of 1.73, the phase at 2.5 s could be the first multiple of a shallow interface located at a depth of ~3.2 km (if H=3.2 km and V_P=3.4 km/s: P_S=0.69 s, 1M=2.54 s, 2M=3.23 s).

- The phase at 3.7 s shows an amplitude on the T component not null. Since the uneven coverage in the backazimuth could hide the backazimuth angle where the direction of the polarity change, strike is constrained to be 0° (eastwards dipping) by the minimum delay phase around 250-260°.

To check if those phases are the converted and/or the multiple, in **Fig. 38** we plot stacked receiver functions sorted by the ray parameter. As we can observe, the selected converted phase (3.7 s) follows a positive moveout with increasing ray parameter, while

the pulse at 2.5 s presents a negative moveout. In particular the amplitude of the P_S increases with the ray parameter (and also the arrival time), while the multiple shows constant amplitude and decreases in time arrival (Cassidy, 1992).

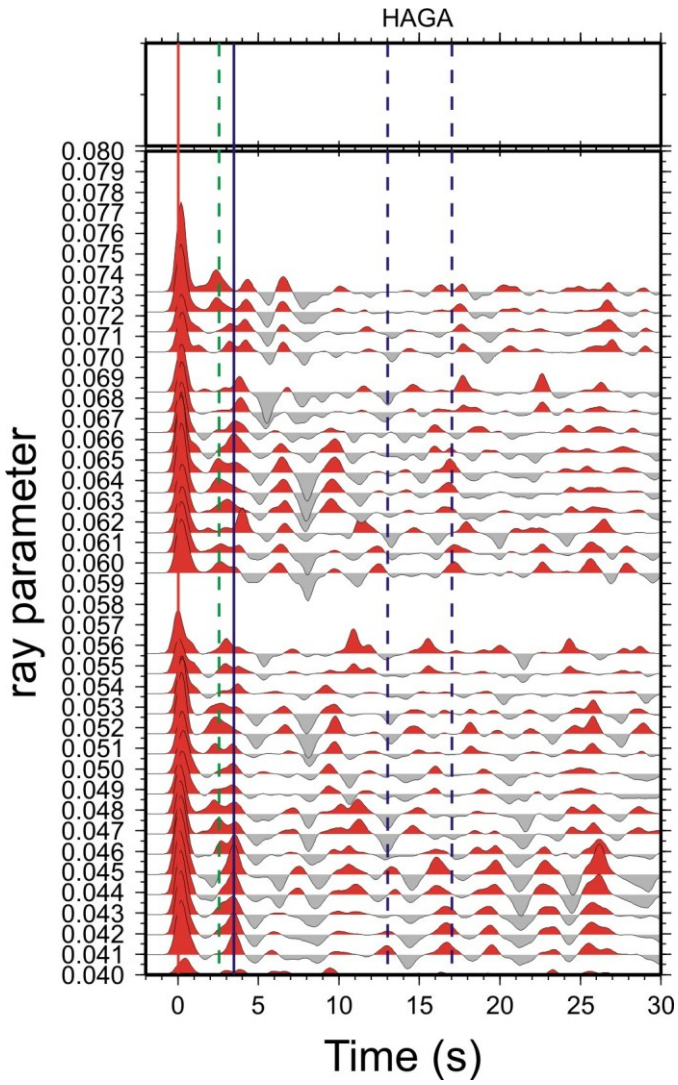

Fig. 38- *Radial receiver functions sorted by the ray parameter, computed at HAGA station. Blue line marks the pulse related to the crust-mantle transition (see text for details).*

Then, we applied the receiver function stacking technique developed by Zhu and Kanamori (2000), involving a grid search in the H and V_P/V_S space (**Fig. 39**). We used steps of 0.1 km and 0.01, respectively, searching for the maximum-stacked amplitude in the Moho depth (H) versus V_P/V_S domain in the interval of 22 to 44 km depth and 1.6 to 1.9 for the V_P/V_S ratio. Primary phase and the two multiple conversions were weighted with the values of 0.8, 0.1 and 0.1, respectively. The yellow shaded area displays the stacking function (**Fig. 39**), from blue (lower) to yellow (higher) values. For this station, the grid search maxima are poorly constrained and indicate implausible values due to a

lack of clear multiples or weak Moho conversions or superposition of unrelated phases. In this case, information on the crustal thickness and V_P/V_S ratio can arise from nearby stations or other sources.

To decipher the crustal parameters, we performed forward modelling (**Fig. 40**) for a number of simple crustal models (published and averaged velocities for the crust and upper mantle have been used) by using the approach of Frederiksen and Bostock (2000).

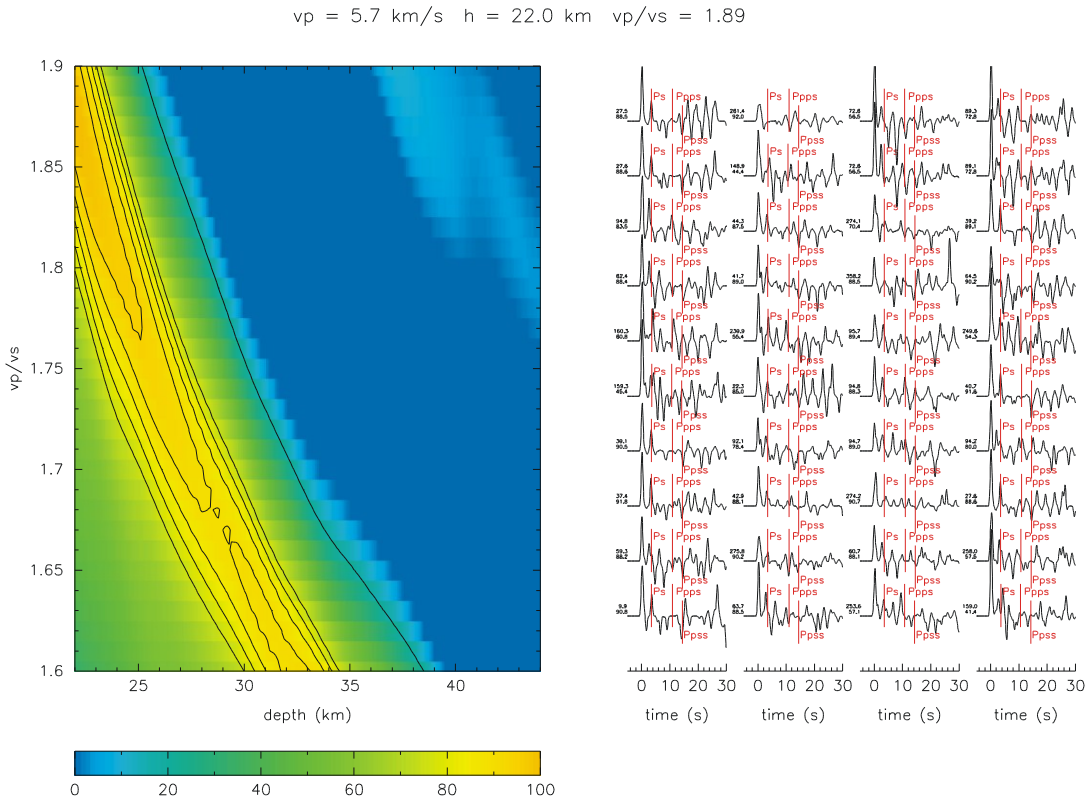

Fig. 39- *Grid search results for HAGA station according to Zhu and Kanamori (2000) method. A fixed crustal V_P value of 5.7 km/s was assumed.*

For this station, the shallower layer is modelled at 3.3 km depth and the Moho is modelled at 29.3 km depth, dipping 10° eastwards (strike N0°). Subtracting the station elevation (126 m) from the crustal thickness, the Moho is modelled at 29.2 km.

The results can be summarized into the following main points: (1) The stacking of the 97 receiver functions for station HAGA is poorly constrained. (2) The RFs for this station are generally consistent with a Moho interfaces at ~28-30 km. (3) The receiver function profile shows a converted phase at 3.7 s following the direct P arrival which has the expected increase of amplitude and time delay with ray parameter for a primary

converted phase. (4) The synthetic models (**Fig. 40**), based on the simple-layered structure including dipping layers, reproduce the main characteristics of the real data (**Fig. 37**). It should be pointed out, however, that no estimate from previous work is available for HAGA. The value calculated here, 29.2 km, therefore cannot be tested against previous work.

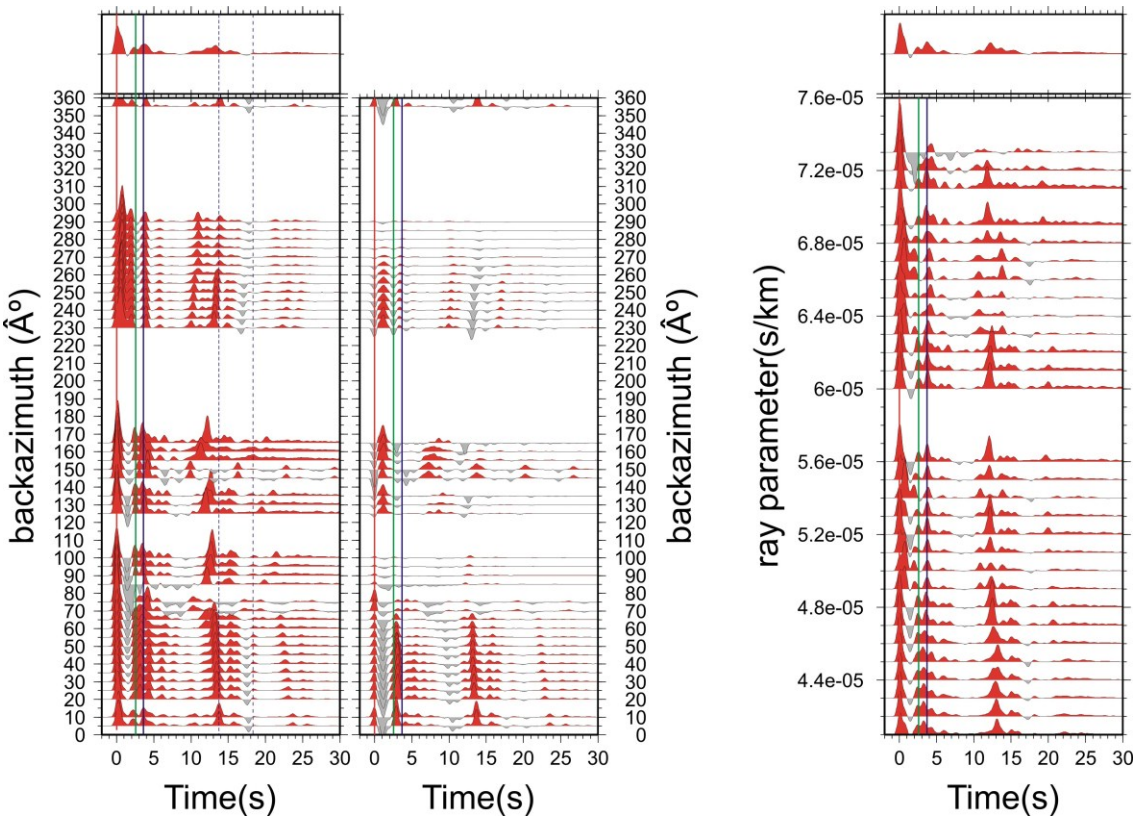

Fig. 40- *Synthetic radial and transverse RF components vs. backazimuth (on the left), computed at HAGA station by using the approach of Frederiksen and Bostock (2000). Synthetic radial RF components vs. ray parameter (on the right).*

4.2.1.4 HVZN

Station HVZN is located in the north-western part of the Hyblean Foreland on volcanic rocks, at about 32 km and 41 km eastwards from SSY and HAGA stations, respectively. This station displays an almost complete backazimuthal coverage and high data quality. Nevertheless, lack of data between 100 and 120, 160 and 220, 290 and350 degrees backazimuth are observed (**Fig. 41**).

HVZN traces appear more complex and the energy in the T component higher than in the case of SSY, HCRL and HAGA stations, indicating great intracrustal complexity (i.e. dipping intracrustal and Moho discontinuities, scattering and/or anisotropy). The

stack, comprising of 79 traces, is characterized by a relatively high amplitude first arriving P-wave, followed by a relatively low amplitude wave arrival at approximately 3.0 s and a higher amplitude phase at 4.8 s (**Fig. 42**).

By considering the radial and tangential component traces we observe:

- Radial RFs are very complex in the first 1.0 s, with a large amplitude pulse 0.5-1.0 s after the direct P arrival in the restricted backazimuth range of 0°-100° (as observed at HCRL station). We interpret this large pulse to represent a P_S converted pulse from the bottom of a thick deposit of low-velocity sediments. Where the sedimentary layer is thinner, interference of the P_S conversion and the direct P arrival produce a composite peak which is shifted in time from 0 s. Reverberations inside the sedimentary layers contribute to the pulse complexity over 1-3 s.

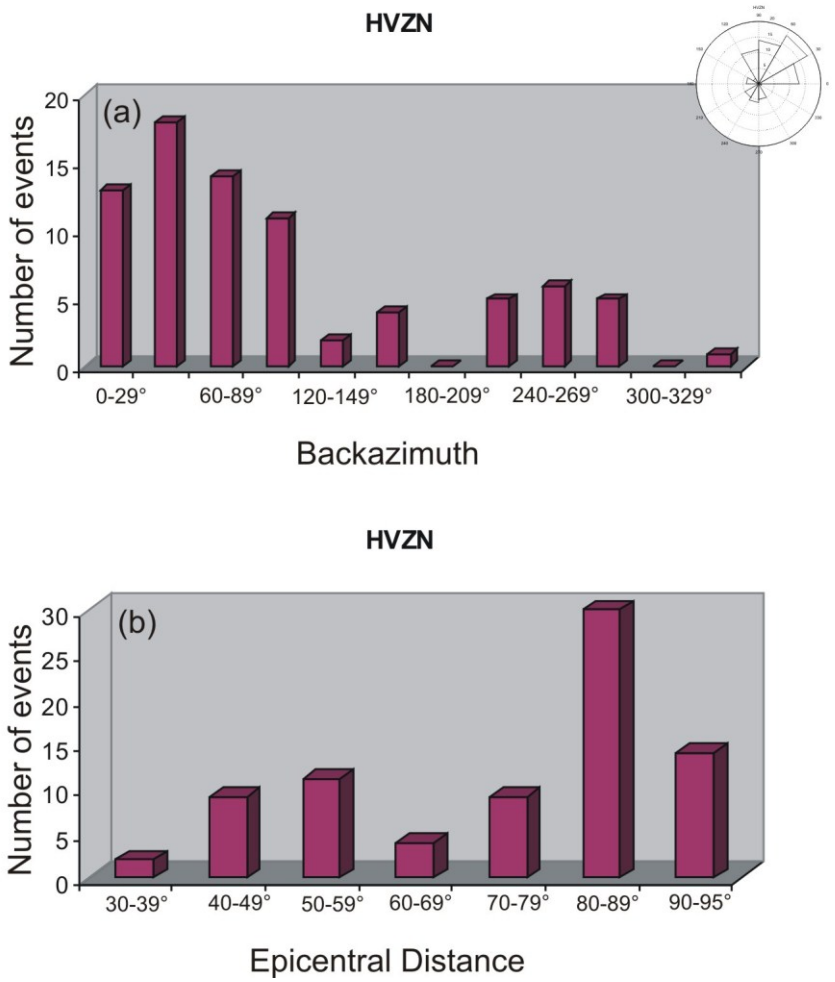

Fig. 41- *Distribution of events according to their (a) backazimuth, (b) epicentral distance with respect to HVZN station.*

- A first positive pulse at about 3.0 s. The phase, mostly clear in the backazimuth range of 230°-300°, can be related to a shallow discontinuity. The phase appears slightly

later (~0.2 s) for backazimuths from 40°-60°, and earliest (~0.5 s) at backazimuths of 140°-180°.

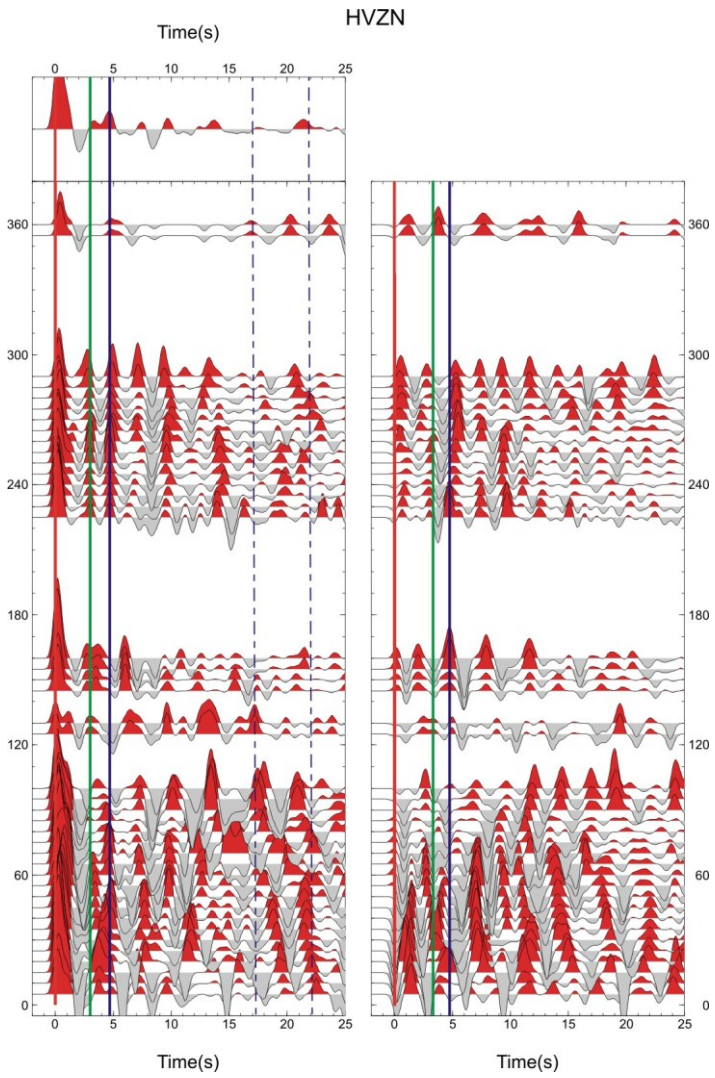

Fig. 42- *Binned RF dataset for Radial (left) and Transverse (right) components plotted as a function of the time (s) and the BAZ (°) at HVZN station. The direct P-wave arrival time is taken as the origin time. Red and gray areas indicate negative and positive pulses, respectively. Upper panel displays the average RF. Blue line marks the pulse related to the crust-mantle transition (see text for details).*

- The Moho conversion (roughly at 4.8 s) can be identified as the largest pulse after the P onset in the R receiver function (**Fig. 42**). The Moho conversion phase, indicates that the Moho is deeper than beneath other stations, or alternatively that the average crustal velocity beneath the station is slower. We used the time delay between the direct P wave and the P_S wave converted at the Moho discontinuity to infer the crustal thickness beneath the station. If we assume an average P-wave crustal velocity of between 5.7 and 6.2 km/s, and a V_P/V_S ratio of 1.73, then the depth of the discontinuity

generating the 4.8 s pulse is ~36-39 km (**Table 3**). The first and second Moho multiples (P_PP_S=1M=positive multiple at ca. 17.0 s and $P_SP_S+P_PS_S$=2M=negative multiple at ca. 22.0 s) are not clear (dashed blue lines in **Fig. 42**), since strong velocity jumps in the uppermost crustal layers might hide the deeper Moho conversion and multiple reflections.

- Some transverse energy is present at T=0.0 s. The polarity of this pulse appears to change from negative to positive between 50 and 230°. The direct P arrival appears in a two-lobed pattern, an effect produced by the dipping interface, as indicated by the fact that its polarity remains unchanged after 90°.

- The positive pulse at about 3 s shows a two lobed disposition with polarity change occurring at N40° and N40+180=N220° (strike 40+90=130° or 310°, in this example). In particular, if we assume an average P-wave crustal velocity of 3.4 km/s, and a V_P/V_S ratio of 1.73, the phase at 3 s could be the first multiple of a shallow interface located at a depth of 4.0 km (if H=4.0 km and V_P=3.4 km/s: Ps=0.86 s, 1M=3.17 s, 2M=4.04 s).

- The phase at 4.8 s shows an amplitude on the T component not null. We considered a polarity that reverses at roughly 100° and 280°. Strike is constrained to be 190° (westwards dipping) by the minimum delay phase around 100°.

The stacked receiver functions sorted by the ray parameter (**Fig. 43**) shows a positive moveout with increasing ray parameter at 4.8 (and also at 1.0 s) and a negative moveout at 3.0 s. In particular the amplitude of the P_S increases with the ray parameter (and also the arrival time), while the multiple decreases in amplitude and time arrival.

Then, we applied the receiver function stacking technique developed by Zhu and Kanamori (2000). We searched for the maximum-stacked amplitude in the Moho depth (H) versus V_P/V_S domain in the interval of 26 to 46 km depth and 1.6 to 1.9 for the V_P/V_S ratio (**Fig. 44**). Primary phase and the two multiple conversions were weighted with the values of 0.6, 0.3 and 0.1, respectively. The stacking surfaces (normalized to 100%) is shown in **Fig. 44** along with the 1σ confidence ellipses (red) from the bootstrap analysis. This station yields a V_P/V_S of 1.71 ±0.10 and thickness of 35.5±4.8 km. The correlation coefficients (the covariance matrix cross term) in **Fig. 44** exhibits a large and negative value (-90.6 %), which implies that the estimated values for V_P/V_S and H do not vary independently within the uncertainty limits.

Forward modelling (**Fig. 45**) for calculation of synthetic receiver function was achieved using the approach of Frederiksen and Bostock (2000). After multiple trials the following result has been achieved: • The shallow layer is modelled at 4.2 km depth and

shows northwest striking (N130°), 10° southwest dipping interface. • The Moho is modelled at 35.2 km depth and dips 15° west (strike N190°). Subtracting the station elevation (788 m) from the crustal thickness, the Moho is modelled at 34.4 km.

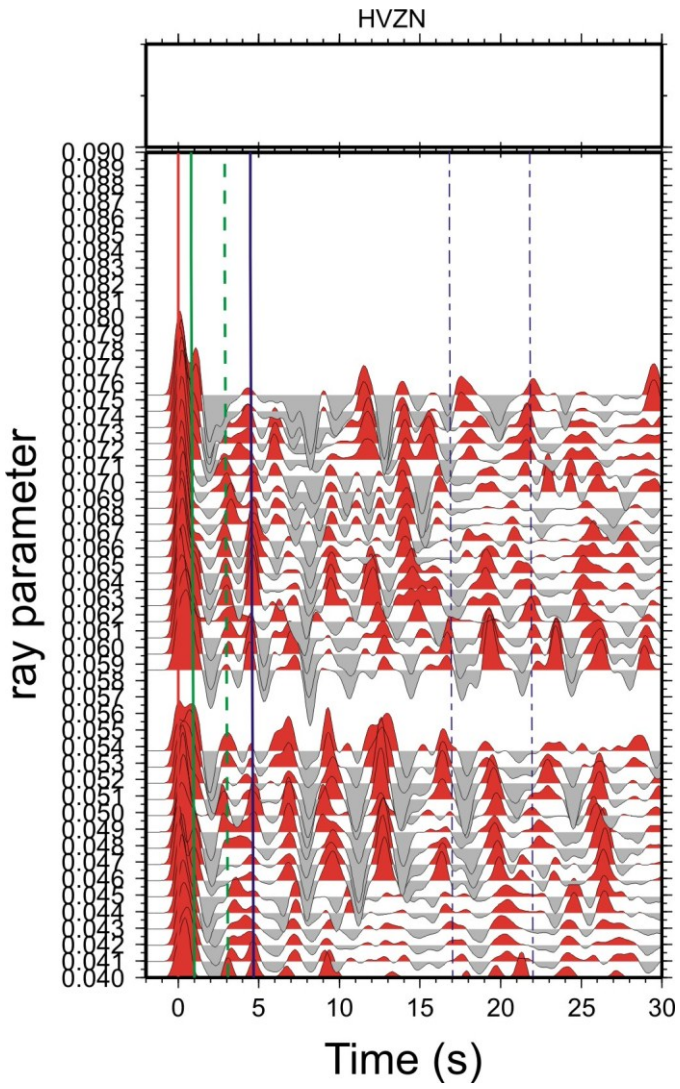

Fig. 43- *Radial receiver functions sorted by the ray parameter, computed at HVZN station. Blue line marks the pulse related to the crust-mantle transition (see text for details).*

The results can be summarized into the following main points: (1) The stacking of the 79 receiver functions for station HVZN gives a crustal thickness of 35.5 ±4.8 km with a crustal V_P/V_S ratio of 1.71 ±0.10. (2) The predicted Moho P_S arrival time agrees with the receiver function profile which shows a strong converted phase at 4.8 s following the direct P arrival (as stated above for an average P-wave crustal velocity of between 5.7 and 6.2 km/s, the depth of the discontinuity generating the 4.8 s pulse is ~36-39 km). (3) This phase has the expected increase of amplitude and time delay with

ray parameter for a primary converted phase. (4) We find that the synthetic model (**Fig. 45**) based on the simple-layered structure including dipping layers reproduce the main characteristics of the real data (**Fig. 42**). (5) Moreover, a good correlation between previous studies, stacked values and synthetically modelled estimates, is observed. The inferred crustal thickness of 34.4 is comparable to the value of 33.5±9.3 km interpreted from Piana Agostinetti and Amato (2009), just beneath this station.

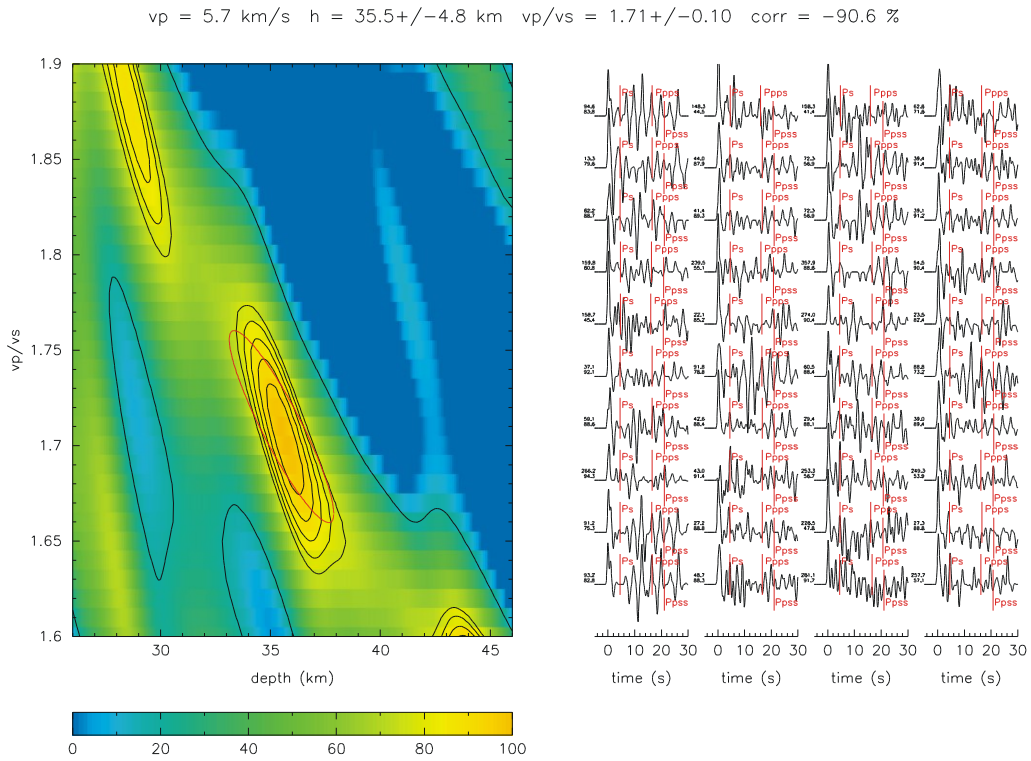

Fig. 44- *Grid search results for HVZN station according to Zhu and Kanamori (2000) method. A fixed crustal V_P value of 5.7 km/s was assumed.*

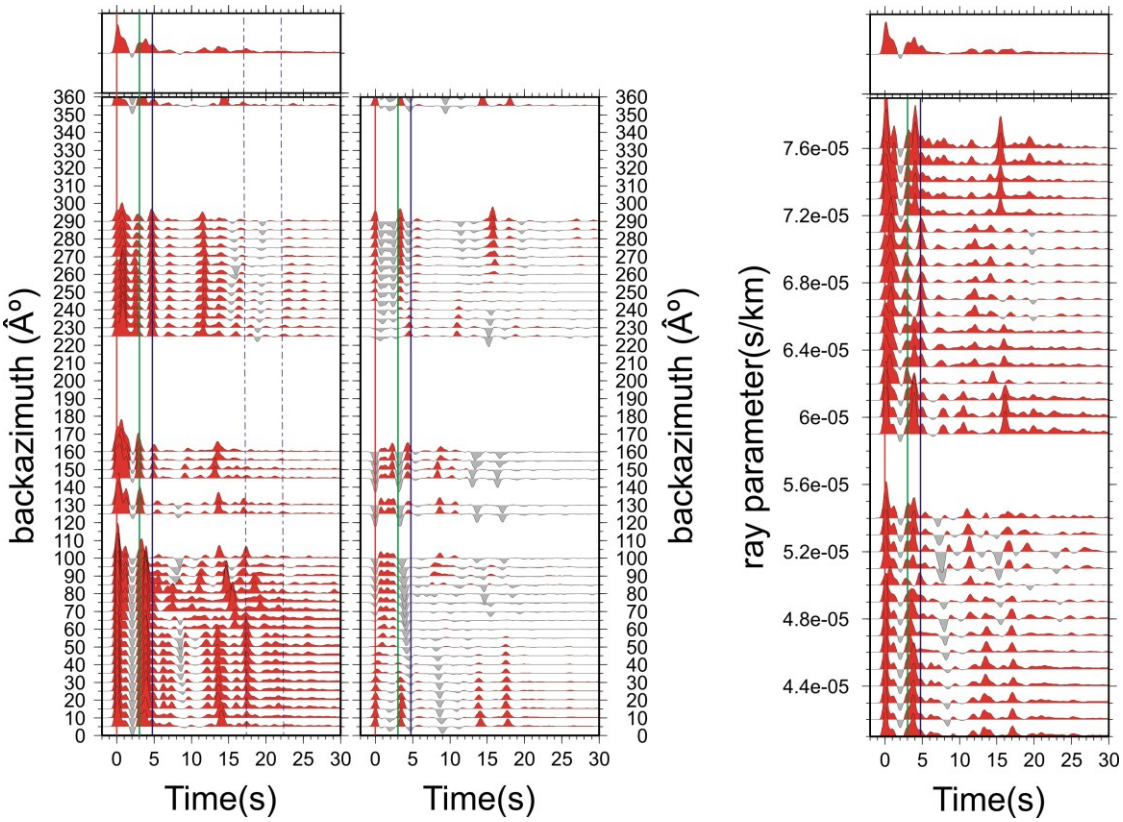

Fig. 45- *Synthetic radial and transverse RF components vs. backazimuth (on the left), computed at HVZN station by using the approach of Frederiksen and Bostock (2000). Synthetic radial RF components vs. ray parameter (on the right).*

4.2.1.5 HMDC

Station HMDC is located on the south-western side of the Hyblean Foreland, about 35 km from SSY and 25 km from HVZN stations, on an alternation of marls and calcarenitic limestones (**Fig. 22**). Data from HMDC station, some of the best in this study, include 39 events with appropriate backazimuth and distance range (**Fig. 46**); lack of data between 100 and 140, 170 and 240, 280 and350 degrees backazimuth are observed. This station shows a stacked P receiver function (**Fig. 47**) with a relatively high amplitude first arriving P-wave, followed by a large phase at approximately 1.8 s and a relatively lower amplitude wave arrival at 5.1 s. A negative pulse with large amplitude is observed 3 s after the initial pulse.

By considering the radial and tangential component traces we observe:

- A high amplitude first arriving P-wave, slightly later (~0.4 s) for backazimuths from 80°-170°. The amplitude pattern of this phase with backazimuth can be reproduced by a dipping interface with a strong velocity contrast, which is too shallow to generate a P_S pulse separated from the direct-P pulse.

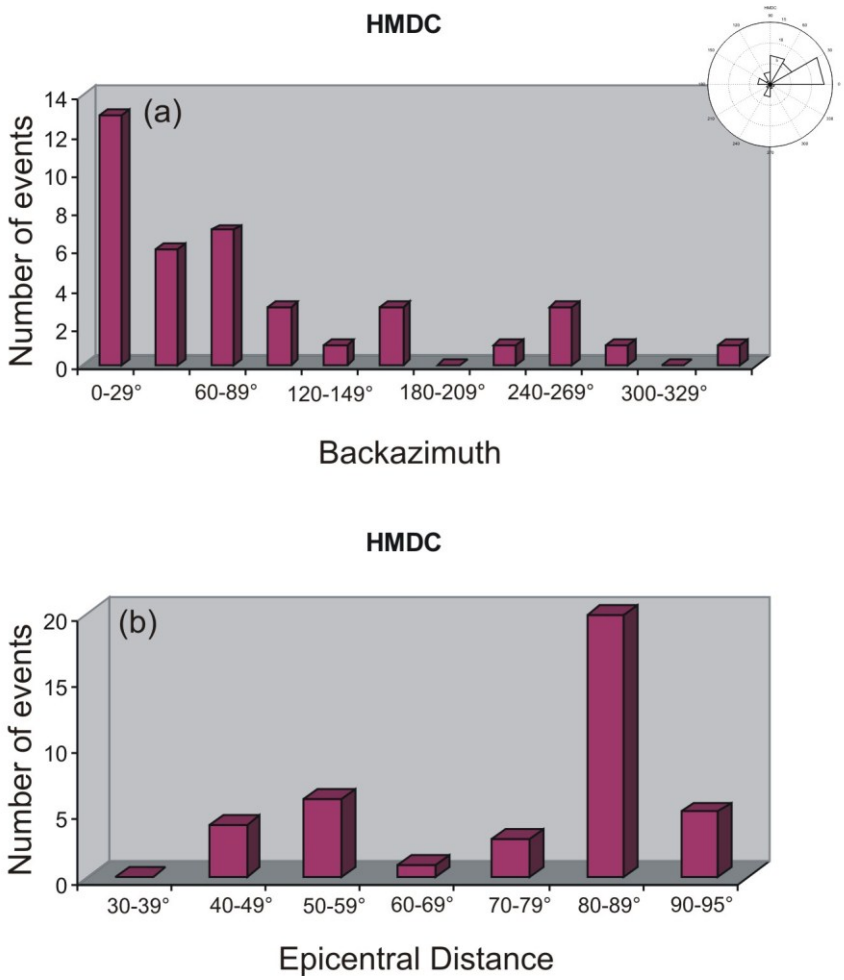

Fig. 46- *Distribution of events according to their (a) backazimuth, (b) epicentral distance with respect to HMDC station.*

• A first positive pulse at 1.8 s (slightly earlier than the similar pulse seen on the SSY radial RFs), the largest pulse after the P onset. This phase, related to a shallow discontinuity, is observable in the all available backazimuth, but with an amplitude that decreases with the backazimuth. As for SSY, we can interpret this early pulse to represent a conversion from a mid-crustal discontinuity.

• Then, the positive, low amplitude phase at about 5.1 s can be related to the P_S Moho conversion. The Moho conversion phase (at 5.1 s), indicates that the Moho is deeper than beneath other stations, or alternatively that the average crustal velocity beneath the station is slower. This phase appears slightly later (~0.2 s) for backazimuths from 10°-30°, and earliest (~0.5 s) for backazimuths of 240°-280°. Its low amplitude can be due to a weak velocity contrast and/or to a deterioration caused by crustal multiples. Firstly, we used the time delay between the direct P wave and the P_S wave converted at the crust-mantle boundary to infer crustal thickness beneath the station, given a bulk crustal velocity. If we translate into depth the arrival time of the converted

phase using an average V_P/V_S ratio of 1.73 and an average P-wave crustal velocity of between 5.7 and 6.2 km/s, its crustal thickness is is ~39-42 km (**Table 3**). The first and second Moho multiples (P_PP_S=1M=positive multiple at ca. 18.0 s and $P_SP_S+P_PS_S$=2M=negative multiple at ca. 23.0 s) are not clear (dashed blue lines in **Fig. 47**) since strong velocity jumps in the uppermost crustal layers might hide the deeper Moho conversion and multiple reflections.

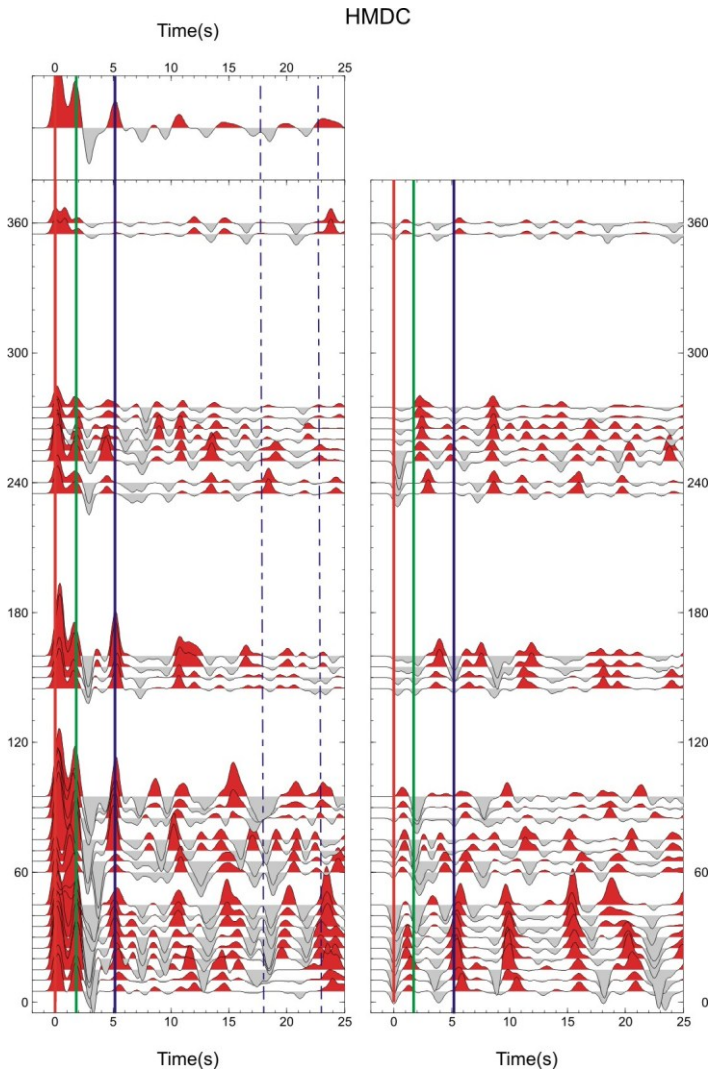

Fig. 47- *Binned RF dataset for Radial (left) and Transverse (right) components plotted as a function of the time (s) and the BAZ (°) at HMDC station. The direct P-wave arrival time is taken as the origin time. Red and gray areas indicate negative and positive pulses, respectively. Upper panel displays the average RF. Blue line marks the pulse related to the crust-mantle transition (see text for details).*

Looking at the tangential component traces (**Fig. 47**), considerable energy is visible. In particular:

- The phase at 1.8 s shows an amplitude on the T component not null and varies with

the backazimuth angle (polarity change occurs at N20° and N20+180=N200°). Strike direction of the interface is 20+90=110° or 290°, in this example. This pulse could be the first multiple of a shallow interface (if H=2.3 km and V_P =3.4 km/s: P_S=0.49 s, P_PP_S=1M=1.82 s, P_SP_S+P_PS_S=2M=2.32 s). However, from geological sections we know the existence of the carbonate rocks at about 8-10 km depth. In this case, if we assume an average P-wave crustal velocity of 4.7 km/s (an average value up to 10 km) and a V_P/V_S ratio of 1.73, the phase at 1.8 s could be the P_S of a shallow interface located at a depth of ~11.5 km (if H=11.5 km and V_P =4.7 km/s: P_S=1.82 s, P_PP_S=1M=6.54 s, P_SP_S+P_PS_S=2M=8.37 s).

- The phase at 5.1 s shows an amplitude on the T component not null. We considered a polarity that reverses at 60° and 240°. The strike of this interface is constrained by the minimum time-delay of this phase at about 240° backazimuth to be roughly 330°, while determining its dip is more tricky.

The stacked receiver functions sorted by the ray parameter shows a positive moveout with increasing ray parameter at 5.1, while no moveout is observed at 1.8 s (**Fig. 48)**. In particular the amplitude of the P_S increases with the ray parameter (and also the arrival time), while the multiple should be decreasing in amplitude and time arrival (Cassidy, 1992).

Then, we slant stacked the 9 receiver functions (**Fig. 49**) in order to find the bulk crustal thickness and crustal V_P/V_S (Zhu and Kanamori, 2000). We searched for the maximum-stacked amplitude in the Moho depth (H) versus V_P/V_S domain in the interval of 32 to 52 km depth and 1.6 to 1.9 for the V_P/V_S ratio (**Fig. 49**). Primary phase and the two multiple conversions were weighted with the values of 0.6, 0.3 and 0.1, respectively. We base the statistics on 200 bootstrap replications which means we repeat the stacking procedure 200 times with a resampled data set selected randomly from the original data set.

The stacking surfaces (normalized to 100%) is shown in **Fig. 49** along with the 1σ confidence ellipses (red) from the bootstrap analysis. This station yields a V_P/V_S of 1.68 ±0.03 and thickness of 40.9 ±1.4 km. The correlation coefficient (the covariance matrix cross term) exhibits a large and negative value (-92.1 %), which implies that the estimated values for V_P/V_S and H do not vary independently within the uncertainty limits.

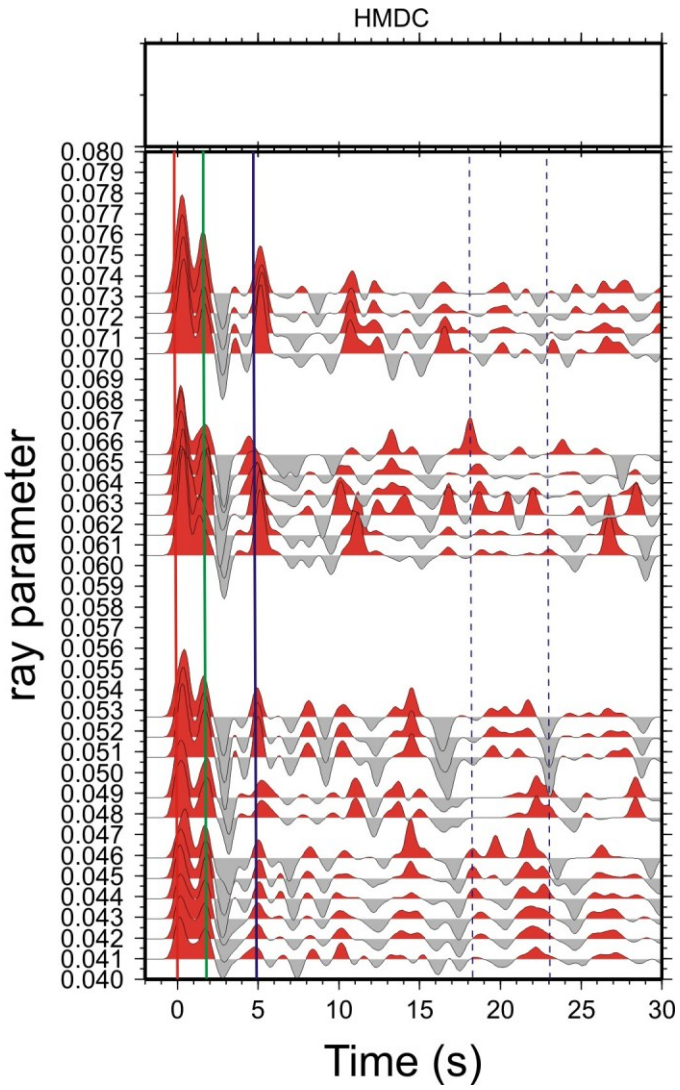

Fig. 48- *Radial receiver functions sorted by the ray parameter, computed at HMDC station. Blue line marks the pulse related to the crust-mantle transition (see text for details).*

Forward modelling (**Fig. 50**) for calculation of synthetic receiver function was achieved using the approach of Frederiksen and Bostock (2000). After multiple trials the following results have been achieved: • The shallow layer is modelled at 2.2 km depth and shows an east striking (N110°), 10° south dipping interface. • A mid-crustal discontinuity is observed at roughly 13 km depth. • The Moho is modelled at 38.5 km depth and dips 15° north-eastwards (strike N330°). Subtracting the station elevation (600 m) from the crustal thickness, the Moho is modelled roughly at 38.0 km.

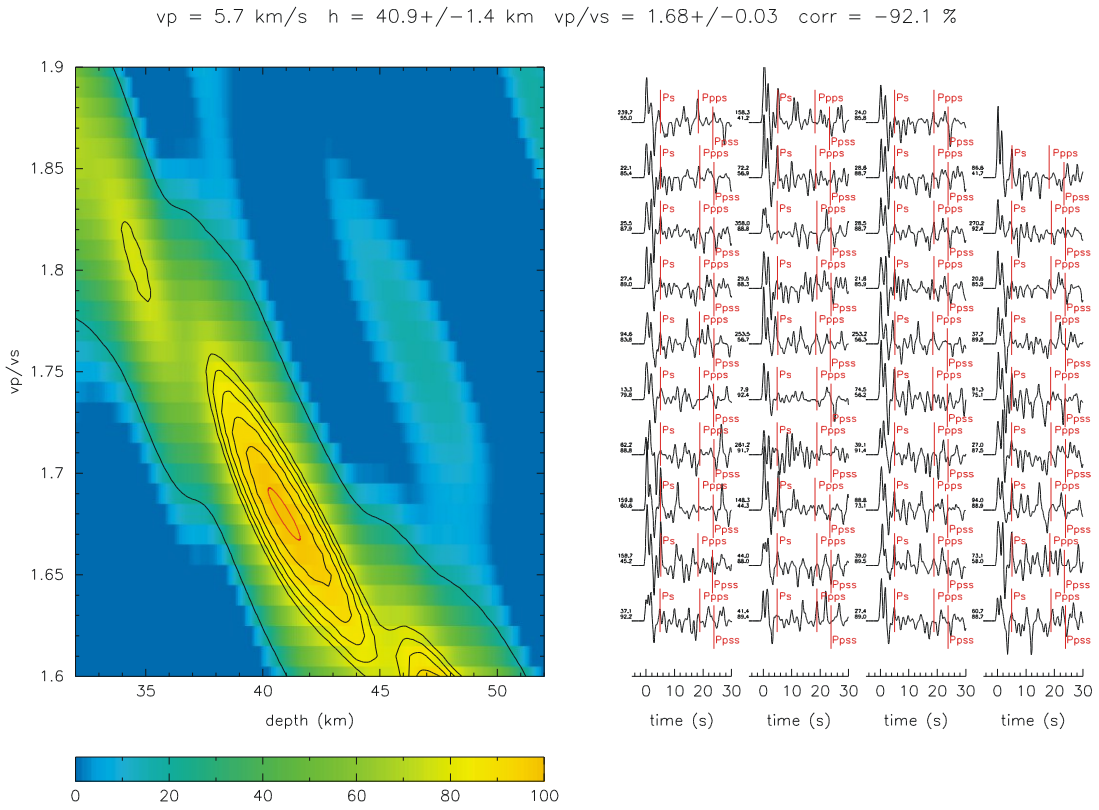

Fig. 49- *Grid search results for HMDC station according to Zhu and Kanamori (2000) method. A fixed crustal V_P value of 5.7 km/s was assumed.*

The results can be summarized into the following main points: (1) The stacking of the 39 receiver functions for station HMDC gives a crustal thickness of 40.9±1.4 km with a crustal V_P/V_S ratio of 1.68 ±0.03. (2) The predicted Moho P_S arrival time agrees with the receiver function profile which shows a strong converted phase at 5.1 s following the direct P arrival (as stated above for an average P-wave crustal velocity of between 5.7 and 6.2 km/s, the depth of the discontinuity generating the 5.1 s pulse is ~39-42 km). (3) This phase has the expected increase of amplitude and time delay with ray parameter for a primary converted phase. (4) Moreover, we find that the synthetic model (**Fig. 50**) based on the simple-layered structure including dipping layers reproduce the major characteristics of the real data (**Fig. 47**). (5) There is a good correlation between previous studies, stacked values and synthetically modelled estimates. The inferred crustal thickness of 38 km is slightly greater than the value of 34± 1.5 km found from Piana Agostinetti and Amato (2009), just beneath this station.

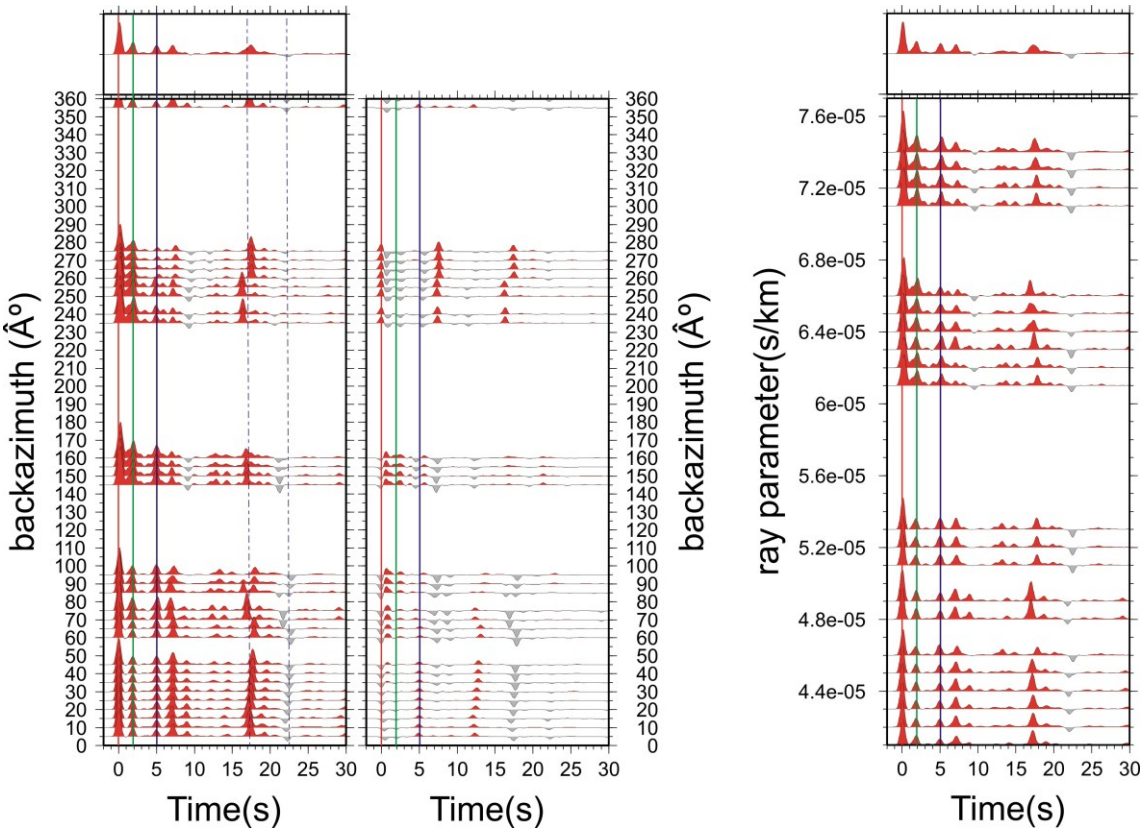

Fig. 50- *Synthetic radial and transverse RF components vs. backazimuth (on the left), computed at HMDC station by using the approach of Frederiksen and Bostock (2000). Synthetic radial RF components vs. ray parameter (on the right).*

4.2.1.6 HAVL

HAVL station, the southernmost station of the Hyblean Foreland, far about 22 km from SSY and 30 km from HMDC stations, is located on Meso-Cenozoic carbonate sediments (**Fig. 22** and **Table 1**). This station includes 46 events with appropriate backazimuth and distance range (**Fig. 51**). Backazimuth information between 100 and 150, 170 and 220, 290 and 350 degrees are nevertheless not available.

Fig. 52 shows radial and tangential components of RFs vs. backazimuth (BAZ). The stack is characterized by a relatively high amplitude first arriving P-wave, followed by a phase at approximately 1.7 s and a wave arrival at approximately 4.9 s. In particular, we can observe:

- A clear time delay and amplitude variation of the direct-P pulse on the radial component. This behaviour can be interpreted as being caused by interference between the direct-P and P_S conversions from a shallow, high-velocity contrast interface (Owens and Crosson, 1988).

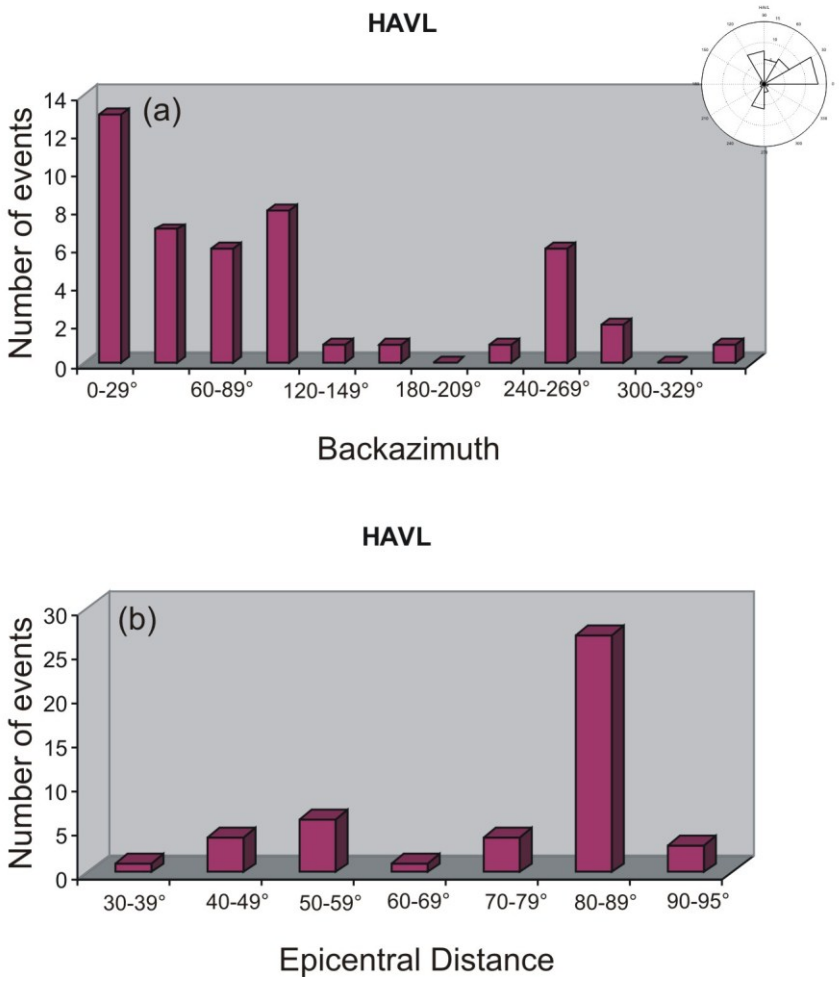

Fig. 51- *Distribution of events according to their (a) backazimuth, (b) epicentral distance with respect to HAVL station.*

• Another prominent feature in the radial RFs is a phase seen from all BAZ which arrives progressively later with increasing BAZ angle (time delay between 1.7 and 2.2 s with respect to direct P arrival; **Fig. 52**).

• Then, we observe a clear and coherent phase at 4.9 s (slightly earlier than the similar pulse seen on the HMDC radial RFs), which can be identified as the Moho conversion (**Fig. 53**). If we assume an average P-wave crustal velocity of between 5.7 and 6.2 km/s, and a V_P/V_S ratio of 1.73, then the depth of the discontinuity generating the 4.9 s pulse is ~37-40 km (**Table 3**). The first and second Moho multiples (P_PP_S=1M=positive multiple at ca. 17.0 s and $P_SP_S+P_PS_S$=2M=negative multiple at ca. 22.0 s) are not clear (dashed blue lines in **Fig. 52**) The P_S phase has a relatively constant arrival time for most azimuths, although it appears to arrive slightly latest, at ~5.1-5.2 s, for backazimuths between 140° and 170° and earliest for backazimuths of 250° and 290°. Such changes in time of the radial P_S with backazimuth may support the presence of a dipping structure (e.g. Cassidy, 1992; Levin and Park, 1997).

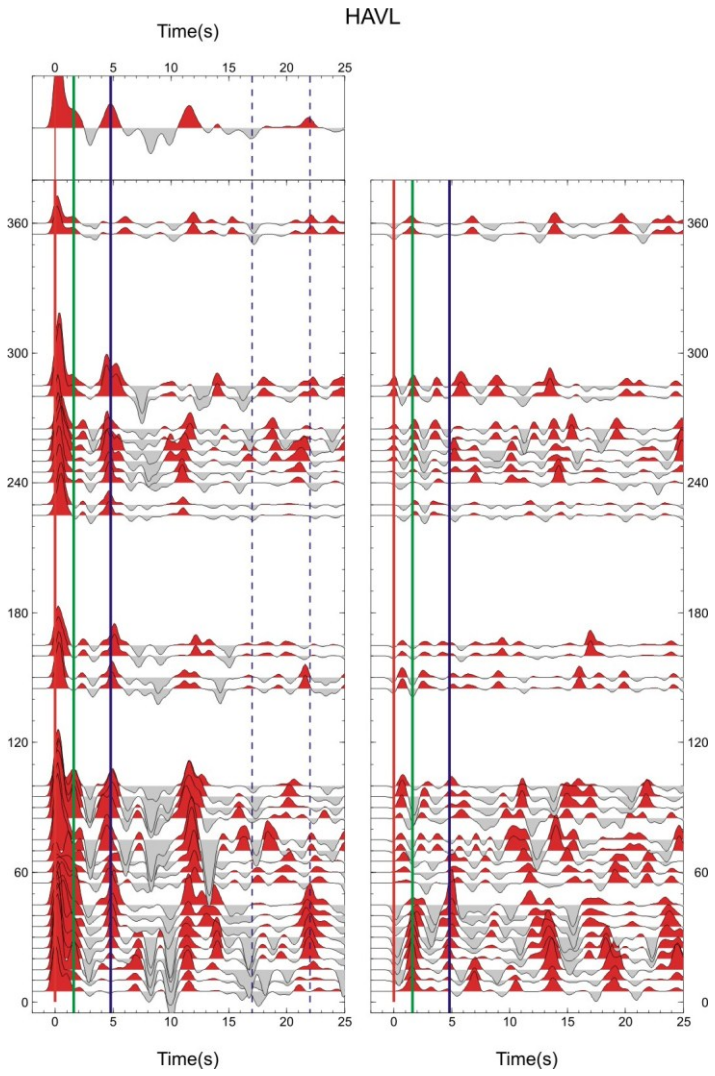

Fig. 52- *Binned RF dataset for Radial (left) and Transverse (right) components plotted as a function of the time (s) and the BAZ (°) at HAVL station. The direct P-wave arrival time is taken as the origin time. Red and gray areas indicate negative and positive pulses, respectively. Upper panel displays the average RF. Blue line marks the pulse related to the crust-mantle transition (see text for details).*

Significant energy is visible in the tangential component traces. In particular:

• The phase at 1.7 s shows an amplitude on the T component not null and varies with the backazimuth angle (polarity change occurs at N60° and N60+180=N240° in this example). The motion of the first transverse arrivals is downward between 60° and 240° BAZ, and upward between 240° and 60°. These observations could be explained with the presence of a north-eastwards dipping interface at about 2.2 km depth. This pulse could be the first multiple of a shallow interface (H=2.2 km and V_P=3.4 km/s: P_S=0.47 s, 1M=1.74 s, 2M=2.22 s) striking 60°+90°=150° or 330°. We also considered a mid-crustal discontinuity 12 km depth (if V_P=4.7 km: P_S=1.9 s, 1M=6.83 s, 2M=8.73 s) with P_S conversion arriving with the multiples from the shallow discontinuity at ~2.2 km

depth.

- The phase at 4.9 s shows an amplitude on the T component not null. We considered a polarity that reverses around at 180° and 360°. However, the choice of 180° is somewhat arbitrary, since there are few traces around 180° backazimuth.

For this station, the stacked receiver functions, sorted by the ray parameter (**Fig. 53**), shows a positive moveout with increasing ray parameter at 4.9 (and also at 0.5 s) and a constant moveout at 1.7 s. As stated above, if the amplitude of the P_S increases with the ray parameter (and also the arrival time), the amplitude of reverberations may remain constant or even decreases with the ray parameter. The pulse at 1.9 s (P_S of a subcrustal discontinuity 12 km depth) could potentially be overwhelm by the negative multiple of the shallow interface at 2.2 km.

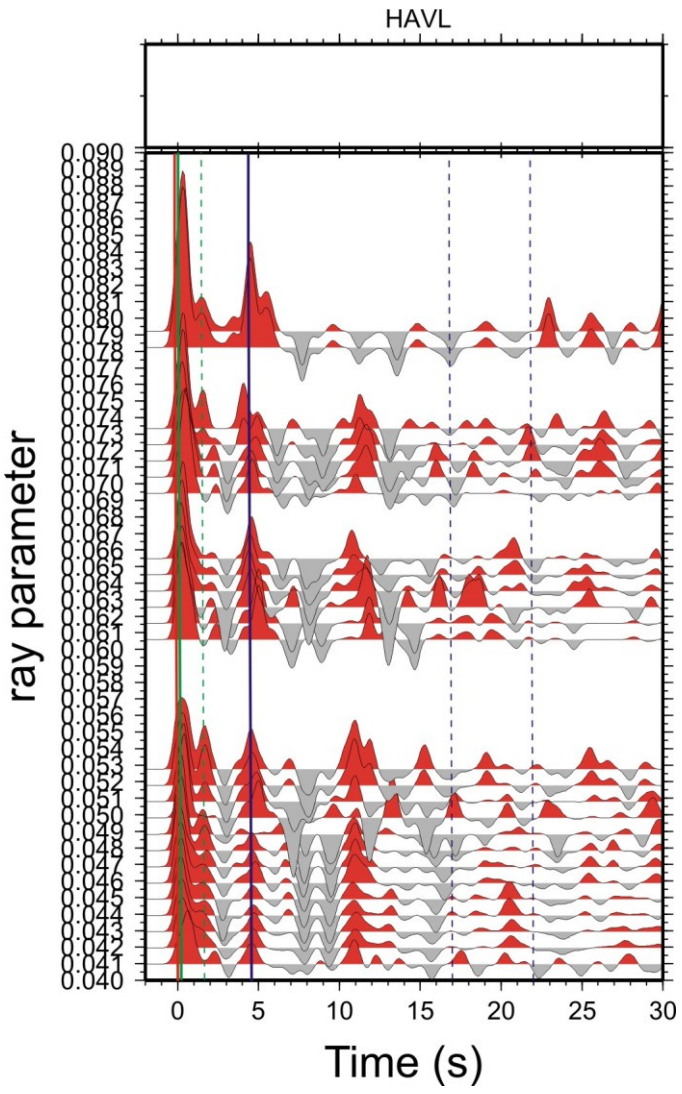

Fig. 53- *Radial receiver functions sorted by the ray parameter, computed at HAVL station. Blue line marks the pulse related to the crust-mantle transition (see text for details).*

Then, we applied the receiver function stacking technique developed by Zhu and Kanamori (2000). We searched for the maximum-stacked amplitude in the Moho depth (H) versus V_P/V_S domain in the interval of 26 to 44 km depth and 1.6 to 1.9 for the V_P/V_S ratio (**Fig. 54**). Primary phase and the two multiple conversions were weighted with the values of 0.8, 0.1 and 0.1, respectively. For this station, the receiver function stacking technique does not provide a stable solution, showing three maxima at depth (roughly 30, 36 and 42 km). Two of these peaks agree with the receiver function profile which shows a strong converted phase at 4.9 s following the direct P arrival: (a) V_P/V_S of 1.71 ±0.05 and thickness of 36.2±3.8 km; (b) V_P/V_S of 1.60 ±0.10 and thickness of 42.8±4.9 km (**Fig. 54**).

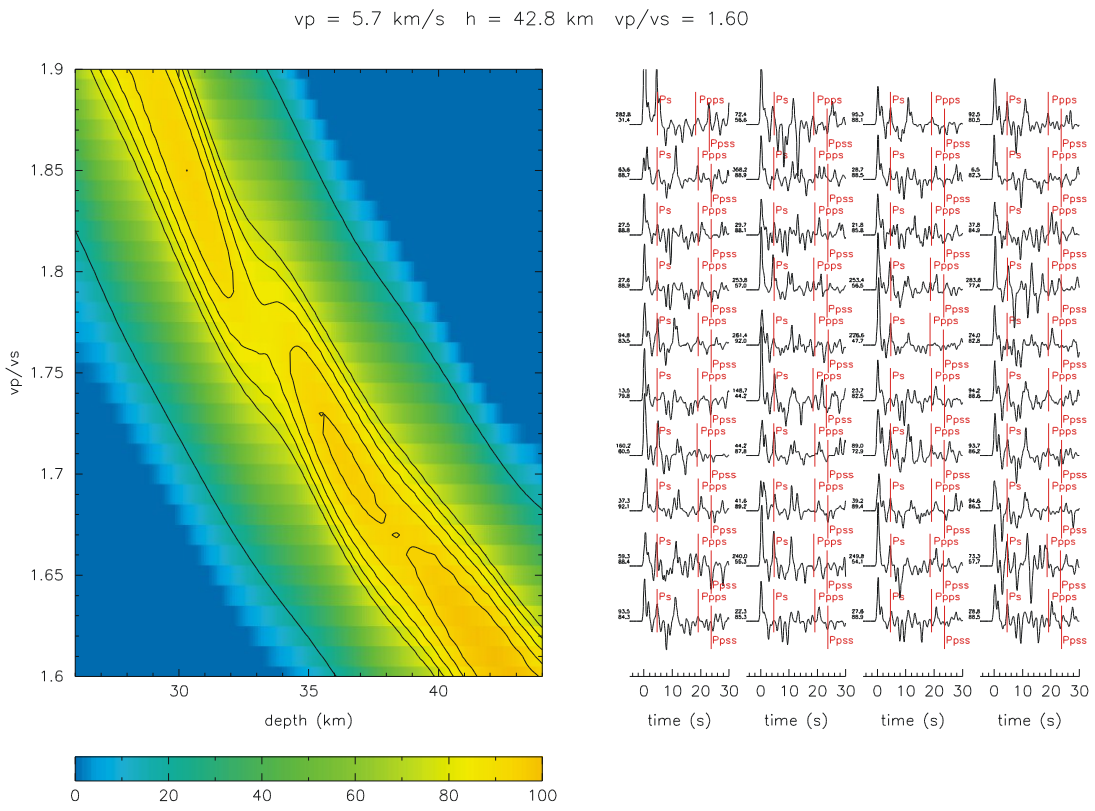

Fig. 54- *Grid search results for HAVL station according to Zhu and Kanamori (2000) method. A fixed crustal V_P value of 5.7 km/s was assumed.*

Forward modelling (**Fig. 55**) for calculation of synthetic receiver function was achieved using the approach of Frederiksen and Bostock (2000). After multiple trials the following results have been achieved: • The shallow layer is modelled at 2.2 km depth and shows a northwest striking (N330°), 10° northeast dipping interface. • The mid-crustal discontinuity is at roughly 12 km depth. • The Moho is modelled at 37.2 km

depth and dips 10° southwards (strike N90°). Subtracting the station elevation (503 m) from the crustal thickness, the Moho is modelled at 36.7 km.

The results can be summarized into the following main points: (1) The stacking of the 46 receiver functions for station HAVL does not provide a stable solution (two peaks agree with the receiver function profile: (a) V_P/V_S of 1.71 ±0.05 and thickness of 36.2±3.8 km; (b) V_P/V_S of 1.60±0.10 and thickness of 42.8±4.9 km). (2) The receiver function profile shows a strong converted phase at 4.9 s following the direct P arrival. (3) This phase has the expected increase of amplitude and time delay with ray parameter for a primary converted phase. (4) We find that the synthetic models (**Fig. 55**) based on the simple-layered structure including dipping layers reproduce the major characteristics of the real data (**Fig. 52**). (5) There is a good correlation between previous studies, stacked values and synthetically modelled estimates. The inferred crustal thickness of 36.7 km is slightly lower than the value of 41.5±11.0 km interpreted from Piana Agostinetti and Amato (2009) for the same station.

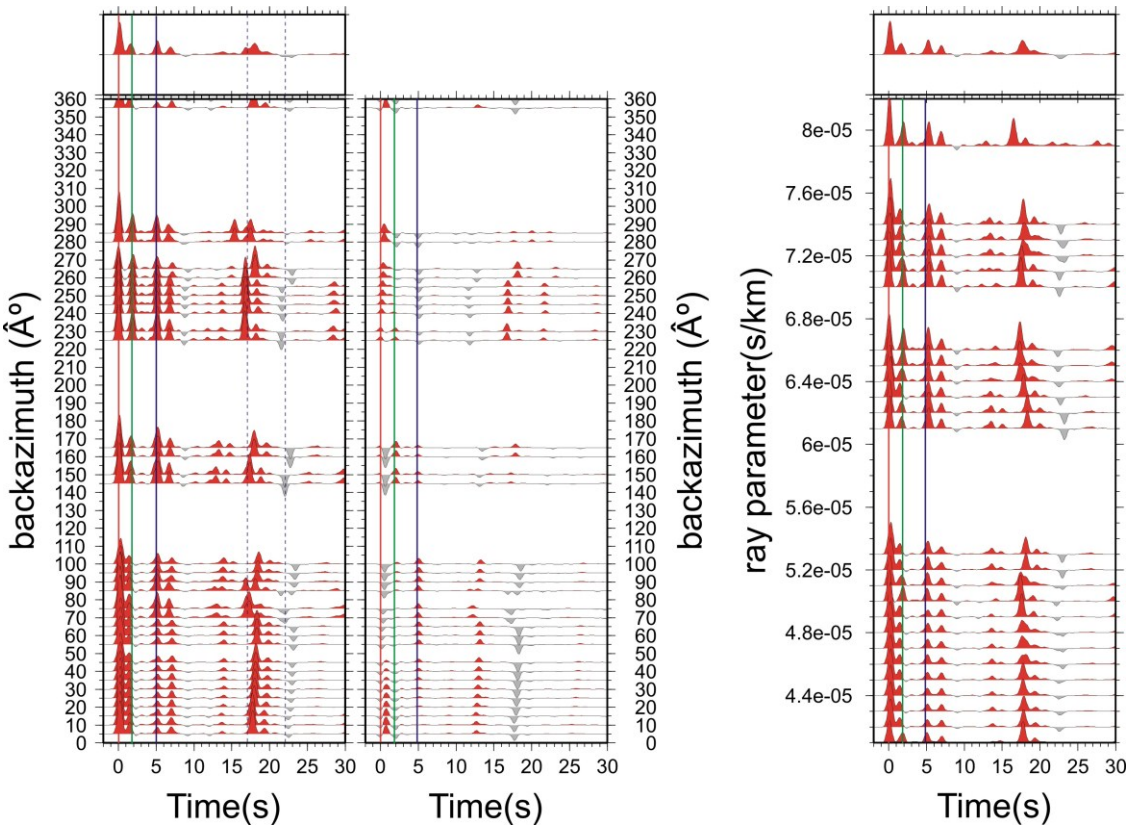

Fig. 55- *Synthetic radial and transverse RF components vs. backazimuth (on the left), computed at HAVL station by using the approach of Frederiksen and Bostock (2000). Synthetic radial RF components vs. ray parameter (on the right).*

4.2.1.7 HLNI

Station HLNI is located in the northern part of the Hyblean Foreland on Recent Quaternary deposits, far about 16 km from HCRL, 28 km from SSY and 23 km from HVZN stations, respectively (**Fig. 22**). Northwards the station is bordered by the older extensional belt, named Gela-Catania Foredeep. The quantity and quality of the waveform data derived from this station are not comparable to the data derived for the other stations, primarily because of the short duration of the recording period (since 2009; see **Table 2**). Nevertheless, a reasonable number of suitable teleseismic events (36 traces) were recorded by this station, with backazimuth information not available between 100 and 130, 160 and 250, 290 and 360 degrees (**Fig. 56**). Looking at **Fig. 57**, this station shows a stacked P receiver function with a relatively high amplitude first arriving P-wave, followed by a relatively low amplitude wave arrival at approximately 3.0 s and two relatively lower amplitude wave arrivals at approximately 4.2 and 5.5 seconds (s). The identification of the pulse corresponding to the Moho conversion is unclear as two pulses (4.2 and 5.5 s) are present within the time range of possible Moho conversions, nevertheless the pulse at 4.2 s shows a positive moveout with increasing ray parameter (**Fig. 58**), while the pulse at roughly 5.5 s decreases with increasing ray parameter. The identification of the Moho with the earlier pulse leads to a shallower Moho and to a smoother transition toward the surrounding stations (see SSY and HCRL stations), whereas the later pulse is assumed to be related to a subcrustal discontinuity.

Looking at the radial and tangential component traces we observe:

- Radial RFs (**Fig. 57**) are very complex in the first 1.0 s (as observed for HVZN and HCRL stations), with a large amplitude pulse 0.5-1.0 s after the direct P arrival in the restricted backazimuth range of 0°-100°. We interpret this large pulse to represent a P_S converted pulse from the bottom of a thick deposit of low-velocity sediments. Where the sedimentary layer is thinner, the interference of the P_S conversion and the direct P arrival produce a composite peak which is shifted in time from 0 s. Reverberations inside the sedimentary layers contribute to the pulse complexity over 1-3 s.

- Then we observe a phase at roughly 3.0 s. This phase is seen for some but not all of the backazimuths on the RFs and it can be related to a shallow discontinuity.

- Then, we observe a positive pulse at 4.2 s behind the direct arrival, which can be identified as the Moho conversion. Its low amplitude can be due to a weak velocity contrast and/or to a deterioration caused by crustal multiples arriving in the same time interval. If we translate into depth the arrival time of the converted phase using an

average V_P/V_S ratio of 1.73 and an average P-wave crustal velocity of between 5.7 and 6.2 km/s, its crustal thickness is ~32-35 km (**Table 3**). The first and second Moho multiples (P_PP_S=1M=positive multiple at ca. 15.0 s and P_SP_S+P_PS_S=2M=negative multiple at ca. 19.0 s) are not clear (dashed blue lines in **Fig. 57**), since strong velocity jumps in the uppermost crustal layers might hide the deeper Moho conversion and multiple reflections. The P_S phase has a relatively constant arrival time for most azimuths, although it is not observable in the all available backazimuths.

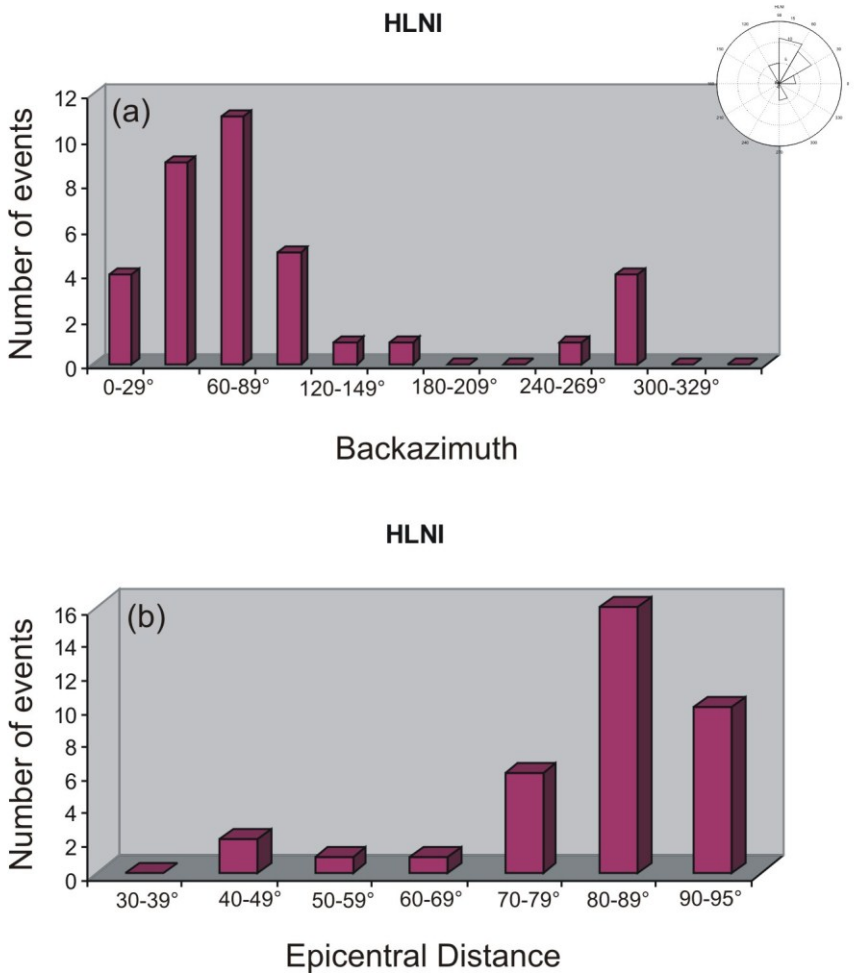

Fig. 56- *Distribution of events according to their (a) backazimuth, (b) epicentral distance with respect to HLNI station.*

• Then we observe a clear and coherent phase at roughly 5.0-5.5. We attribute this pulse to be the first multiple of a subcrustal discontinuity 8-9 km depth. If we assume an average P-wave crustal velocity of between 4.7 and 5.0 km/s, and a V_P/V_S ratio of 1.73, then the depth of the discontinuity generating the 5.0-5.5 s pulse is 8-9 km. The P_S, the first and second multiples of a subcrustal discontinuity 8-9 km depth should be observed at ca. 1.4 s (P_S), at ca. 5.0 s (P_PP_S) and at ca. 6.3 s (P_SP_S+P_PS_S). The P_S phase has a

relatively constant arrival time for most azimuths, although it appears to arrive slightly latest, at ~5.1-5.2 s, for backazimuths between 90° and 100°.

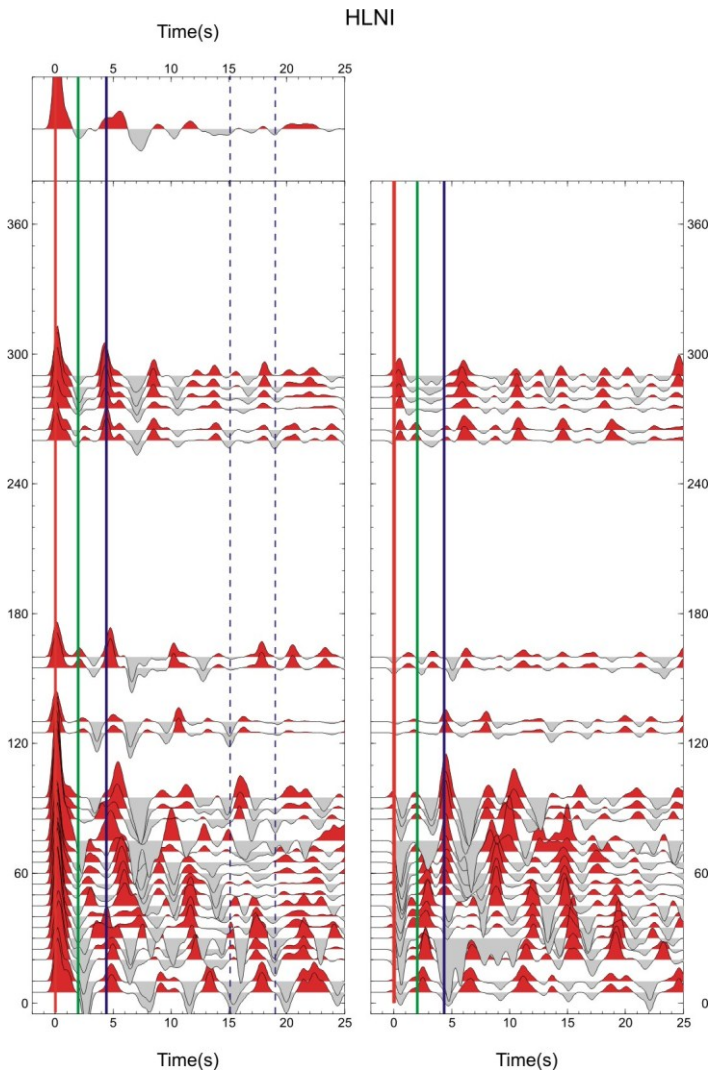

Fig. 57- *Binned RF dataset for Radial (left) and Transverse (right) components plotted as a function of the time (s) and the BAZ (°) at HLNI station. The direct P-wave arrival time is taken as the origin time. Red and gray areas indicate negative and positive pulses, respectively. Upper panel displays the average RF. Blue line marks the pulse related to the crust-mantle transition (see text for details).*

Considerable energy is visible in the tangential component traces. In particular:

- Some transverse energy is present at T=0.0 s. The polarity of this pulse appears to change from positive to negative between 90 and 270°. The direct P arrival appears in a two-lobed pattern, an effect produced by the dipping interface, as indicated by the fact that its polarity remains unchanged after 90°.
- The phase at 3.0 s shows an amplitude on the T component not null and varies with the backazimuth angle (polarity change occurs at N80° and N80+180=N260°). It could

be the first multiple of a shallow interface (if H=3.8 km and V_P=3.4 km/s: P_S=0.82 s, 1M=3.02 s, 2M=3.84 s) striking 80+90=170° or 350° in this example.

- The phase at 4.0 s shows an amplitude on the T component not null. We considered a polarity that reverses at 50° and 230°, in a striking interface at 50°+90=140° or 320°.

Looking at the receiver functions sorted by the ray parameter, the pulse at 4.2 s shows a positive moveout with increasing ray parameter, while the pulse at roughly 5.5 s decreases with increasing ray parameter (**Fig. 58**).

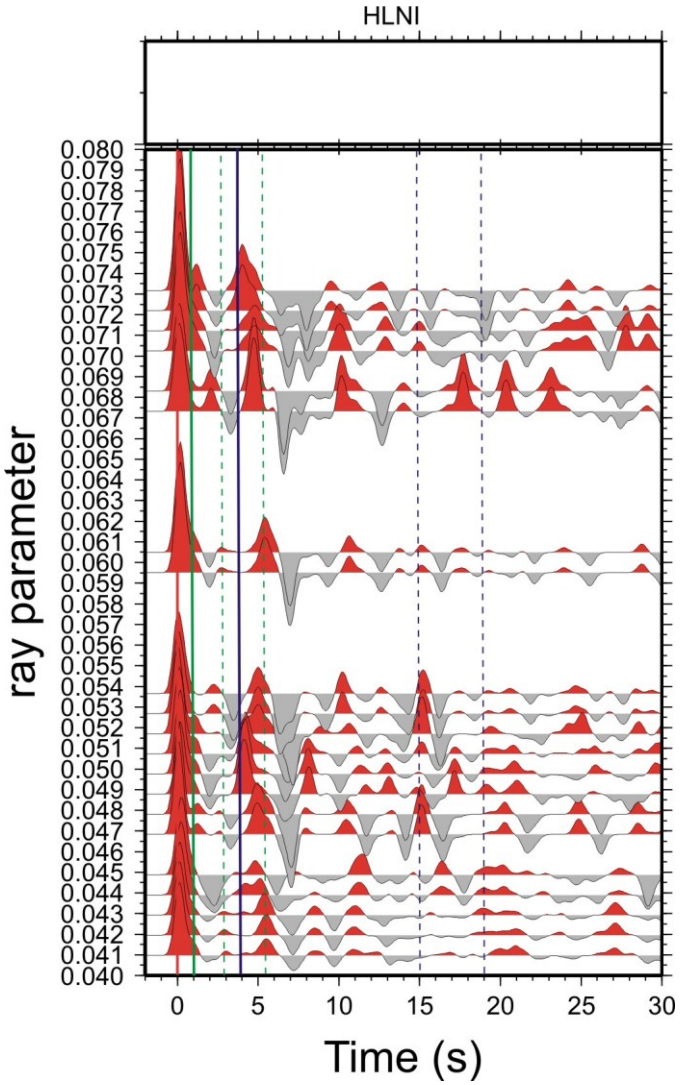

Fig. 58- *Radial receiver functions sorted by the ray parameter, computed at HLNI station. Blue line marks the pulse related to the crust-mantle transition (see text for details).*

Then, we applied a receiver function stacking technique developed by Zhu and Kanamori (2000). We searched for the maximum-stacked amplitude in the Moho depth (H) versus V_P/V_S domain in the interval of 29 to 47 km depth and 1.6 to 1.9 for the

V_P/V_S ratio. Primary phase and the two multiple conversions were weighted with the values of 0.6, 0.3 and 0.1 (100 bootstrap), respectively. For this station, the receiver function stacking technique does not provide a stable solution, showing three maxima at depth (roughly 35, 41 and 46 km): (a) V_P/V_S of 1.86 ±0.11 and thickness of 34.6±2.7 km; (b) V_P/V_S of 1.73 ±0.09 and thickness of 40.7±4.8 km; (c) V_P/V_S of 1.65 ±0.09 and thickness of 45.7±5.5 km) (**Fig. 59**). Two of these peaks agree with the receiver function profile which shows a strong converted phase at 4.2 s following the direct P arrival: (a) V_P/V_S of 1.86 ±0.11 and thickness of 34.6±2.7 km; (b) V_P/V_S of 1.73 ±0.09 and thickness of 40.7±4.8 km.

To decipher the crustal parameters, we performed forward modelling (**Fig. 60**) for a number of simple crustal models (published and averaged velocities for the crust and upper mantle have been used) by using the approach of Frederiksen and Bostock (2000).

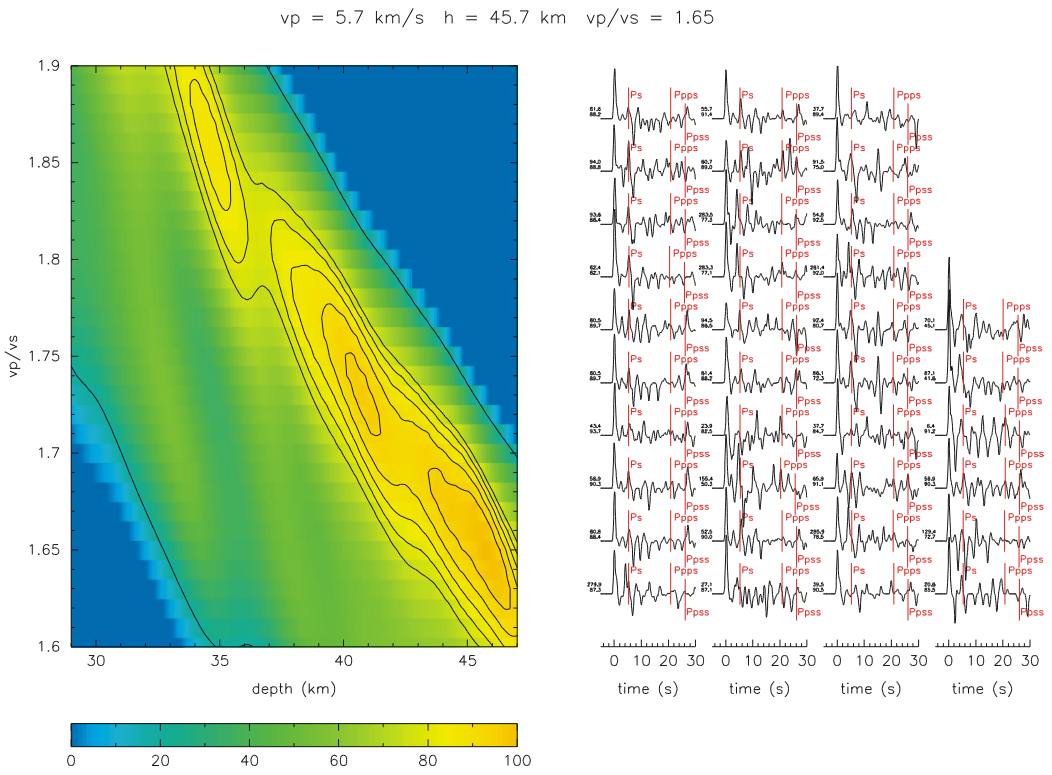

Fig. 59- *Grid search results for HLNI station according to Zhu and Kanamori (2000) method. A fixed crustal V_P value of 5.7 km/s was assumed.*

After multiple trials the following results have been achieved: • The shallower layer is modelled at 1.5 km depth and shows north-south striking, 10° east dipping interface.

• The mid-crustal layer is modelled at 8 km and the Moho at 35 km depth, dipping 25° south-westwards (strike N140°). Subtracting the station elevation (147 m) from the crustal thickness, the Moho is modelled at roughly 35.0 km.

The results can be summarized into the following main points: (1) The stacking of the 36 receiver functions for station HLNI does not provide a stable solution (two peaks agree with the receiver function profile: (a) V_P/V_S of 1.86 ±0.11 and thickness of 34.6±2.7 km; (b) V_P/V_S of 1.73 ±0.09 and thickness of 40.7±4.8 km (**Fig. 59**). (2) The predicted Moho P_S arrival time agrees with the receiver function profile which shows a converted phase at 4.2 s following the direct P arrival (if we assume an average P-wave crustal velocity of between 5.7 and 6.2 km/s, the depth of the discontinuity generating the 4.2 s pulse is ~32-35 km). (3) This phase shows the expected increase of amplitude and time delay with ray parameter for a primary converted phase. (4) We find that the synthetic models (**Fig. 60**), based on the simple-layered structure including dipping layers, reproduce the major characteristics of the real data (**Fig. 57**).

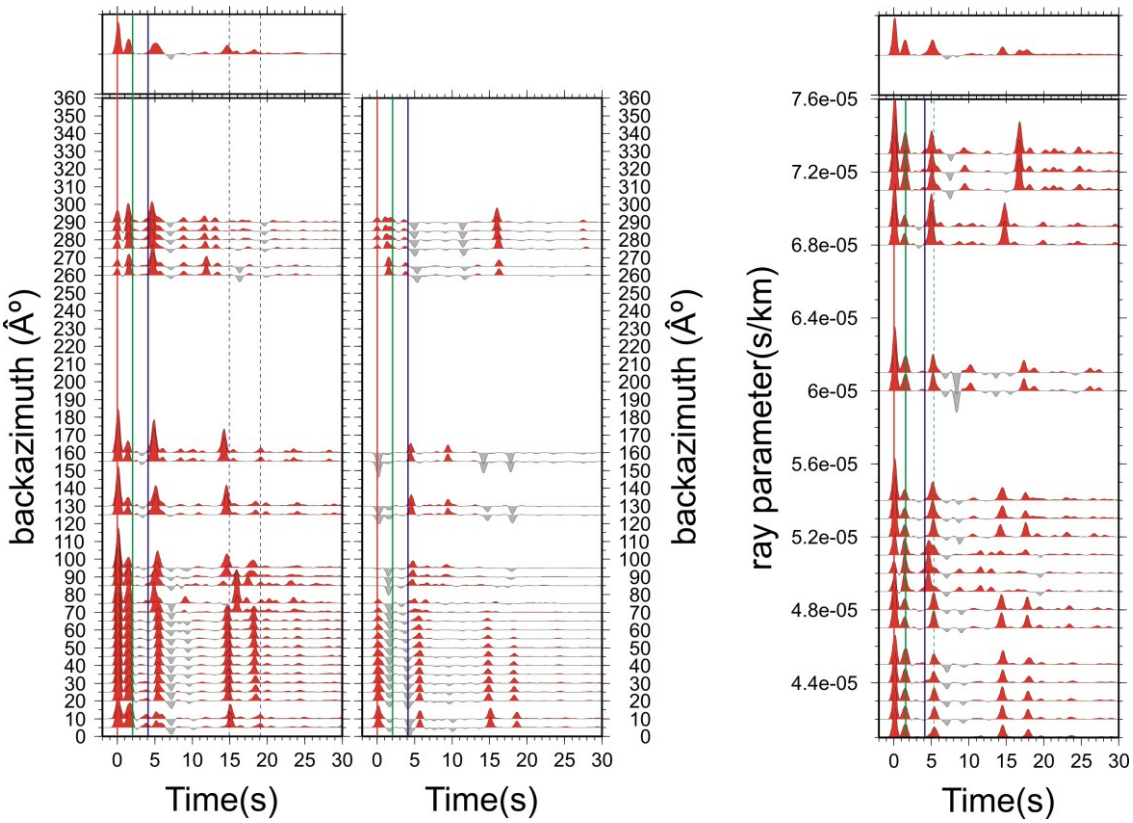

Fig. 60- *Synthetic radial and transverse RF components vs. backazimuth (on the left), computed at HLNI station by using the approach of Frederiksen and Bostock (2000). Synthetic radial RF components vs. ray parameter (on the right).*

No estimate from previous work was available for HLNI. The value calculated here,

35 km, therefore cannot be tested against previous work. Nevertheless, the RF data from station HLNI, just 16 km and 28 km north of station HCRL and SSY, respectively, indicate a markedly different crustal structure from those beneath HCRL and SSY, indicating a relatively sharp change in the crustal thickness and composition between the three stations. For locations such HLNI station, further work must be done and additional data should be provided to analyze the plausibility of the crustal thickness.

4.2.1.8 RAFF

An example of problematic station is RAFF, the western-most station of the network, located on the complex units of the Appenninic-Maghrebian Chain (**Fig. 22** and **Table 1**), 31 km far from HVZN and 47 km far from HLNI stations (see **Fig. 61** for the distribution of events according to their backazimuth and epicentral distance).

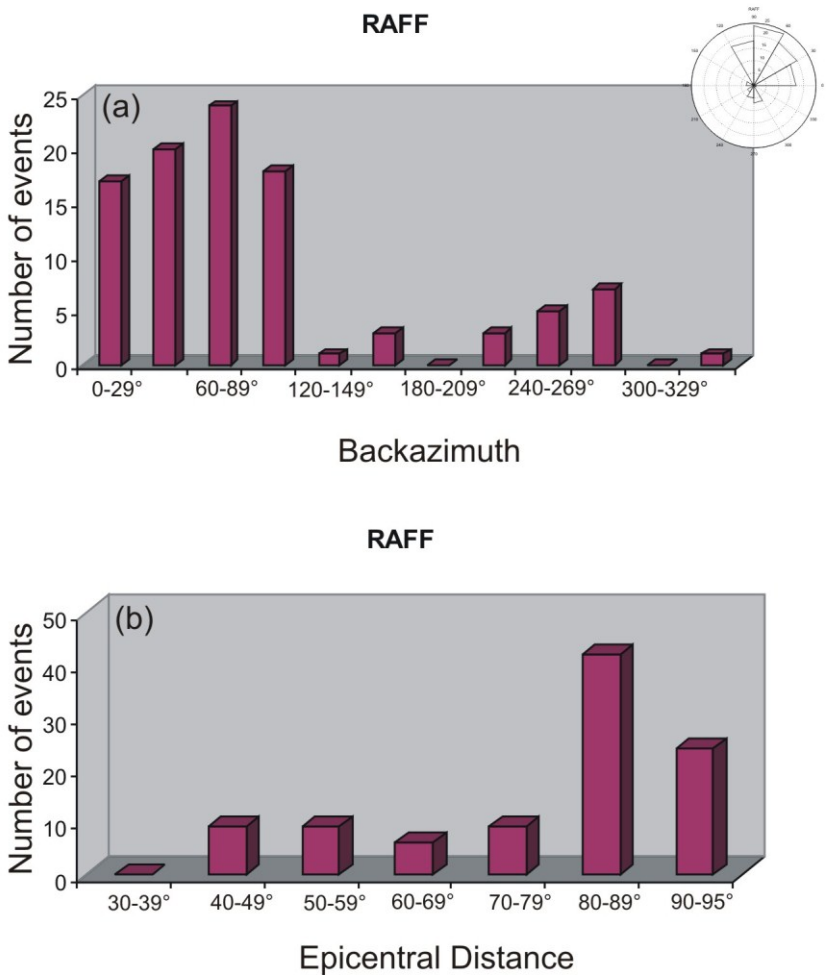

Fig. 61- *Distribution of events according to their (a) backazimuth, (b) epicentral distance with respect to RAFF station.*

Receiver functions from this station (**Fig. 62**) are noisier and less coherent than for the other stations, with higher energy levels on the transverse component, probably resulting from near-receiver scattering associated with crustal heterogeneity. Looking at the stack (**Fig. 62**), comprising of 99 traces, it is characterized by a relatively low amplitude first arriving P-wave, a relatively high amplitude wave arrival at approximately 2.0 s and a lower amplitude phase roughly at 4.2 s.

It should be pointed out, however, the surprising feature highlighted in the very first seconds of the receiver functions. The direct P pulse on radial components is really low and displays reverse polarity for teleseisms coming from BAZs between 20-30° and 250-280° (its polarity is positive for the other BAZs).

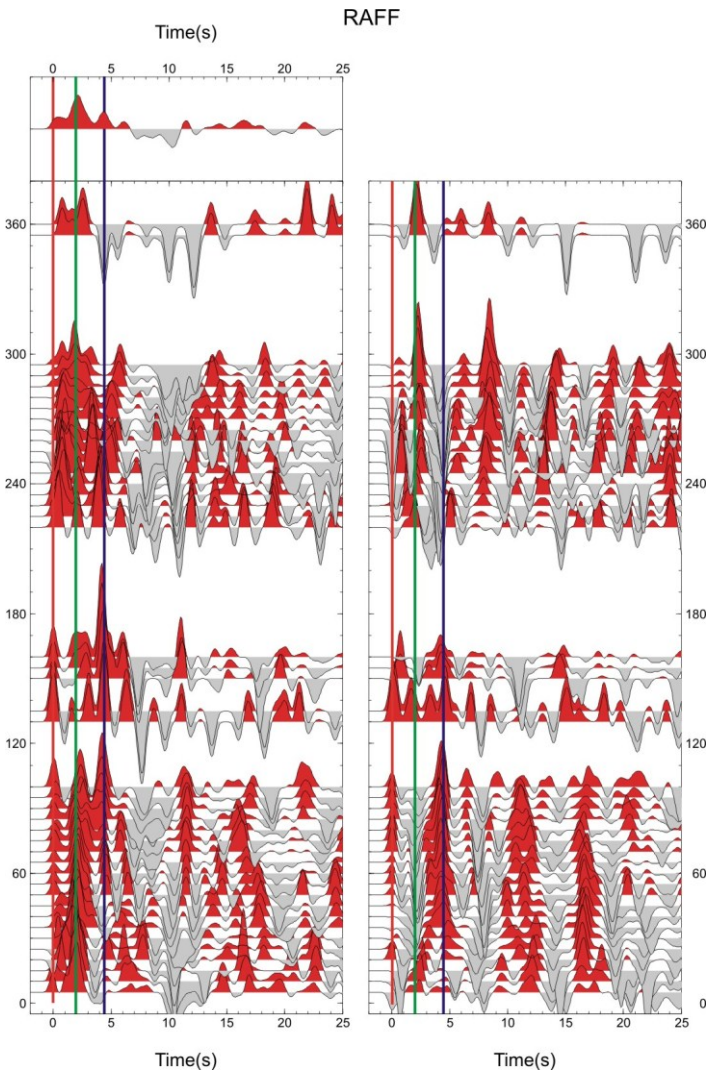

Fig. 62- *Binned RF dataset for Radial (left) and Transverse (right) components plotted as a function of the time (s) and the BAZ (°) at RAFF station. The direct P-wave arrival time is taken as the origin time. Red and gray areas indicate negative and positive pulses, respectively. Upper panel displays the average RF. Blue line marks the pulse related to the crust-mantle transition (see text for details).*

Lucente et alii (2005) demonstrated that to obtain the direct P pulse reversal on the radial component of a RF, a percentage of more than 40% (positive or negative) anisotropy (pure P or P+S) is needed. Such an anisotropic percentage by far exceeds the maximum crustal anisotropy values reported in the literature, both for heavily fractured rocks and for rocks with uniformly oriented foliation, whose strongest observed anisotropy percentages are in the range of 10-20% (e.g. Crampin, 1994; Godfrey et alii, 2002). Thus, Lucente et alii (2005) ruled out the anisotropy as first-order factor determining the direct P pulse reversal on the radial components of the RFs, concentrating on the steep interface/strong seismic velocity contrast cause. In particular, the presence of a strong upper crustal discontinuity beneath this station makes data distribution with respect to backazimuth (**Fig. 62**) and ray parameter (**Fig. 63**) quite sparse and the stacking result strongly biased.

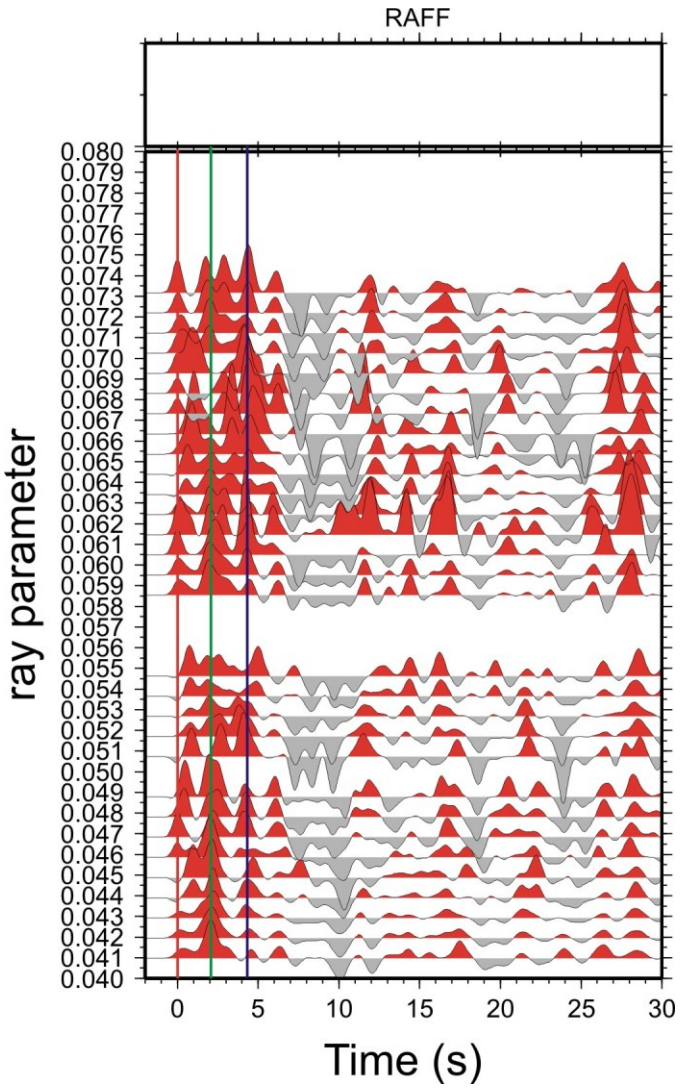

Fig. 63- *Radial receiver functions sorted by the ray parameter at RAFF station. Blue line marks the pulse related to the crust-mantle transition (see text for details).*

As a consequence, the grid search (Zhu and Kanamori, 2000) converged on the smallest crustal value in the range (as small as 17 km in the tests we have performed). As we do not expect a crustal thickness less than 25 km in the Hyblean Foreland, we limited the search range to values in excess of 25 km, obtaining the stacking surface in **Fig. 64**, which displays two clearly distinct maxima at depth. For the first peak: V_P/V_S=1.81 and H=29.9 km; for the second peak: V_P/V_S=1.68 and H=35.4 km. In the case of multiple peaks in *S(H, V_P/V_S)*, information on the crustal thickness and V_P/V_S ratio from nearby stations or other sources can help to resolve this ambiguity.

Due to the high level of transverse energy and the variability of the RFs with backazimuth, synthetic receiver functions were not performed for this station. A very complex model, combining both anisotropy and dipping discontinuities, would be required to qualitatively match the observed RFs pattern. It should be pointed out, however, that no estimate from previous work is available for RAFF station.

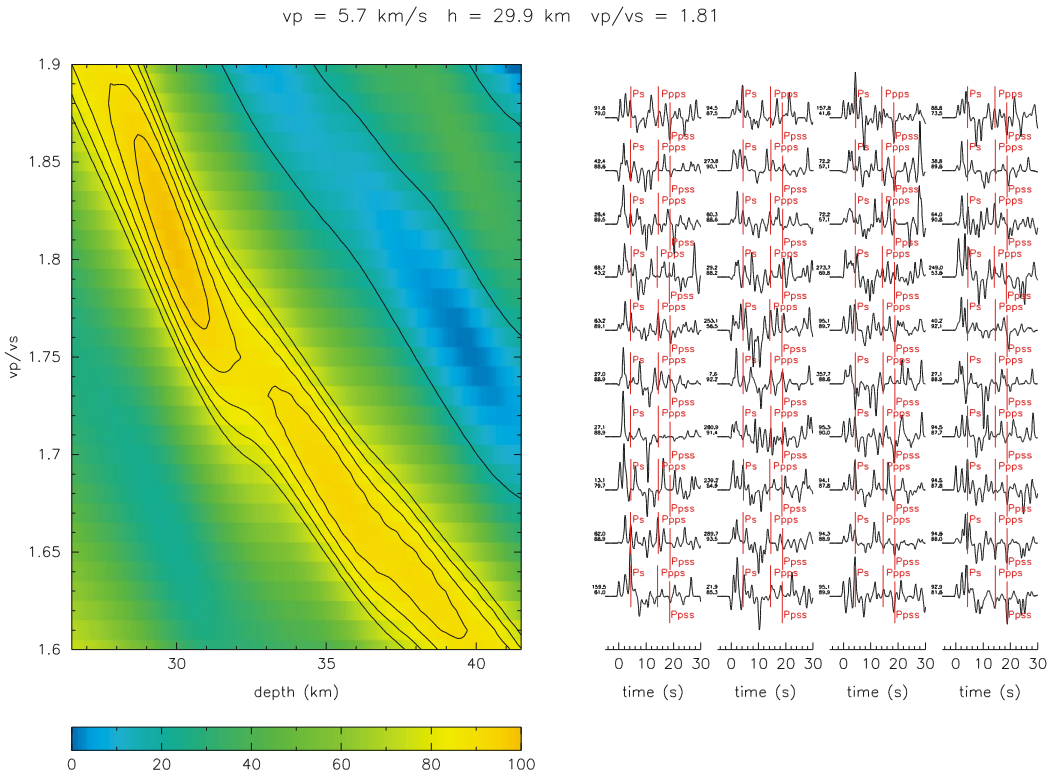

Fig. 64- *Grid search results for RAFF station according to Zhu and Kanamori (2000) method. A fixed crustal V_P value of 5.7 km/s was assumed.*

Chapter 5

5.1 Results and Conclusions

The data analysis presented in Chapter 4 provides a clear picture of the geometry of the major crustal structures beneath southeastern Sicily (Italy), giving details for a qualitative interpretation of the results. Only large teleseismic earthquakes (see **Appendix A**), meaning earthquakes that occurred between 30 and 95 degrees from an average location between all of the stations, with magnitude 6.0 and larger, were used to compute receiver functions with a maximum frequency of 1.24 Hz by using an iterative deconvolution method. From analyzing 2-8 years of global seismicity, we obtained more than 500 usable receiver functions, giving an average of 66 receiver functions for each of the 8 recording stations deployed over the region. Although some backazimuths are underrepresented due to the characteristics of global seismicity, the available traces usually allow tracking the Moho conversion over a broad azimuthal range.

This study constrained the crustal structure under single seismic stations with very closed spacing stations (~15-20 km). See **Tables 1** and **2** for seismological station parameters (including station code, latitude, longitude, elevation, recording time and seismometer type) of broadband instruments. As already illustrated through the data examples, receiver functions indicate significant regional and local variations of crustal structure with delay times of the Moho conversions that range from 3.7 s (HAGA station) to 5.1 s (HMDC station). In particular, a prominent Moho arrival can be observed at most of the stations at 4-5 s corresponding to an average crustal thickness of 30-40 km assuming a crustal velocity of 5.7-6.2 km/s and a V_P/V_S ratio of 1.73. Another P_S conversion observed at about 0.5 s can be attributed to a sedimentary layer, significantly located below the surface, while the pulse observed at about 2 s is attributed to a mid-crustal discontinuity located at ~9-12 km depth (with the arrival time of the negative multiple at about 6-7 s). Then, a negative arrival (at about 8-10 s) is detected in most of the stacks, indicating (1) the top of a low velocity region varying between 80-90 km, and/or (2) a negative multiple of a mid-crustal discontinuity 13-14 km depth. Between all of the stations, HLNI and RAFF present the most indeterminate result of all, with drastically time-varying arrivals as a function of incoming direction (backazimuth). This may be the result of a lateral heterogeneity in the crust, multiple layers, or a steeply dipping structure below these stations. Nonetheless, it is evident that simple 1D modelling cannot yield relevant and acceptable results. Further studies into the anisotropy of the area may help to better interpret and elucidate these complex

receiver functions.

As example, **Fig. 65** displays radial and transversal RF components, computed at three stations along a north-south profile, probing the structure of the north (HLNI), the internal (SSY) and external zones (HAVL) of the region. As we can observe, there are differences in the amplitude and character of the Moho and mid-crustal P_S phases between the stations, indicating spatial changes in the nature of the transition between the crust and the upper-mantle, as well as in the mid-crustal discontinuity. A prominent Moho arrival (**Figs. 65** and **66**) can be observed at 4 s at SSY and at 5 s at HAVL station corresponding to an average crustal thickness of 30-33 km and 37-40 km, respectively, assuming an average P-wave crustal velocity of between 5.7-6.2 km/s and a V_P/V_S ratio of 1.73. Some ambiguity indeed exists with the identification of the pulse corresponding to the Moho conversion at HLNI station.

Looking at the average crustal V_P/V_S ratio, estimated by using the grid-search algorithm introduced by Zhu and Kanamori (2000), it varies significantly throughout the region, indicating for some stations implausible values due to the superposition of unrelated phases or grid search maxima poorly constrained. In particular, in the investigated region average crustal values (1.73) to very high values (about 1.87) in the central portion of the Foreland have been obtained, showing areas with similar behaviour but also significant lateral changes. Recently published seismic velocity models from Scarfì et alii (2007) and Piana Agostinetti and Amato (2009) show relatively high V_P/V_S ratios as well. Variability of V_P/V_S probably reflects noise, thick near surface deposits and great intracrustal complexity. In general, the V_P/V_S crustal average does not allow to define the crustal composition and structure in detail, but can provide only valuable information on the gross crustal architecture. Nevertheless, it must be considered that the V_P/V_S values obtained by this RF analysis are average values for the whole crustal volume below each station, and therefore both shallow sedimentary layers and deep basement rocks contribute to these estimates, possibly compensating each other in some areas. A more detailed analysis of the layered structure of the crust is needed to interpret the V_P/V_S values throughout the region, trying to discriminate among the contributions of the different units composing the complex crustal structure of the region.

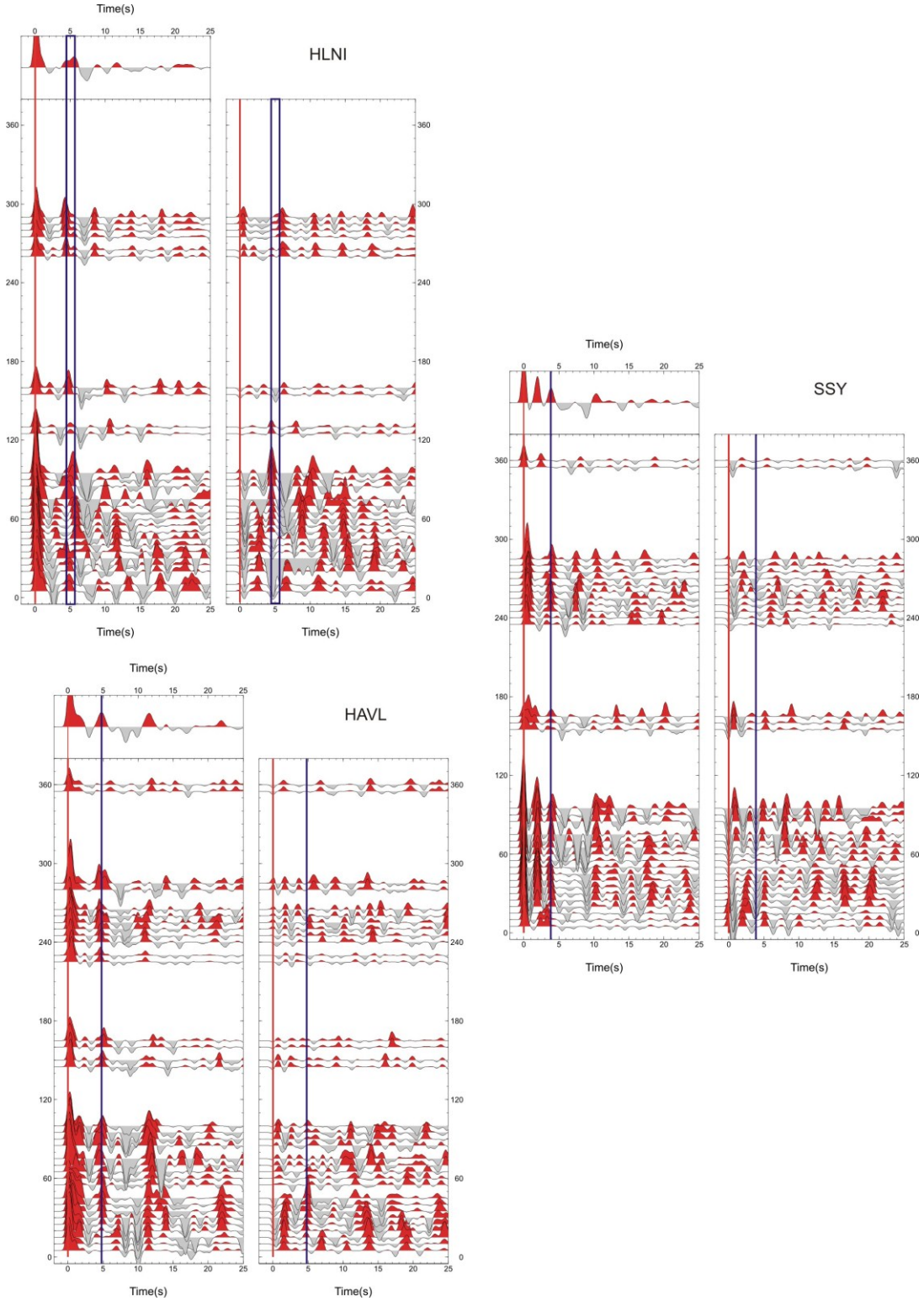

Fig. 65- *Binned RFs for Radial (left) and Transverse (right) components plotted as a function of the BAZ (°) at three seismic stations (HLNI, SSY and HAVL) along a north-south profile.*

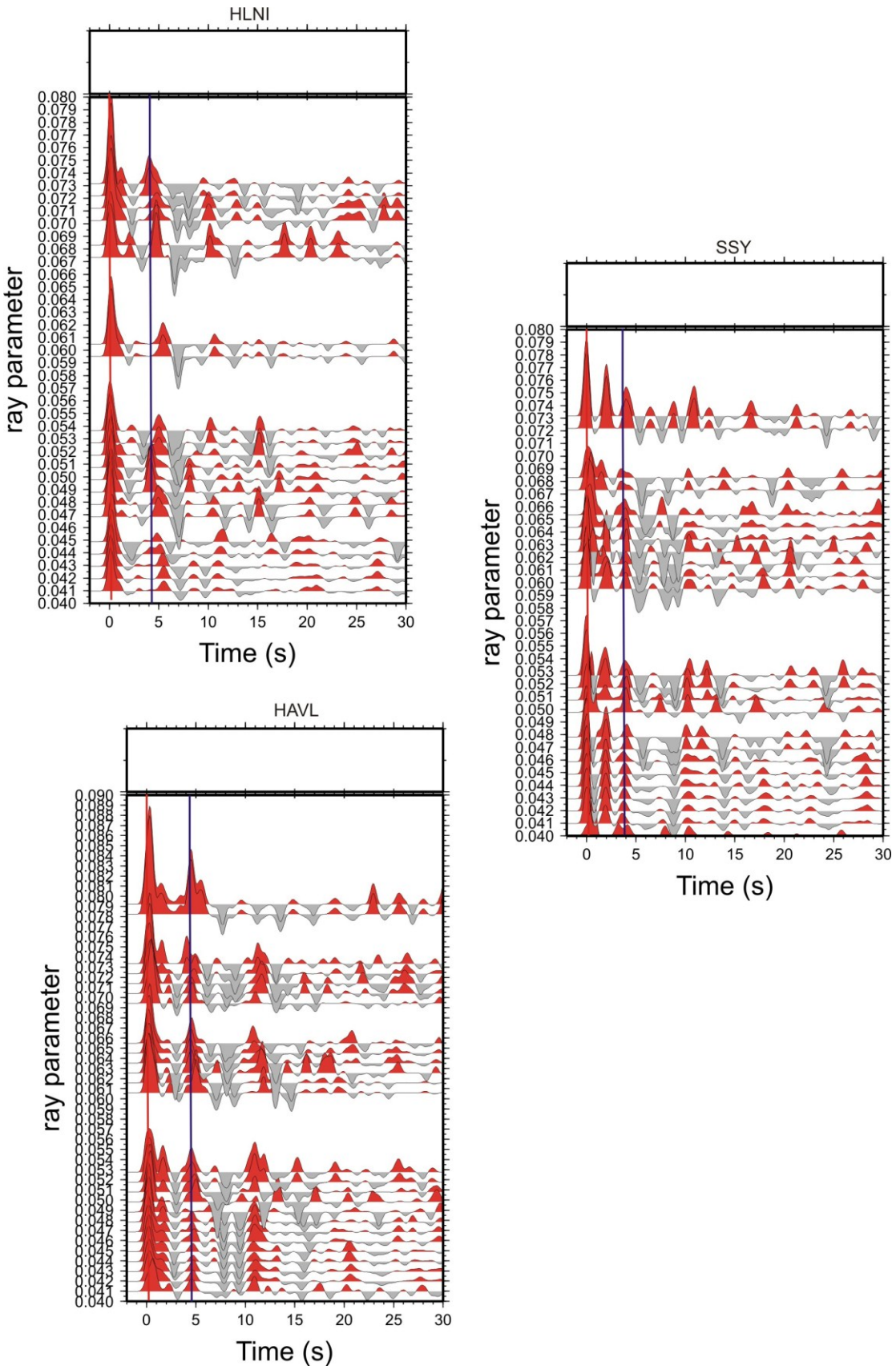

Fig. 66- *Binned RFs for Radial (left) and Transverse (right) components plotted as a function of the ray parameter at three seismic stations (HLNI, SSY and HAVL) along a north-south profile.*

Additional confidence on the thickness and crustal V_P/V_S ratio have been gained by examining the computed RF uncertainties. For most stations, the 2 standard deviations (STD) for 200 bootstrap error analysis show ±0.05 for the V_P/V_S and ±2.5 km in Moho depth, though a few stations have somewhat larger errors (i.e. HVZN). As horizontal resolution of the Moho depth, we considered the radius of the first Fresnel zone (Saunders et alii, 1998; Ryberg and Weber, 2000) associated with the incoming S wave. In our case, the resolution for a 30-35 km deep Moho, a crustal S wave velocity of 3.58 km/s and a typical frequency of 1.24 Hz, is of the order of 13-14 km.

A more detailed waveform modelling (Frederiksen and Bostock, 2000) underlined that receiver functions can be well fit using a 2- or 3-layer model containing a sedimentary layer at 2-4 km and/or a mid-crustal discontinuity located at ~9-12 km depth, using constant seismic properties for each layer. The mid-crustal discontinuity is more pronounced beneath the southernmost stations. Generally, Moho depths range between 29 and 30 km in the central part (SSY, HCRL, HAGA), whereas it got up to 37-38 km in the southern part of the study area (HMDC and HAVL) and up to 35 km westwards (HVZN) and northwards (HLNI), in a total distance of about 50 km. The results of the waveform modelling are summarized in **Fig. 67**. The numbers represent the depth of the Moho in kilometres, corrected for the station elevation, beneath each station.

The most relevant observation is the significant deepening of the Moho discontinuity beneath the southern and northern portions of the region with Moho changes in depth of nearly 5-8 km that occurs over a very short distance.

Within the associated uncertainty, these crustal estimates (depth and average V_P/V_S ratio) are close enough to match the results of previous studies (Cassinis et alii, 2003; Finetti, 2005; Piana Agostinetti and Amato, 2009), adding original information where previous data were lacking or uncertain. Some problem in matching exists when deep crustal structures preclude model accuracy.

Looking at the seismicity pattern provided in Section 2.2.3 (work in progress), the spatial distribution of the 885 earthquakes ($1.0 \leq Ml \leq 4.6$), recorded from January 1994 to June 2012 in southeastern Sicily (Italy), highlights two important features. First, a clear trend that shallows from north to south (S-N cross-section in **Fig. 14**) and second, a seismicity pattern with earthquakes getting shallower in the central part of the region and earthquakes getting deeper shifting westwards and eastwards (W-E cross section in **Fig. 14**). This earthquake spatial distribution can be indicative of a crustal thinning just

of the inner part of the region, agreeing with the results herein.

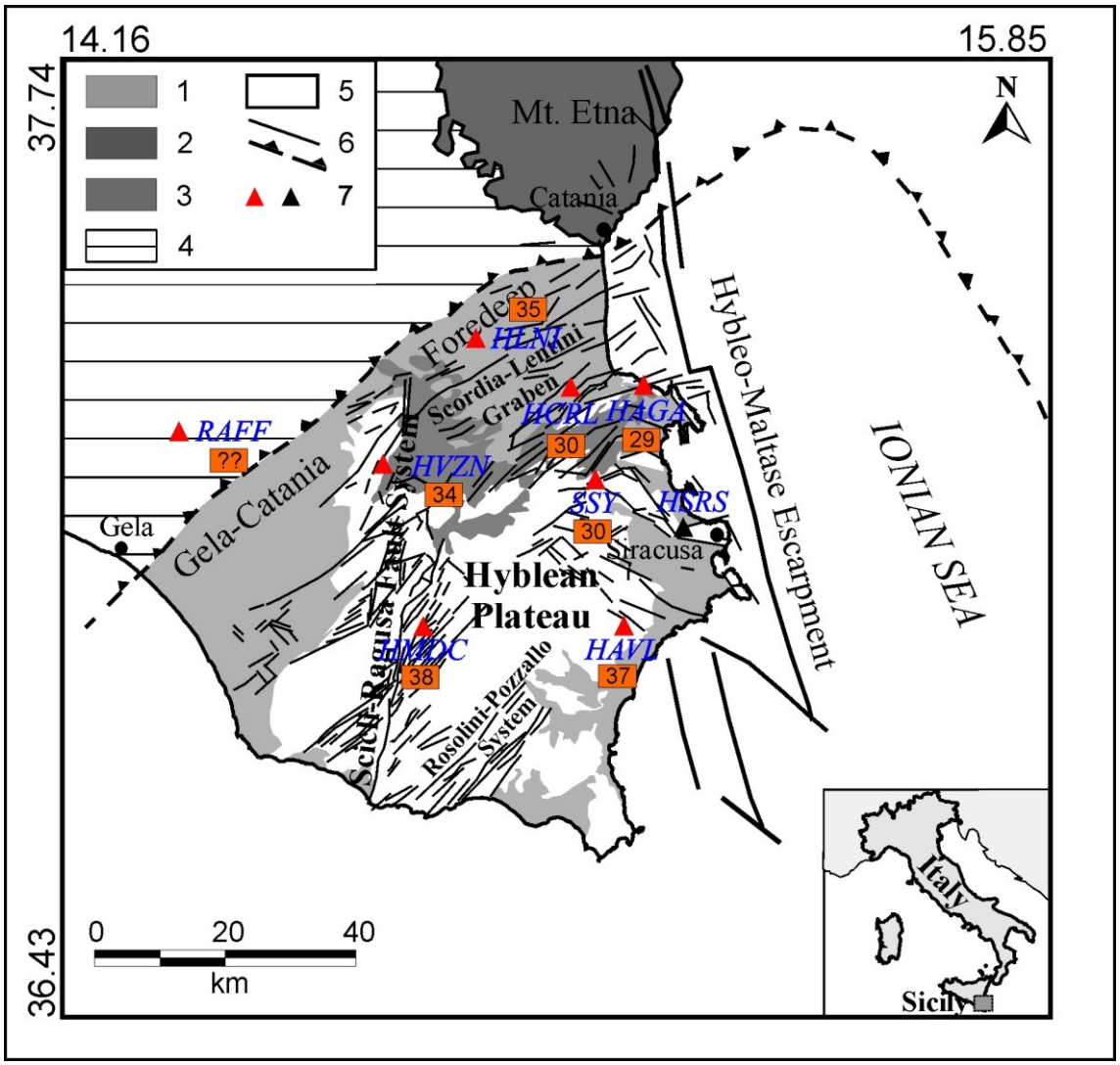

Fig. 67- *Map of southeastern Sicily (legend as in Fig. 22) showing the estimated Moho depths from forward modelling (Frederiksen and Bostock, 2000). Numbers represent the depth of the Moho in kilometers beneath each station.*

Looking at some recent published papers, Piana Agostinetti and Amato (2009), applying the stacking method of Zhu and Kanamori (2000), estimated Moho depth in southeastern Sicily. It ranges from the shallowest in the northeast (SSY=28.6±6.8 km) and west (HMDC=34±1.5 km, HVZN=33.5±9.3 km) to the deepest in the southeast (HAVL=41.5±11 km) and an average V_P/V_S of 1.8 or slightly above. Recent modelling of receiver functions (Miller and Piana Agostinetti, 2012) showed contrasting results with Moho depth ranging from the shallowest in the southeast (23 km beneath HAVL) to the deepest in the northwest (~35 km beneath HVZN). In this context, the position of Mt. Etna, situated on the margin of the Hyblean Foreland, has been suggested to be the

result of asthenospheric upwelling along slab tear faults (e.g. Gvirtzman and Nur, 1999; Doglioni et alii, 2001; Faccenna et alii, 2005, 2011; Miller and Piana Agostinetti, 2011). The thinnest lithosphere beneath Sicily imaged with S-RFs (Miller and Piana Agostinetti, 2011, 2012) is positioned on the Foreland side of the proposed tear fault and closest to Mount Etna volcano. Miller and Piana Agostinetti (2011) interpret the thinned continental lithosphere near the volcano as being thermo-mechanically modified by toroidal flow around the edges of the subducting oceanic lithosphere of the Calabrian arc due to rollback.

In order to extract first-order information about the crustal structure beneath some station located northwards from the Hyblean Foreland and to make this work, in someway, comparable to these studies recently published, I have chosen to show the radial and transverse receiver functions from ECNV (Catenanuova) station (**Fig. 68**).

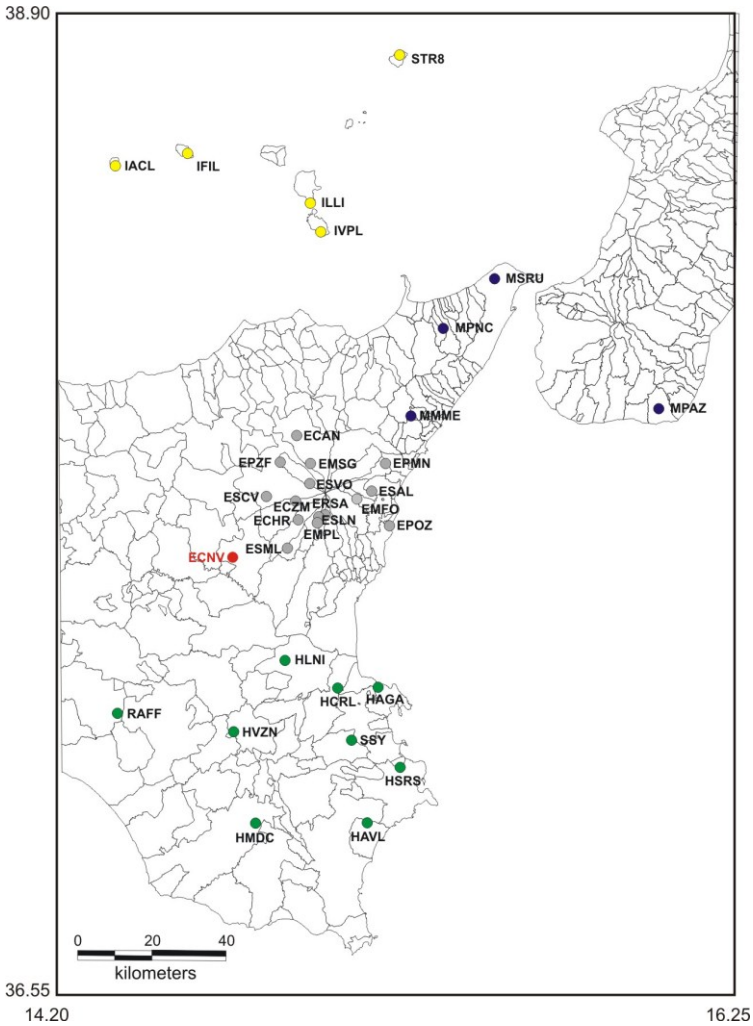

Fig. 68- *Map of eastern Sicily showing the location of ECNV station (red circle) with respect to the Hyblean stations (green circles), Etnean stations (gray circles), Messinian stations (blue circles) and Eolian stations (yellow stations).*

The location of ECNV site, placed on the Appennine-Maghrebian units at a distance of about 31 and 52 km from HLNI and RAFF stations (**Fig. 68**), respectively, makes it a favorable candidate for highlighting the change (if it exists) in the bulk seismic properties of the crust under the Appennine-Maghrebian units with respect to those ones of the Hyblean Foreland.

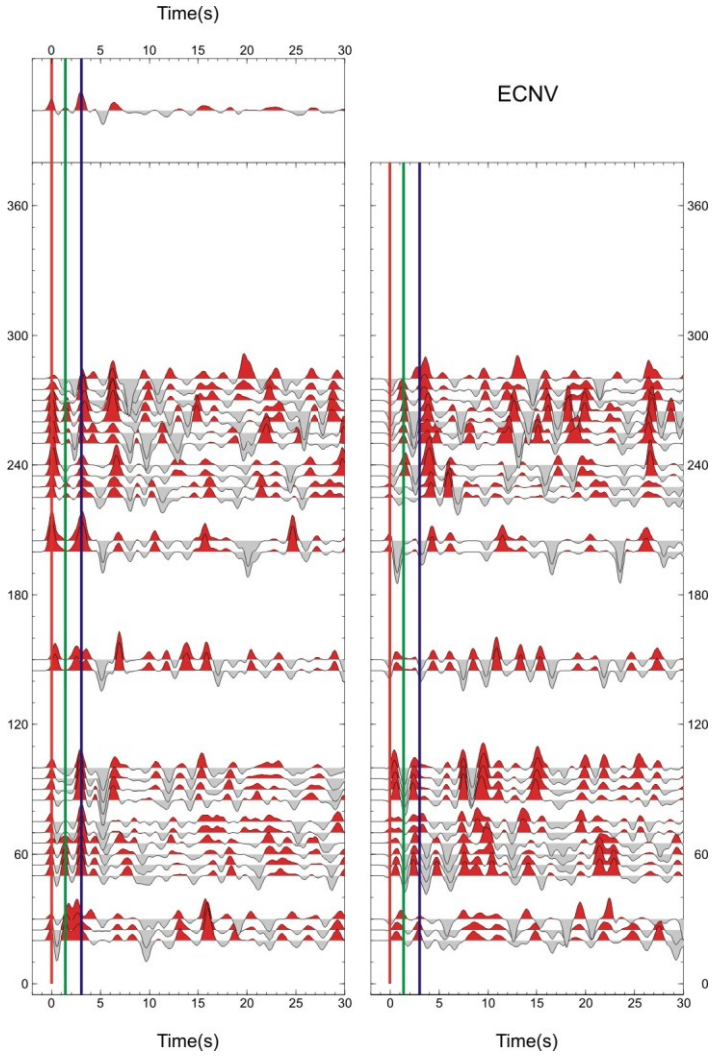

Fig. 69- *Binned RF dataset for Radial (left) and Transverse (right) components plotted as a function of the time (s) and the BAZ (°) at ECNV station. The direct P-wave arrival time is taken as the origin time. Red and gray areas indicate negative and positive pulses, respectively. Upper panel displays the average RF. Blue line marks the pulse related to the crust-mantle transition (see text for details).*

Primary phase and the two multiple conversions were weighted with the values of 0.6, 0.3 and 0.1, respectively. The stacking surface (normalized to 100%) is shown in **Fig. 70** along with the 1σ confidence ellipses (red) from the bootstrap analysis. The best-fit value provides a surprisingly thin crust which clearly highlights the changes in the bulk seismic properties of the crust under the Appennine-Maghrebian units with

respect to the ones of the Hyblean Foreland. However, an explanation on the sharp change in crustal thickness between these two domains is out of the scope of this thesis and it will be the topic of a separate study.

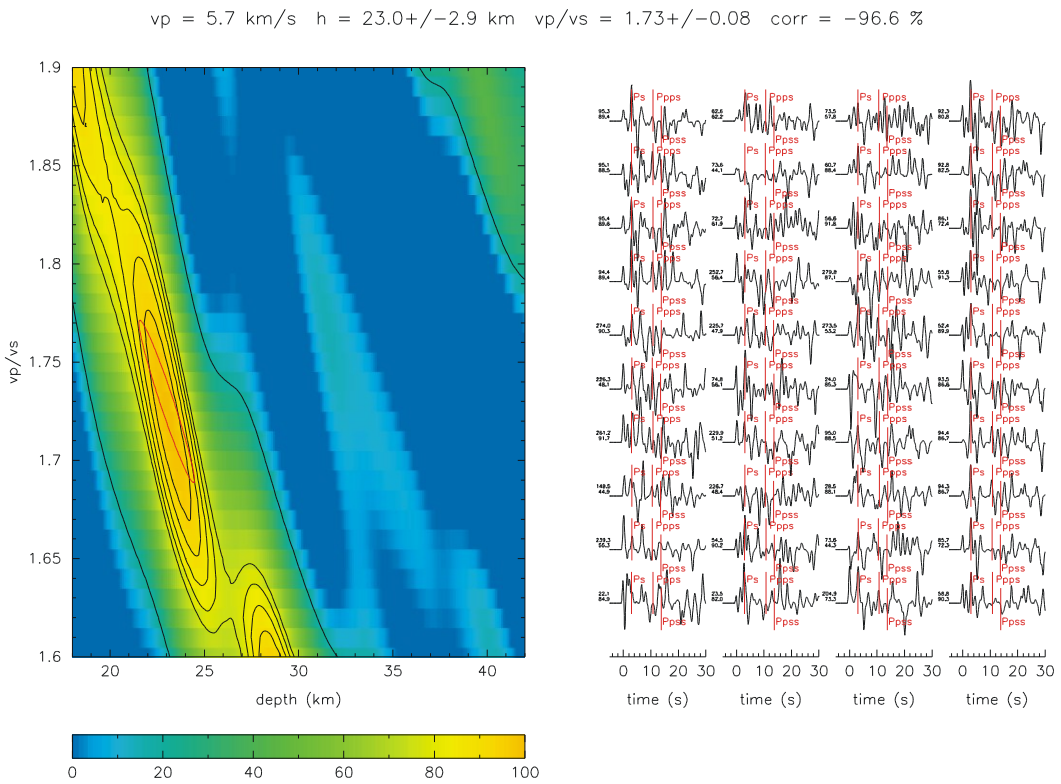

Fig. 70- *Grid search results for ECNV station according to Zhu and Kanamori (2000) method. A fixed crustal V_P value of 5.7 km/s was assumed.*

Chapter 6

6.1 Concluding remarks

Southeastern Sicily (Italy) is acknowledged to be a tectonically complex region, due to the continental collision between the Nubian and Eurasian plates (see **Fig. 2**). This study aims (1) to provide an image of the crustal complexities and Moho geometry across this region, employing the P receiver function (P-RF) technique, and (2) to offer a tentative interpretation of the tectonic evolution and of the inferred geodynamic regime. The investigation of the crustal structure in southeastern Sicily revealed strong lateral variations, with Moho depths ranging between 29-30 km in the central part of the study area, up to 38 km in the southern part and up to 35 km northwards, in a total distance of about 50 km (HLNI-HAVL distance). Looking at the results of the forward modelling, summarized in **Fig. 67**, the relatively short distance over which the crustal thickness changes is the most important observation. In the following, we propose two alternative, plausible hypotheses for explaining these strong lateral variations.

The first hypothesis is based on the assumption that the uplift and erosion of the peripheral-bulge (**Fig. 71**), in turn controlled by thrust wedge loading and lithospheric flexure, should have resulted in the thinning of the crust towards the bulge and the consequent northward foredeep thickening. In detail, tectonic loading by orogens provides the defining feature of foreland systems, i.e. their partitioning into flexural provinces: foredeep (foreland basin), forebulge (peripheral bulge) and back-bulge (**Fig. 71**). Along the flexural profile, the uplift of the forebulge is synchronous with the subsidence of the foredeep, and is caused by the rapid lateral displacement of sublithospheric viscous mantle material as a result of lithospheric downwarp beneath the orogen and the adjacent foredeep (Catuneanu, 2004 and references therein). The width and depth of the foreland basin is determined by the flexural rigidity of the underlying lithosphere, and the characteristics of the applied load (i.e. the mountain belt). Although the degree to which the lithosphere relaxes over time is still controversial, most workers (Flemings and Jordan, 1989; Allen and Allen, 2005) accept an elastic or visco-elastic rheology to describe the lithospheric deformation of the foreland basin. Allen and Allen (2005) describe a moving load system, in which the deflection moves as a wave through the foreland plate before the load system. The deflection shape is commonly described as an asymmetrical low close to the load along the foreland and a broader uplifted deflection along the forebulge (**Fig. 71**). The transport rate or flux of erosion, as well as sedimentation, is a function of topographic

relief. For the loading model, the lithosphere is initially stiff, with the basin broad and shallow. As indicated by modelling on **Fig 71**, a lithosphere that is subject to supracrustal loading tends to relax stress leading to the deepening and narrowing of the foredeep with time (stages 1 to 3) and synchronous uplifting and narrowing of the forebulge. The bending of the lithosphere under the orogenic load controls the drainage pattern of the foreland basin, the flexural tilting of the basin and the sediment supply from the orogen.

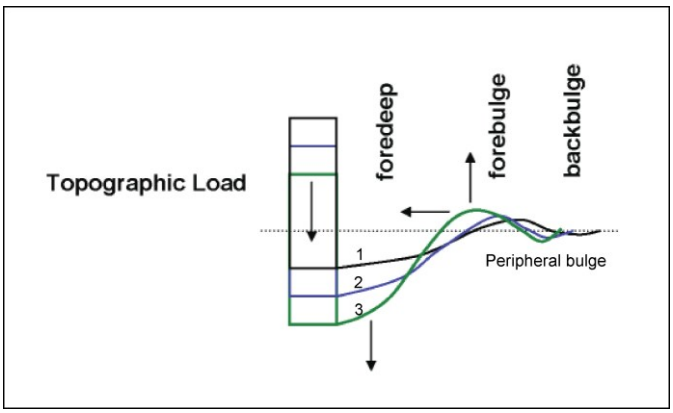

Fig. 71- *Schematic cross section of a 'typical' foreland basin (modified after Catuneanu, 2004).*

In our regional context, as also supported by Elter et alii (2003; **Fig. 72**), the strong lateral variations of the crustal thickness could have been controlled by peripheral-bulge dynamics with repeated uplift and erosion of the peripheral-bulge.

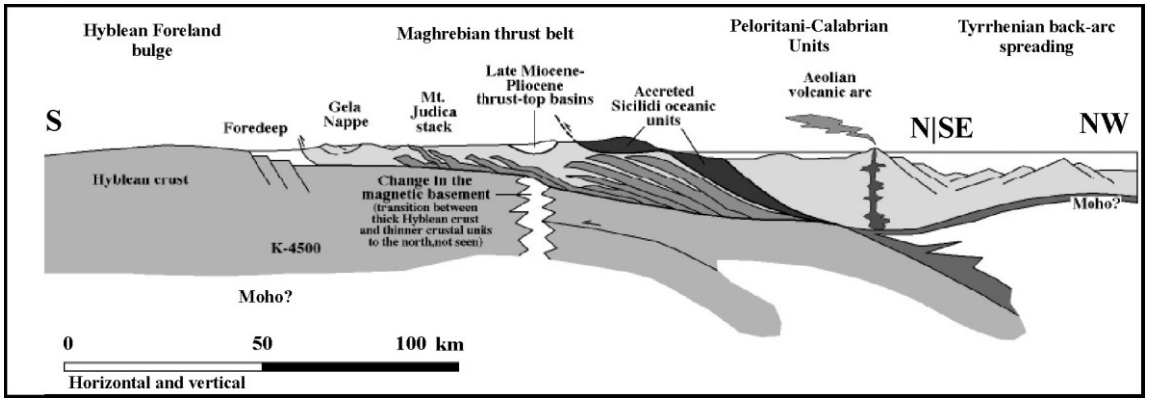

Fig. 72- *Simplified section across the eastern Sicily, from the Hyblean Foreland to the southern Tyrrhenian back-arc basin; K indicates the magnetic susceptibility (from Elter et alii, 2003).*

Additionally, as consequence of continued convergence the load migrated southeastward and the initial uplift of the forebulge region was followed by subsidence as the bulge moved onto the outer foreland (**Fig. 73**). Therefore, the entire system thrust-wedge, foredeep, forebulge and backbulge was subject to migration. Time constraint for this event (displacement-rate and whole mechanism of evolution) is less than 5 Ma years (from Early Pliocene; Lickorish et alii, 1999; Ghisetti et alii, 2009). This process could have involved the thinning of the crust towards the central part (close to HCRL, HAGA and SSY stations), where Moho lies at about 29-30 km depth, and the consequent northward and westward thickening, where Moho lies at about 35-38 km depth. This can be explained by a secondary flexure of the foreland about a NW trending axis as suggested by Billi et alii (2006). According to the cited Authors, the Hyblean foreland, resistant to subduction, has been progressively surrounded by advancing orogenic salients, which have exerted additional loads on the southwestern and northeastern sides of the Hyblean forebulge.

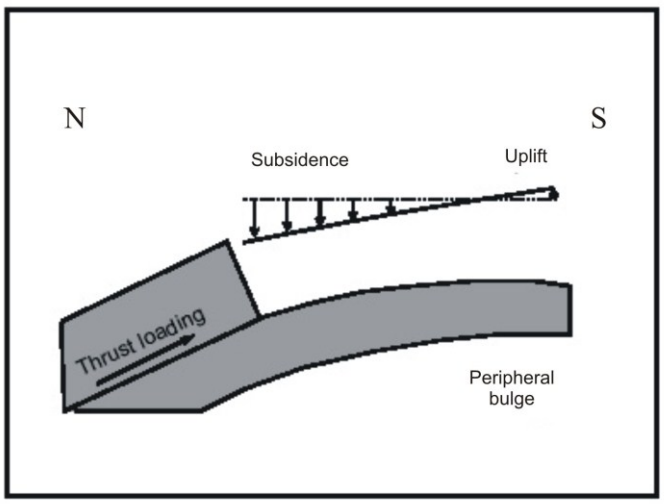

Fig. 73- *Schematic model of the development of the peripheral bulge through the Hyblean Foreland.*

The second suggested hypothesis is equally supported by geological reasons and it refers to the kinematic and dynamic model discussed in Catalano et alii (2011) about the mantle intrusion (mantle diapirism at depth) beneath the Hyblean Foreland.

The Authors explain the Recent and active contractional structures (two antithetic ENE-WSW oriented thrust-ramps), located at the northern edge of the African Foreland (**Fig. 74**), as originated from the tectonic inversion of a Lower-Middle Pleistocene

extensional basin where the Late Quaternary motions along the inverted structures were accommodated to the west by a major N-S oriented left-lateral fault zone in the last 850 ka. As a whole, the Late Quaternary contractional tectonics of SE Sicily are related to a NW-verging crustal stacking, related to a mantle intrusion active (mantle diapirism at depth) beneath the Hyblean Plateau that developed as effect of the rift-flank deformation.

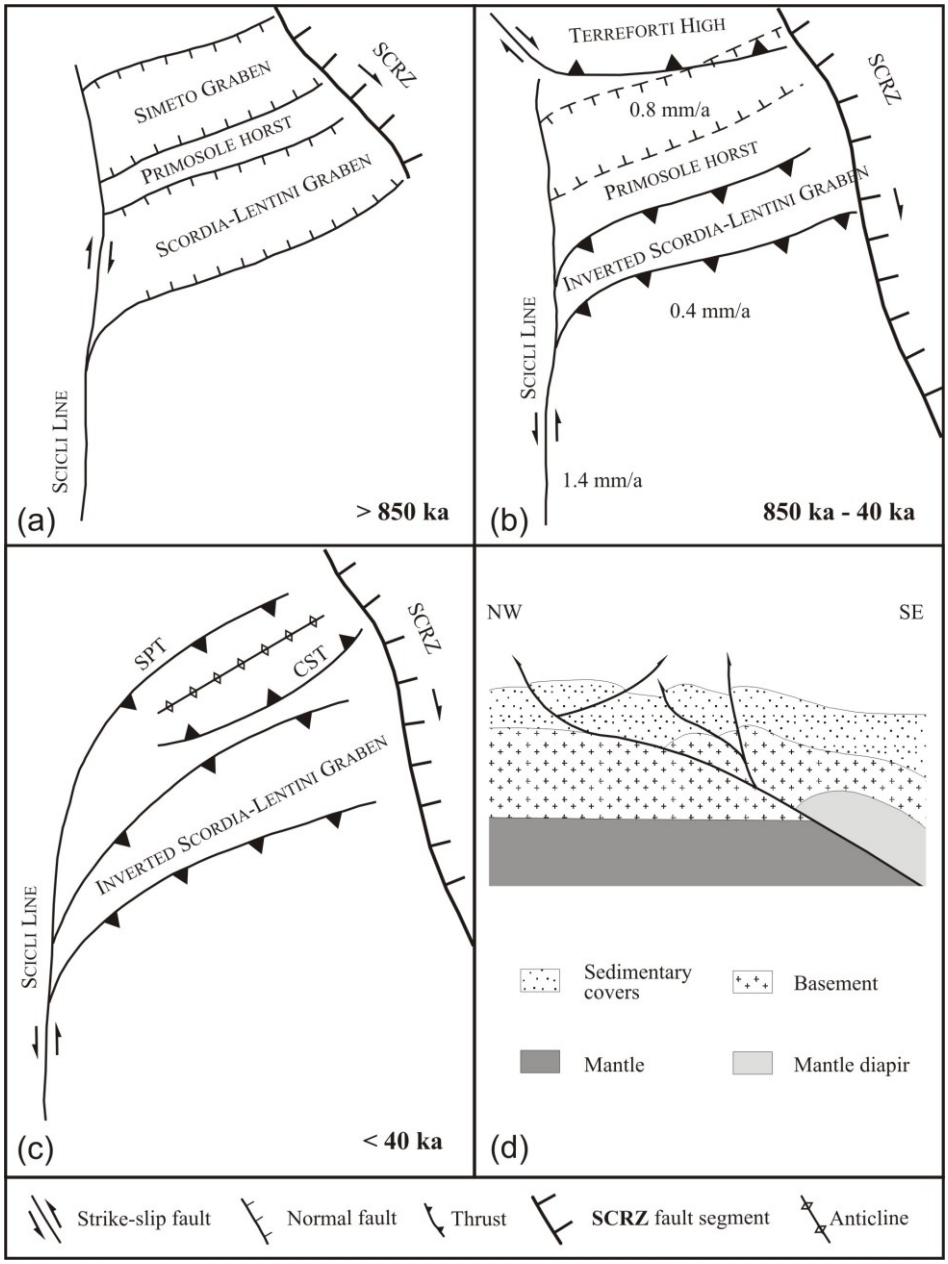

Fig. 74- *Evolution of the Late Quaternary positive tectonic inversion at the flank of the Siculo-Calabrian Rift Zone (SCRZ), in the Catania region (from Catalano et alii, 2011).*

The rate of deformation of the Late Quaternary morphological features along the bordering structures indicate an amounts of contractional-rate along the northwestern border of the block of about 1.2 to 1.3 mm/year. The displacement-rate and the mechanism of the contractional structures evolution (less than 850 ka; from Pleistocene) are shown in **Fig. 74** (see also Catalano et alii, 2011 for details).

According to this model, **Fig. 75** shows a simplified scheme (NW-SE profile) of the relation between dynamic and kinematic features of the eastern Hyblean region (after Catalano et alii, 2011) and Moho depth beneath some representative seismic stations. As illustrated in the schematic profile, the mantle intrusion (mantle diapirism at depth) beneath the Hyblean Foreland should be responsible for the thinning of the central part of the Foreland, where Moho lies at about 29-30 km.

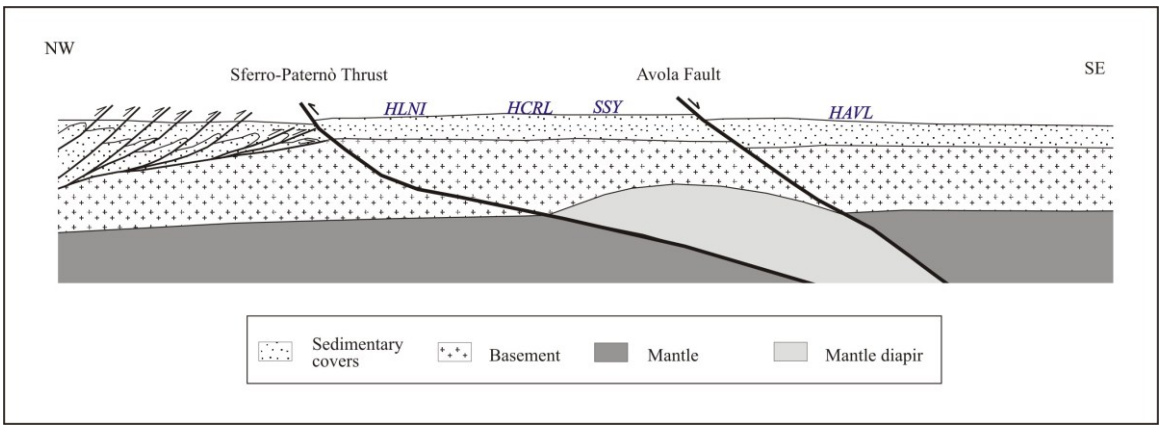

Fig. 75- *Schematic profile, not drawn to scale (modified after Catalano et alii, 2011).*

High heat flows (or high V_P/V_S volume) in the central portion of the Hyblean Foreland, as remnant heat from old volcanic centres, could be a further support for this hypothesis. However, the considerable thinning of the central part of the crust in a so short-time period (more than 5 km in less than 850 ka that means about 6 mm/year) bring us to think that the first hypothesis is the most plausible of those discussed so far.

Notwithstanding we attempted to speculate on the relatively short distance over which the crustal thickness changes, just future RF studies, based on detailed modelling of the crustal structure and anisotropy, could provide additional constraints to the hypotheses advanced in this thesis.

Acknowledgments

Un ringraziamento particolare va alla mia amica e collega Carmen Martínez Arévalo per il lavoro condiviso durante i miei numerosi soggiorni a Madrid (al Museo Nacional de Ciencias Naturales, CSIC, e al Department of Mechanical Engineering and Construction at the Universidad Politécnica di Madrid, UPM), per il sostegno professionale e prima ancora umano.

Ringrazio il mio Tutor (Prof. Stefano Gresta), il Co-tutor (Prof. Stefano Catalano) e i miei diretti superiori all'INGV di Catania per l'incoraggiamento e i preziosi consigli.

Ringrazio Giuseppe Tortorici e Flor de Lis Mancilla per l'aiuto scientifico.

Un grazie particolare ai miei amici (e colleghi) di sempre Betty, Giusy, Tiziana, Giuseppe e Salvo che in questi tre anni mi hanno supportato e "sopportato" condividendo con me lavoro e momenti di spensieratezza.

Ringrazio tutti i miei amici vicini e lontani, vecchi e nuovi per l'aiuto morale, in particolar modo ringrazio Marilena, Angela, Rosanna e Marco che con il loro sostegno e la loro amicizia mi hanno accompagnato in quest'ultima fase di stesura.

E poi non finirò mai di ringraziare mio padre, mia madre e mia sorella Paola che mi hanno sempre sostenuto in tutte le scelte che ho fatto, rendendomi con la loro pazienza e il loro affetto tutto molto più semplice. Ludovica e Benedetta per avermi regalato ogni giorno un sorriso.

Infine, ringrazio me stessa per aver avuto la forza di continuare a crederci.

References

Adam J., Reuther C.D., Grasso M., Torelli L. (2000). *Active fault kinematics and crustal stresses along the Ionian margin of southeastern Sicily*. Tectonophysics, 326, 217-239.

Allen P.A. and Allen J.R. (2005). *Basin Analysis: Principles and Applications*. 2nd ed., Blackwell Publishing, 549 pp.

Ammon C.J. (1991). *The isolation of receiver effects from teleseismic P waveforms*. Bull. Seism. Soc. Am., 81, 2504-2510.

Ammon C.J., Randall G.E., Zandt G. (1990). *On the nonuniqueness of receiver function inversions.* J. Geophys. Res., 95, 15.303-15.318.

Anderson H. and Jackson J.A. (1987). *Active tectonics in the Adriatic region*. Geophis. J. R. Astron. Soc., 91, 937-983.

Azzaro R. and Barbano M.S. (2000). *Analysis of the seismicity of southeastern Sicily: A proposed tectonic interpretation.* Ann. Geofis., 43, 171-188.

Bello M., Franchino A., Merlini S. (2000). *Structural model of Eastern Sicily*. Mem. Soc. Geol. It., 55, 61-70.

Ben-Avraham Z., Lyakhovsky V., Grasso M. (1995). *Simulation of the collisional zone segmentation in the Central Mediterranean*. Tectonophysics, 243, 57-68.

Bianca M., Monaco C., Tortorici L., Cernobori L. (1999). *Quaternary normal faulting in south-eastern Sicily (Italy): a seismic source for the 1693 large earthquake*. Geophys. J. Int., 139, 370-394.

Bianchi F., Carbone S., Grasso M., Invernizzi G., Lentini F., Longaretti G., Merlini S., Moscardini F. (1987). *Sicilia orientale: Profilo geologico Nebrodi-Iblei*. Mem. Soc. Geol. It., 38, 429-458 (in Italian).

Bianchi I., Piana Agostinetti N., De Gori P., Chiarabba C. (2008). *Deep structure of the Colli Albani volcanic district (central Italy) from receiver functions analysis*. J. Geophys. Res., 113, B09313, doi:10.1029/2007JB005548.

Billi A., Porreca M., Faccenna C., Mattei M. (2006). *Magnetic and structural constraints for the noncylidrical evolution of a continental forebulge (Hyblea, Italy)*. Tectonics, 25, doi: 10.1029/2005TC001800, 2006, 15 pp.

Brancato A., Hole J., Gresta S., Beale J.N. (2009). *Determination of seismogenic structures in Southeastern Sicily (Italy) by high-precise relative location of microearthquakes*. Bull. Seismol. Soc. Am., 99, 3, 1921-1936, doi:10.1785/0120080204.

Burdick L.J. and Langston C.A. (1977). *Modeling crustal structure through the use of converted phases in teleseismic body-wave forms*. Bull. Seism. Soc. Am., 67, 677-691.

Burollet P.F., Mugniot G.M., Sweeney P. (1978). *Geology of the Pelagian Block: the Margin and Basin of Southern Tunisia and Tripolitania*. In: Nairn, A., Kanes, W., Stelhi, F.G. (Eds.), The Ocean Basin and Margin. Plenum, New York, 331-419.

Cassidy J.F. (1992). *Numerical experiments in broadband receiver function analysis*. Bull. seism. Soc. Am., 82, 1453-1474.

Cassinis R., Scarascia S., Lozej A. (2003). *The deep crustal structure of Italy and surrounding area from seismic refraction data. A new synthesis*. Boll. Soc. Geol. It., 122, 365-376.

Catalano S., Romagnoli G., Tortorici G. (2010). *Kinematics and dynamics of the Late Quaternary rift flank deformation in the Hyblean Plateau (SE Sicily).* Tectonophysics, 486, 1-14, doi: 10.1016/j.tecto.2010.01.013.

Catalano S., Torrisi S., Tortorici G., Romagnoli G. (2011). *Active folding along a rift-flank: the Catania region case history (SE Sicily)*. Journal of Geodynamics, 51, 53-63.

Catuneanu O. (2004). *Retroarc foreland systems - evolution through time*. J. African Earth Sci., 38, 225-242.

Cernobori L., Hirn A., Nicolich R., McBride J., Petronio L., Romanelli M., the Streamers/Profiles group (1996). *Crustal image of the Ionian Basin and its Calabrian margins*. Tectonophysics, 264, 175-189.

Chen J. and Liu Q. (2000). *Wavefield features of teleseismic receiver function in laterally inhomogeneous media*. Acta Seismologica Sinica, 13, 6, 656-663.

Chironi C., De Luca L., Guerra I., Luzio D., Moretti A., Vitale M., SEALAND GROUP (2000). *Crustal structures of the Tyrrhenian Sea and Sicily Channel on the basis of the M25, M26, M28, M39 WARR profiles*. Boll. Soc. Geol. It., 119, 189-203.

Continisio R., Ferrucci F., Gaudiosi G., Lo Bascio D., Ventura G. (1997). *Malta escarpment and Mt Etna: early stages of an asymmetric rifting process? Evidences from geophysical and geological data*. Acta Vulcanol., 9, 45-53.

Crampin S. (1994). *The fracture criticality of crustal rocks*. Geophys. J. Int., 118, 428-438.

D'agostino N. and Selvaggi G. (2004). *Crustal motion along the Eurasia-Nubia plate boundary in the Calabrian arc and Sicily and active extension in the Messina Straits*

from GPS measurements. J. Geophys. Res., 109, B11402.

Di Stefano R., Bianchi I., Ciaccio M.G., Carrara G., Kissling E. (2011). *Three-dimensional Moho topography in Italy: New constraints from receiver functions and controlled source seismology*. Geochem. Geophys. Geosyst., 12, Q09006, doi:10.1029/2011GC003649.

Doglioni C., Innocenti F., Mariotti G. (2001). *Why Mt Etna?*. Terra Nova, 13, 25-31, doi:10.1046/j.1365-3121.2001.00301.x.

Du Z., Michelini A., Panza G. (1998). *EurId: A regionalized 3-D seismological model of Europe*. Phys. Earth Planet. Inter., 106, 31-62, doi:10.1016/S0031-9201(97)00107-6.

Efron B. and Tibshirani R. (1991). *Statistical data analysis in the computer age*. Science, 253, 390-395.

Elter P., Grasso M., Parotto M., Vezzani L. (2003). Structural setting of the Apennine-Maghrebian thrust belt. Lournal of International Geosciences, 26, 3, 205-211.

Faccenna C., Becker T.W., Lucente F.P., Jolivet L., Rossetti F. (2001). *History of subduction and back-arc extension in the Central Mediterranean*. Geophys. J. Int., 145, 809-820.

Faccenna C., Civetta L., D'Antonio M., Funiciello F., Margheriti L., Piromallo C. (2005). *Constraints on mantle circulation around the deforming Calabrian slab*. Geophys. Res. Lett., 32, L06311, doi:10.1029/2004GL021874.

Faccenna C., Molin P., Orecchio B., Olivetti V., Bellier O., Funiciello F., Minelli L., Piromallo C., Billi A. (2011). *Topography of the Calabria subduction zone (southern Italy): Clues for the origin of Mt. Etna*. Tectonics, 30, TC1003, doi:10.1029/2010TC002694.

Finetti I.R. (2005). *Depth contour map of the Moho discontinuity in the central Mediterranean region from new crop seismic data*. In: Finetti, I.R. (Ed.), CROP PROJECT. Deep Seismic Exploration of the Central Mediterranean and Italy, 597-606.

Finetti I.R. and Del Ben A. (1996). *Crustal Tectono-Stratigraphic Setting of the Pelagian Foreland from New CROP Seismic Data*. In: Finetti, I.R. (Ed.), CROP PROJECT: Deep Seismic Exploration of the Central Mediterranean and Italy. Chapter 26, 581-595.

Flemings P.B. and Jordan T.E. (1989). *A synthetic stratigraphic model of foreland basin development*. J. Geophys. Res., 94, B4, 3853-3866.

Frederiksen A.W. and Bostok M.G. (2000). *Modelling teleseismic waves in dipping*

anisotropic structures. Geophys. J. Int, 141, 401-412.

Geiss E. (1987). *A new compilation of crustal thickness data for the Mediterranean area*. Ann. Geophys., Ser. B, 5, 623-630.

Ghisetti F.C., Gorman A.R., Grasso M., Vezzani L. (2009). *Imprint of foreland structure on the deformation of a thrust sheet: The Plio-Pleistocene Gela Nappe (southern Sicily, Italy).* Tectonics, 28, TC4015, doi:10.1029/2008TC002385.

Godfrey N.J., Christensen N.I., Okaya D.A. (2002). *The effect of crustal anisotropy on reflector depth and velocity determination from wide-angle seismic data: A synthetic example based on South Island, New Zealand*. Tectonophysics, 355, 145-161.

Grad M., Tiira T., the ESC Working Group (2009). *The Moho depth map of the European Plate*. Geophys. J. Int., 176, 279-292, doi:10.1111/j.1365-246X.2008.03919.x.

Grasso M., Lentini F., Nairn A.E.M., Vigliotti L. (1983). *A geological and paleomagnetic study of the Hyblean volcanic rocks, Sicily.* Tectonophysics, 98, 271-295.

Grasso M., Behncke B., Di Geronimo I., Giuffrida S., La Manna F., Maniscalco R., Pedley H.M., Raffi S., Schmincke H.U., Strano D., Sturiale G. (2004). *Carta geologica del bordo nord-occidentale dell'Avampaese Ibleo e del fronte della Falda di Gela*. Firenze: S.EL.C.A.

Gvirtzman Z. and Nur A. (1999). *The formation of Mt Etna as a consequence of slab rollback*. Nature, 401, 782-785, doi:10.1038/44555.

Hobbs T. and Darbyshire F.A. (2012). *Point estimates of crustal thickness using receiver function stacking*. MSURJ, 7 (1), 21-27.

Hollenstein Ch., Kahle H.G., Geiger A., Jenny S., Geos S., Giardini D. (2003). *New GPS constraints on the Africa-Europe plate boundary zone in southern Italy*. Geophys. Res. Lett., 30 (18), 1935. doi:10.1029/2003GL017554.

Kind R. and Vinnik L.P. (1988). *The upper mantle discontinuities underneath the GRF array from P to S converted phases*. J. Geophys., 62, 138-147.

Kind R., Kosarev G.L., Petersen N.V. (1995). *Receiver functions at the stations of the German Regional Seismic Network (GRSN).* Geophys. J. Int., 121, 191-202.

Kosarev G.L., Makeyeva L.I., Vinnik L.P. (1987). *Inversion of teleseismic P-wave particle motions for crustal structure in Fennoscandia*. Phys. Earth Planet. Inter., 47, 11-24.

Kosarev G.L., Petersen N.V., Vinnik L.P., Roecker S.W. (1993). *Receiver functions for*

the Tien Shan analog broadband network: Contrasts in the evolution of structure across Talasso-Fergano Fault. J. Geophys. Res., 98, 4437-4448.

Kosarev G., Kind R., Sobolev S.V., Yuan X., Hanka W., Oreshin S. (1999). *Seismic evidence for a detached Indian lithospheric mantle beneath Tibet.* Science, 283, 1306-1309*,* doi: 10.1126/science.283.5406.1306.

Langston C.A. (1977*). The effect of planar dipping structure on source and receiver responses for constant ray parameter.* Bull. Seism. Soc. Am., 67, 1029-1050.

Langston C.A. (1979). *Structure under Mount Rainier, Washington, inferred from teleseismic body waves.* J. Geophys. Res., 84(B9), 4749-4762.

Lanzafame G. and Bousquet J.C. (1997). *The Maltese escarpment and its extension from Mt. Etna to Aeolian Islands (Sicily): importance and evolution of a lithospheric discontinuity.* Acta Vulcanologica, 9, 121-135.

Lavecchia G., Ferrarini F., De Nardis R., Visini F., Barbano M.S. (2007). *Active thrusting as a possible seismogenic source in Sicily (Southern Italy): Some insights from integrated structural-kinematic and seismological data.* Tectonophysics, 445, 145-167.

Levin V. and Park J. (1997). *P-SH conversions in a flat-layered medium with anisotropy of arbitrary orientation.* Geophys. J. Int., 131, 253-266.

Levin V. and Park J. (1998). *P-SH conversions in layered media with hexagonally symmetric anisotropy: A cookbook.* Pure Appl. Geophys., 151(2-4), 669-697.

Lickorish W.H., Grasso M., Butler R.W.H., Argnani A., Maniscalco R. (1999). *Structural styles and regional tectonic setting of the "Gela Nappe" and frontal part of theMaghrebian thrust belt in Sicily*. Tectonics, 18, 655-668, doi:10.1029/1999TC900013.

Ligorria J.P. and Ammon C.J. (1999). *Iterative deconvolution and receiver-function estimation.* Bull. Seismol. Soc. Am., 89, 1395-1400.

Lombardi D., Braunmiller J., Kissling E., Giardini D. (2008). *Moho depth and poissons ratio in the western central Alps from receiver functions.* Geophys. J. Int., 173, 249-264, doi:10.1111/j.1365-246X.2007.03706.x.

Longaretti G. and Rocchi S. (1990). *Il magmatismo dell'avampaese Ibleo (Sicilia orientale) tra il Trias e il Quaternario: dati stratigrafici e petrologici di sottosuolo*. Mem. Soc. Geol. It., 45, 911-925.

Lucente F.P., Piana Agostinetti N., Moro M., Selvaggi G., Di Bona M. (2005). *Possible fault plane in a seismic gap area of the Southern Apennines (Italy) revealed by*

receiver functions analysis. J. Geophys. Res., 110, doi:10.1029/2004JB003187.

Margheriti L., Pondrelli S., Piccinini D., Piana Agostinetti N., Giovani L., Salimbeni S., Lucente F.P., Amato A., Baccheschi P., Park J., Brandon M., Levin V., Plomerová J., Jedlicka P., Vecsey L., Babuska V., Fiaschi A., Carpani B., Ulbricht P. (2006). *RETREAT seismic deployment in the northern Apennines.* Ann. Geofis., 49(4/5).

Mele G. and Sandvol E. (2003). *Deep crustal roots beneath the northern Apennines inferred from teleseismic receiver functions.* Earth Planet. Sci. Lett., 211, 69-78.

Miller M.S. and Piana Agostinetti N. (2011). *Erosion of the continental lithosphere at the cusps of the Calabrian arc: evidence from S receiver functions analysis.* Geophys. Res. Lett., 38, http://dx.doi.org/10.1029/2011GL049455.

Miller M.S. and Piana Agostinetti N. (2012). *Insights into the evolution of the Italian lithospheric structure from S receiver function analysis.* Earth Planet. Sci. Lett., 345-348, 49-59.

Milne J. (1895). *Suggestion for a systematic observation in the northern hemisphere of earth waves and vibrations travelling great distances.* Circular Tokyo, 31 January 1895.

Morelli C., Bellemo S., Finetti I., de Visintini G. (1967). *Preliminary depth contour maps for the Conrad and Moho discontinuities in Europe.* Bol. Geofis. Teor. Appl., 9, 142-157.

Musumeci C., Patanè D., Scarfì L., Gresta S. (2005). *Stress directions and shear wave anisotropy: Observations from local earthquakes in southeastern Sicily (Italy).* Bull. Seismol. Soc. Am., 95, 1359-1374.

Nicolich R. and Dal Piaz G. (1991). *Isobate della Moho in Italia, in Structural Model of Italy, 6 fogli 1:500,000.* Progetto Finalizzato "Geodinamica" CNR, Rome.

Nicolich R., Laigle M., Hirn A., Cernobori, L., Gallart J. (2000). *Crustal structure of the Ionian margin of Sicily: Etna volcano in the frame of regional evolution*. Tectonophysics, 329, 121-140.

Owens T.J., Zandt G., Taylor S.R. (1984). *Seismic evidence for an ancient rift beneath the Cumberland Plateau, Tennessee: a detailed analysis of broadband teleseismic P waveforms.* J. Geophys. Res., 89, 7783-7795.

Owens T.J. and Zandt G. (1985). *The response of the continental crust-mantle boundary observed on broadband teleseismic receiver functions*. Geophys. Res. Lett., 12, 705-708.

Owens T.J., Taylor S.R., Zandt G. (1987). *Crustal structure at regional seismic test*

network stations determined from inversion of broadband teleseismic P waveforms. Bull. Seismol. Soc. Am., 77, 631-662.

Owens T.J. and Crosson R.S. (1988). *Shallow structure effects on broadband teleseismic P waveforms*. Bull. Seis. Soc. Am., 78(1), 96-108.

Park J., Yuan H., Levin V. (2004). *Subduction zone anisotropy beneath Corvallis, Oregon: A serpentinite skid mark of trench-parallel terrane migration?*. J. Geophys. Res., 109, B10306, doi:10.1029/2003JB002718.

Patacca E., Scandone P., Giunta G., Liguori V. (1979). *Mesozoic paleotectonic evolution of the Ragusa zone (South-eastern Sicily).* Geol. Romana, 18, 331-369.

Phinney R.A. (1964). *Structure of the Earth's crust from spectral behavior of long-period body waves.* J. Geophys. Res., 69(14), 2997-3017, doi:10.1029/JZ069i014p02997.

Piana Agostinetti N., Lucente F.P., Selvaggi G., Di Bona M. (2002). *Crustal Structure and Moho Geometry beneath the northern Apennines (Italy).* Geophys. Res. Lett., 29(20), 1999, doi:10.1029/2002GL015109.

Piana Agostinetti N., Park J., Lucente F.P. (2008). *Mantle wedge anisotropy in Southern Tyrrhenian subduction zone (Italy), from receiver function analysis.* Tectonophysics, 462, 35-48, doi:10.1016/j.tecto.2008.03.020.

Piana Agostinetti N. and Amato A. (2009). *Moho depth and V_P/V_S ratio in peninsular Italy from teleseismic receiver functions.* J. Geophys. Res., 114, B06303. doi:10.1029/2008JB005899.

Piana Agostinetti N. and Malinverno A. (2010). *Receiver function inversion by trans-dimensional Monte Carlo sampling.* Geophys. J. Int., 181, 2, 858-872.

Pondrelli S., Morelli A., Ekström G., Mazza S., Boschi E., Dziewonski A.M. (2002). *European-Mediterranean regional centroid-moment tensors: 1997-2000*. Phys. Earth Planet. Inter., 130, 71-101.

Pondrelli S., Morelli A., Ekström G. (2004). *European-Mediterranean regional centroid moment tensor catalog: solutions for years 2001 and 2002*. Phys. Earth Planet. Inter., 145 (1-4), 127-147.

Pontevivo A. and Panza G. (2002). *Group velocity tomography and regionalization in Italy and bordering areas.* Phys. Earth Planet. Inter., 134, 1-15, doi:10.1016/S0031-9201 (02)00079-1.

Ramesh D.S., Kind R., Yuan X. (2002). *Receiver function analysis of the North American crust and upper mantle.* Geophys. J. Int., 150, 91-108.

Reuther C.D., Ben-Avraham Z., Grasso M. (1993). *Origin and role of major strike-slip transfers during plate collision in the central Mediterranean*. Terra Nova, 5, 249-257.

Ryberg T. and Weber M. (2000). *Receiver function arrays: a reflection seismic approach*. Geophys. J. Int., 141, 1-11.

Sandvol E., Seber D., Barazangi M., Vernon F., Mellors R., Al-Amri A. (1998). *Lithospheric seismic velocity discontinuities beneath the Arabian shield.* Geophys. Res. Lett., 25, 2873-2876.

Saunders P., Priestley K., Taymaz T. (1998). *Variations in the crustal structure beneath western Turkey.* Geophys. J. Int., 134, 373-389.

Savage M.K. (1998). *Lower crustal anisotropy or dipping boundaries? Effects on receiver functions and a case study in New Zealand*. J. Geophys. Res., 103, 15.069-15.087.

Scarascia S., Lozej A., Cassinis R. (1994). *Crustal structures of the Ligurian, Tyrrhenian and Ionian seas and adjacent onshore areas interpreted from wide-angle seismic profiles*. Bol. Geofis. Teor. Appl., 36, 5-19.

Scarfì L., Giampiccolo E., Musumeci C., Patanè D., Zhang H. (2007). *New insights on 3D crustal structure in Southeastern Sicily (Italy) and tectonic implications from an adaptive mesh seismic tomography.* Phys. Earth Planet. Inter., 161, 74-85.

Suhadolc P. and Panza G. (1989). *Physical properties of the Lithosphere-asthenosphere system in Europe from geophysical data*. In: The Lithosphere in Italy, edited by A. Boriani et al., pp. 15-40, Acad. Naz. dei Lincei, Rome.

Tarantola A. (1987). *Inverse problem theory; methods for data fitting and model parameter estimation*. Elsevier, 613 pp.

Tomlinson J.P., Denton P., Maguire P.K.H., Booth D.C. (2006). *Analysis of the crustal velocity structure of the British isles using teleseismic receiver functions*. Geophys. J. Int., 167(1), 223-237, doi:10.1111/j.1365-246X.2006.03044.x.

von Rebeur-Paschwitz E. (1889). *The earthquake of Tokio, April 18, 1889*. Nature, 40, 294-295.

Waldhauser F., Kissling E., Ansorge J., Muller S. (1998). *Three-dimensional interface modeling with two-dimensional seismic data: The Alpine crust-mantle boundary*. Geophys. J. Int., 135, 264-278, doi:10.1046/j.1365-246X.1998.00647.x.

Yellin-Dror A., Grasso M., Ben Avraham Z., Tibor G. (1997). *The subsidence history of the northern Hyblean Plateau margin, southeastern Sicily*. Tectonophysics, 282, 277-

289.

Yuan X., Ni J., Kind R., Sandvol E., Mechie J. (1997). *Lithospheric and upper mantle structure of southern Tibet from a seismological passive source experiment*. J. Geophys. Res., 102, 27.491-27.500.

Yuan X., Sobolev S.V., Kind R., Oncken O., Bock G., Asch G., Graeber F., Hanka W., Wylegalla K., Tibi R., Haberland C., Rietbrock A., Giese P., Wigger P., Röwer P., Zandt G., Beck S., Wallace T., Pardo M., Comte D. (2000). *Subduction and collision processes in the Central Andes constrained by converted seismic phases*. Nature, 408(21), 958-961.

Yuan X., Sobolev S.V., Kind R. (2002). *Moho topography in the central Andes and its geodynamic implications*. Earth Planet. Sci. Lett., 199, 389-402.

Zandt G. and Ammon C.J. (1995). *Continental crust composition constrained by measurement of crustal Poisson's ratio*. Nature, 374, 152-154.

Zhang H. and Thurber C.H. (2003). *Double-difference tomography; the method and its application to the Hayward Fault, California*. Bull. seism. Soc. Am., 93(5), 1875-1889.

Zhang H. and Thurber C.H. (2005). *Adaptive mesh seismic tomography based on tetrahedral and Voronoi diagrams: application to Parkfield, California*. J. Geophys. Res., 110, B04303, doi:10.1029/2004JB003186.

Zhu L. and Kanamori H. (2000). *Moho depth variation in southern California from teleseismic receiver function*. J. Geophys. Res., 105, 2969-2980.

Appendix A-*Source parameters of teleseismic events used to compute RFs*

N	DATE (UTC)	Lat	Lon	H (km)	Mw
1	April 5, 2004 at 21:24:04	36.527	71.028	191.4	6.6
2	May 29, 2004 at 20:56:12	34.256	141.385	38.1	6.5
3	June 10, 2004 at 15:19:57	55.713	160.031	184.3	6.9
4	June 28, 2004 at 09:49:47	55.007	-134.378	15.5	6.8
5	July 25, 2004 at 14:35:18	-2.455	103.977	576.0	7.3
6	September 5, 2004 at 10:07:07	33.062	136.608	14.0	7.2
7	September 5, 2004 at 14:57:18	33.216	137.061	10.0	7.4
8	September 6, 2004 at 23:29:35	33.184	137.201	10.0	6.7
9	September 28, 2004 at 17:15:24	35.815	-120.374	7.9	6.0
10	October 8, 2004 at 14:36:06	13.954	120.533	105.0	6.5
11	October 9, 2004 at 21:26:53	11.424	-86.633	35.0	6.9
12	October 15, 2004 at 04:08:50	24.533	122.696	94.4	6.7
13	October 23, 2004 at 08:56:00	37.231	138.753	16.0	6.6
14	November 2, 2004 at 10:02:12	49.305	-128.781	10.0	6.7
15	November 8, 2004 at 15:55:01	24.059	122.548	29.0	6.3
16	November 15, 2004 at 09:06:56	4.679	-77.511	15.0	7.2
17	November 20, 2004 at 08:07:21	9.581	-84.228	16.0	6.4
18	November 21, 2004 at 11:41:07	15.699	-61.654	14.0	6.3
19	November 28, 2004 at 18:32:13	42.995	145.056	39.0	7.0
20	December 6, 2004 at 14:15:11	42.907	145.200	35.0	6.8
21	December 14, 2004 at 23:20:13	19.011	-81.348	10.0	6.8
22	December 26, 2004 at 00:58:53	3.307	95.947	30.0	9.0
23	December 26, 2004 at 04:21:29	6.910	92.958	39.0	7.1
24	January 1, 2005 at 06:25:44	5.093	92.313	11.7	6.6
25	January 12, 2005 at 08:40:03	-0.878	-21.194	10.0	6.8
26	January 19, 2005 at 06:11:36	34.064	141.491	28.0	6.6
27	February 16, 2005 at 20:27:52	-36.320	-16.558	10.0	6.6
28	February 22, 2005 at 02:25:22	30.735	56.901	14.0	6.4
29	February 26, 2005 at 12:56:50	2.933	95.522	23.2	6.8
30	March 20, 2005 at 01:53:41	33.795	130.108	10.0	6.6
31	March 28, 2005 at 16:09:36	2.074	97.013	30.0	8.7
32	April 10, 2005 at 10:29:11	-1.672	99.620	19.0	6.7
33	April 10, 2005 at 11:14:19	-1.714	99.779	30.0	6.5
34	May 05, 2005 at 19:12:21	5.710	-82.845	18.0	6.5
35	May 14, 2005 at 05:05:18	0.586	98.401	34.0	6.8
36	May 19, 2005 at 01:54:52	1.965	96.976	30.0	6.9
37	June 14, 2005 at 17:10:16	51.231	179.394	51.7	6.8
38	June 15, 2005 at 02:50:53	41.284	-125.983	10.0	7.2
39	June 17, 2005 at 06:21:41	40.758	-126.595	10.0	6.7
40	July 2, 2005 at 02:16:44	11.198	-86.411	27.0	6.6
41	July 5, 2005 at 01:52:02	1.836	97.034	21.0	6.7
42	July 23, 2005 at 07:34:57	35.506	139.933	65.6	6.0

N	DATE (UTC)	Lat	Lon	H (km)	Mw
43	July 24, 2005 at 15:42:06	7.909	92.139	135.0	7.3
44	August 16, 2005 at 02:46:28	38.251	142.059	36.0	7.2
45	September 26, 2005 at 01:55:39	-5.674	-76.409	127.4	7.5
46	October 8, 2005 at 03:50:40	34.493	73.629	26.0	7.6
47	October 15, 2005 at 15:51:07	25.321	123.356	183.0	6.5
48	October 19, 2005 at 11:44:43	36.383	140.833	41.5	6.4
49	November 14, 2005 at 21:38:51	38.101	144.925	11.0	7.0
50	November 19, 2005 at 14:10:14	2.220	96.763	30.0	6.5
51	November 27, 2005 at 10:22:19	26.784	55.847	10.0	6.0
52	December 2, 2005 at 13:13:09	38.122	142.118	29.0	6.5
53	December 5, 2005 at 12:19:57	-6.174	29.717	22.0	6.8
54	December 12, 2005 at 21:47:46	36.332	71.130	225.4	6.7
55	January 23, 2006 at 20:50:44.98	6.865	-77.790	14.0	6.2
56	February 22, 2006 at 22:19:07	-21.259	33.480	11.0	7.0
57	April 1, 2006 at 10:02:19	22.868	121.278	9.0	6.2
58	April 20, 2006 at 23:25:02	61.075	167.085	22.0	7.6
59	May 16, 2006 at 15:28:26	0.081	97.073	16.2	6.8
60	June 11, 2006 at 20:01:29	33.290	131.182	154.8	6.3
61	July 8, 2006 at 20:40:00	51.214	-179.312	22.0	6.6
62	September 30, 2006 at 17:50:23	46.360	153.152	11.0	6.6
63	October 1, 2006 at 09:06:02	46.470	153.236	19.0	6.6
64	November 15, 2006 at 11:14:16	46.616	153.224	28.5	8.3
65	November 15, 2006 at 11:34:58	46.666	155.310	10.0	6.5
66	December 1, 2006 at 03:58:21	3.427	99.069	205.0	6.4
67	December 26, 2006 at 12:26:21	21.818	120.534	10.0	7.2
68	December 26, 2006 at 12:34:14	22.023	120.539	10.0	7.0
69	January 13, 2007 at 04:23:20	46.272	154.455	10.0	8.1
70	March 6, 2007 at 03:49:41	-0.536	100.498	30.0	6.3
71	March 8, 2007 at 05:03:32	29.918	140.281	138.6	6.1
72	March 25, 2007 at 00:41:57	37.281	136.602	5.0	6.7
73	April 3, 2007 at 03:35:06	36.528	70.668	210.5	6.2
74	April 5, 2007 at 03:56:50	37.343	-24.613	14.0	6.3
75	April 7, 2007 at 07:09:26	37.344	-24.506	10.0	6.3
76	April 7, 2007 at 09:51:51	2.920	95.700	30.0	6.2
77	April 20, 2007 at 01:45:56	25.714	125.250	10.0	6.3
78	April 29, 2007 at 12:41:57	52.047	-179.985	117.0	6.2
79	May 4, 2007 at 12:06:52	-1.523	-14.869	10.0	6.2
80	May 16, 2007 at 08:56:18	20.473	100.701	38.1	6.3
81	May 30, 2007 at 20:22:12	52.144	157.313	115.8	6.4
82	June 2, 2007 at 21:34:58	23.013	101.054	10.0	6.2
83	June 13, 2007 at 19:29:41	13.613	-90.822	23.0	6.8
84	July 03, 2007 at 08:26:00	0.728	-30.254	10.0	6.3
85	July 16, 2007 at 01:13:22	37.570	138.478	10.0	6.6

N	DATE (UTC)	Lat	Lon	H (km)	Mw
86	July 16, 2007 at 14:17:37	36.785	134.883	350.7	6.8
87	July 21, 2007 at 13:27:03	-7.976	-71.130	632.9	6.1
88	July 25, 2007 at 23:37:32	7.084	92.588	24.5	6.2
89	July 31, 2007 at 22:55:31	-0.090	-17.780	11.0	6.2
90	August 2, 2007 at 02:37:42	47.180	141.770	5.0	6.2
91	August 2, 2007 at 03:21:42	51.340	-179.990	21.0	6.7
92	August 8, 2007 at 17:04:57	-5.960	107.650	280.0	7.5
93	August 15, 2007 at 20:22:13	50.568	-177.507	21.2	6.5
94	August 20, 2007 at 22:42:28	8.016	-39.267	10.0	6.6
95	September 03, 2007 at 16:14:54	45.829	150.027	99.6	6.2
96	September 06, 2007 at 17:51:27	24.334	122.324	62.9	6.5
97	September 10, 2007 at 01:49:11	2.945	-78.069	10.0	6.8
98	September 12, 2007 at 11:10:26	-4.517	101.382	30.0	8.4
99	September 12, 2007 at 23:49:01	-2.526	100.964	10.0	7.8
100	September 13, 2007 at 03:35:26	-2.223	99.564	10.0	7.1
101	September 13, 2007 at 16:09:09	-3.247	101.439	3.3	6.2
102	September 14, 2007 at 06:01:34	-4.108	101.220	35.0	6.4
103	September 19, 2007 at 07:27:51	-2.614	101.024	35.0	6.1
104	September 20, 2007 at 08:31:15	-2.040	100.204	35.0	6.7
105	October 02, 2007 at 18:00:08	54.581	-161.768	47.9	6.3
106	October 24, 2007 at 21:02:51	-3.909	101.061	30.0	6.8
107	October 25, 2007 at 13:50:01	46.057	154.114	6.2	6.1
108	November 16, 2007 at 03:13:00	-2.304	-77.793	119.0	6.7
109	November 29, 2007 at 19:00:19	14.951	-61.241	143.1	7.4
110	December 19, 2007 at 09:30:30	51.495	-179.473	56.3	7.2
111	December 21, 2007 at 07:24:35	51.346	-178.977	35.0	6.2
112	December 26, 2007 at 22:04:56	52.670	-168.271	35.0	6.3
113	January 05, 2008 at 11:01:05	51.299	-130.713	10.0	6.6
114	January 05, 2008 at 11:44:48	51.171	-130.556	10.0	6.4
115	January 09, 2008 at 08:26:45	32.341	85.146	10.0	6.4
116	January 09, 2008 at 14:40:01	51.701	-131.096	10.0	6.1
117	January 10, 2008 at 01:37:18	43.864	-127.310	10.0	6.3
118	January 22, 2008 at 17:14:57	1.011	97.436	20.0	6.1
119	February 08, 2008 at 09:38:14	10.733	-41.884	10.0	6.9
120	February 12, 2008 at 12:50:20	16.409	-94.165	99.6	6.4
121	February 20, 2008 at 08:08:31	2.751	95.966	34.3	7.5
122	February 21, 2008 at 02:46:18	77.051	18.349	10.0	6.1
123	February 24, 2008 at 14:46:24	-2.307	100.020	35.0	6.4
124	February 25, 2008 at 08:36:35	-2.352	100.018	35.0	7.0
125	February 25, 2008 at 18:06:05	-2.322	99.927	35.0	6.4
126	February 25, 2008 at 21:02:18	-2.233	99.828	25.0	6.6
127	March 03, 2008 at 02:37:27	-2.127	99.859	23.0	6.1
128	March 03, 2008 at 09:31:06	46.518	153.092	35.0	6.5

N	DATE (UTC)	Lat	Lon	H (km)	Mw
129	March 22, 2008 at 21:24:12	52.128	-178.587	132.4	6.2
130	March 29, 2008 at 17:30:51	2.910	95.282	32.4	6.3
131	April 15, 2008 at 03:03:10	13.660	-90.629	79.5	6.1
132	April 15, 2008 at 22:59:51	51.902	-179.365	10.0	6.4
133	April 16, 2008 at 05:54:19	51.908	-179.164	13.0	6.6
134	April 24, 2008 at 12:14:50	-1.139	-23.556	10.0	6.5
135	May 02, 2008 at 01:33:36	51.935	-177.595	14.0	6.6
136	May 07, 2008 at 16:02:05	36.216	141.449	35.0	6.2
137	May 07, 2008 at 16:16:38	36.261	141.700	35.0	6.1
138	May 07, 2008 at 16:45:20	36.137	141.446	35.0	6.8
139	May 12, 2008 at 06:28:00	31.104	103.270	10.0	7.8
140	May 20, 2008 at 13:53:38	51.270	178.723	47.1	6.3
141	May 23, 2008 at 19:35:35	7.261	-34.883	10.0	6.5
142	May 29, 2008 at 15:46:00	63.992	-21.014	10.0	6.3
143	June 01, 2008 at 01:57:22	20.115	121.317	22.4	6.3
144	June 13, 2008 at 23:43:46	39.103	140.668	10.0	6.8
145	June 22, 2008 at 23:56:30	67.729	141.249	18.0	6.1
146	June 27, 2008 at 11:40:14	11.005	91.850	17.0	6.6
147	June 28, 2008 at 12:54:46	10.851	91.703	16.6	6.3
148	July 05, 2008 at 02:12:04	53.892	152.884	633.3	7.7
149	July 13, 2008 at 14:58:32	21.020	121.100	10.0	6.3
150	July 19, 2008 at 02:39:30	37.615	142.115	27.0	7.0
151	July 23, 2008 at 15:26:20	39.807	141.467	111.0	6.8
152	July 24, 2008 at 01:43:17	50.967	157.559	35.0	6.4
153	August 10, 2008 at 08.20	11.050	91.840	10.0	6.2
154	August 25, 2008 at 13.21	30.890	83.610	12.0	6.7
155	August 26, 2008 at 21:00:36	-7.670	-74.391	153.0	6.4
156	August 27, 2008 at 01:35:32	51.620	104.135	16.0	6.2
157	August 28, 2008 at 15:22:24	-0.009	-17.421	16.2	6.3
158	September 10, 2008 at 13:08:14	8.091	-38.748	10.0	6.6
159	September 11, 2008 at 00:20:52	41.979	143.625	35.0	6.8
160	October 05, 2008 at 15:52:49	39.515	73.768	27.6	6.6
161	October 06, 2008 at 08:30:45	29.757	90.302	10.0	6.4
162	October 11, 2008 at 10:40:16	19.282	-64.832	25.8	6.1
163	October 16, 2008 at 19:41:26	14.432	-92.418	24.0	6.7
164	October 28, 2008 at 23:09:57	30.653	67.323	15.0	6.2
165	October 29, 2008 at 11:32:42	30.546	67.447	10.0	6.4
166	November 02, 2008 at 13:48:44	51.633	-174.379	51.4	6.1
167	November 10, 2008 at 01:22:01	37.588	95.834	19.0	6.3
168	November 19, 2008 at 06:11:22	8.295	-82.928	48.2	6.2
169	November 22, 2008 at 16:00:59	-4.344	101.243	10.0	6.3
170	November 22, 2008 at 18:49:43	-1.140	-13.896	10.0	6.2
171	November 24, 2008 at 09:02:58	54.194	154.315	491.6	7.3

N	DATE (UTC)	Lat	Lon	H (km)	Mw
172	December 20, 2008 at 10:29:22	36.603	142.356	10.0	6.5
173	January 08, 2009 at 19:21:34	10.197	-84.159	4.5	6.1
174	January 15, 2009 at 17:49:39	46.861	155.154	36.0	7.4
175	March 06, 2009 at 10:50:29	80.297	-2.046	10.0	6.5
176	March 12, 2009 at 23:23:34	5.636	-82.769	9.0	6.3
177	April 07, 2009 at 04:23:33	46.088	151.498	34.0	6.9
178	April 15, 2009 at 20:01:33	-3.091	100.496	8.5	6.2
179	April 18, 2009 at 19:17:59	46.118	151.364	35.0	6.6
180	April 21, 2009 at 05:26:11	50.793	155.050	149.5	6.2
181	May 03, 2009 at 16:21:47	14.585	-91.149	126.8	6.2
182	May 28, 2009 at 08:24:45	16.730	-86.209	10.0	7.3
183	June 05, 2009 at 02:17:04	41.858	143.399	41.6	6.3
184	June 16, 2009 at 20:05:57	-54.384	5.831	10.0	6.2
185	July 04, 2009 at 06:49:36	9.654	-78.983	43.1	6.0
186	July 06, 2009 at 14:53:12	50.487	176.982	22.0	6.1
187	July 07, 2009 at 19:11:45	75.325	-72.312	10.0	6.1
188	July 13, 2009 at 18:05:02	23.997	122.177	24.7	6.3
189	August 05, 2009 at 00:17:58	24.223	125.107	22.0	6.1
190	August 09, 2009 at 10.55.55	33.170	137.940	297.0	7.1
191	August 10, 2009 at 19.55.39	14.100	92.910	35.0	7.5
192	August 10, 2009 at 20.07.07	34.740	138.290	26.0	6.4
193	August 12, 2009 at 22.48.58	32.820	140.400	53.0	6.6
194	August 16, 2009 at 7:38:26	-1.480	99.490	20.0	6.7
195	August 17, 2009 at 0:05:00	23.500	123.500	20.0	6.7
196	August 17, 2009 at 10:10:57	23.420	123.470	10.0	6.1
197	August 20, 2009 at 6:35:03	72.220	0.970	6.0	6.0
198	August 28, 2009 at 01:52:06	37.721	95.684	10.0	6.2
199	September 03, 2009 at 13:26:18	31.128	130.051	161.5	6.2
200	September 12, 2009 at 20:06:25	10.757	-67.847	10.0	6.3
201	September 18, 2009 at 06:23:58	12.573	120.469	50.1	6.0
202	September 21, 2009 at 08:53:05	27.346	91.412	14.0	6.1
203	September 30, 2009 at 10:16:09	-0.725	99.856	81.0	7.6
204	October 01, 2009 at 01:52:29	-2.497	101.540	15.0	6.6
205	October 03, 2009 at 17:36:05	23.635	121.565	17.5	6.0
206	October 12, 2009 at 03:15:46	-17.200	66.602	10.0	6.1
207	October 13, 2009 at 05:37:28	53.132	-167.067	67.9	6.5
208	October 13, 2009 at 20:21:54	52.634	-167.149	13.7	6.4
209	October 16, 2009 at 09:52:52	-6.613	105.182	50.6	6.1
210	October 22, 2009 at 00:51:39	6.827	-82.576	10.0	6.2
211	October 29, 2009 at 17:44:31	36.434	70.731	205.6	6.2
212	October 30, 2009 at 07:03:39	29.154	129.903	35.0	6.8
213	November 10, 2009 at 02:48:45	8.090	91.881	10.8	6.0
214	November 17, 2009 at 15:30:46	52.151	-131.378	11.6	6.6

N	DATE (UTC)	Lat	Lon	H (km)	Mw
215	December 10, 2009 at 02:30:51	53.459	152.675	641.8	6.3
216	December 19, 2009 at 13:02:16	23.763	121.689	44.6	6.4
217	December 19, 2009 at 23:19:17	-10.110	33.814	15.2	6.0
218	December 23, 2009 at 01:11:57	-1.420	99.439	14.2	6.0
219	December 24, 2009 at 00:23:27	42.212	134.793	348.1	6.3
220	January 10, 2010 at 00:27:38	40.645	-124.763	21.7	6.5
221	January 12, 2010 at 21:53:09	18.451	-72.445	10.0	7.0
222	February 06, 2010 at 04:44:59	46.800	152.700	35.0	6.0
223	February 07, 2010 at 06:10:00	23.400	123.600	21.0	6.3
224	February 18, 2010 at 01:13:18	42.581	130.537	573.8	6.9
225	February 26, 2010 at 20:31:27	25.902	128.417	22.0	7.0
226	March 04, 2010 at 00:18:52	22.903	120.823	23.1	6.4
227	March 05, 2010 at 16:06:57	-4.032	100.806	22.0	6.5
228	March 14, 2010 at 08:08:05	37.780	141.562	39.0	6.5
229	March 25, 2010 at 05:29:31	13.744	120.069	72.4	6.0
230	March 30, 2010 at 16:54:47	13.609	92.884	41.7	6.6
231	April 06, 2010 at 22:15:02	2.360	97.132	31.0	7.7
232	April 13, 2010 at 23:49:37	33.271	96.629	10.0	6.9
233	April 26, 2010 at 02:59:51	22.241	123.709	22.0	6.5
234	April 30, 2010 at 23:11:44	60.644	-177.901	15.1	6.4
235	April 30, 2010 at 23:16:29	60.524	-177.728	15.7	6.0
236	May 03, 2010 at 10:27:45	29.614	141.064	82.3	6.1
237	May 05, 2010 at 16:29:03	-4.063	101.085	27.0	6.5
238	May 09, 2010 at 05:59:42	3.775	96.055	45.0	7.2
239	May 19, 2010 at 04:15:42	-5.069	-77.559	125.6	6.0
240	May 24, 2010 at 16:18:27	-8.095	-71.558	565.3	6.5
241	May 25, 2010 at 10:09:06	35.342	-35.940	10.0	6.3
242	May 26, 2010 at 08:53:08	25.796	129.956	10.0	6.4
243	May 31, 2010 at 19:51:48	11.119	93.698	127.7	6.4
244	June 12, 2010 at 19:26:50	7.748	91.938	35.0	7.5
245	June 13, 2010 at 03:32:54	37.405	141.602	7.7	6.1
246	July 04, 2010 at 21:55:51	39.705	142.523	23.7	6.4
247	July 18, 2010 at 05:56:44	52.861	-169.839	10.0	6.7
248	July 30, 2010 at 03:56:14	52.535	159.919	21.0	6.3
249	August 04, 2010 at 12:58:24	51.426	-178.607	27.0	6.4
250	August 04, 2010 at 23:48:02	45.964	153.216	33.6	6.0
251	August 12, 2010 at 11:54:16	-1.260	-77.312	211.0	7.1
252	August 16, 2010 at 03:30:53	-17.700	65.600	10.0	6.3
253	August 21, 2010 at 05:42:52	2.200	96.700	24.0	6.0
254	September 03, 2010 at 11:16:09	51.700	-175.900	58.0	6.5
255	September 17, 2010 at 19:21:15	36.438	70.787	220.4	6.2
256	October 04, 2010 at 13:28:39	24.268	125.149	35.0	6.3
257	October 08, 2010 at 03:26:13	51.421	-175.434	20.6	6.4

N	DATE (UTC)	Lat	Lon	H (km)	Mw
258	October 08, 2010 at 03:49:11	51.499	-175.261	35.0	6.1
259	October 25, 2010 at 14:42:22	-3.484	100.114	20.6	7.7
260	October 25, 2010 at 19:37:30	-2.984	100.391	22.9	6.1
261	October 25, 2010 at 22:59:53	-3.281	100.497	21.5	6.2
262	November 30, 2010 at 03:24:40	28.365	139.152	475.2	6.8
263	December 20, 2010 at 18:41:59	28.491	59.117	11.8	6.5
264	December 23, 2010 at 14:00:33	53.175	171.218	22.2	6.2
265	January 18, 2011 at 20:23:26	28.838	63.947	84.0	7.2
266	January 24, 2011 at 02:45:31	38.432	72.751	110.1	6.1
267	January 26, 2011 at 15:42:29	2.203	96.821	22.6	6.1
268	January 27, 2011 at 08:38:28	28.185	58.968	10.7	6.0
269	January 29, 2011 at 06:55:26	70.965	-6.778	9.5	6.1
270	February 04, 2011 at 13:53:47	24.616	94.740	88.8	6.4
271	March 09, 2011 at 02:45:20	38.510	142.792	14.1	7.2
272	March 09, 2011 at 18:16:14	38.378	142.506	22.0	6.1
273	March 09, 2011 at 18:44:35	38.502	143.199	23.0	6.0
274	March 09, 2011 at 21:22:18	38.385	142.642	23.0	6.1
275	March 11, 2011 at 05:46:23	38.322	142.369	24.4	8.9
276	March 11, 2011 at 06:06:11	39.025	142.316	25.1	6.4
277	March 11, 2011 at 06:07:21	36.401	141.862	35.4	6.4
278	March 11, 2011 at 06:15:40	36.186	141.192	35.0	6.8
279	March 11, 2011 at 06:25:50	38.106	144.553	19.7	7.1
280	March 11, 2011 at 06:48:47	37.993	142.764	22.3	6.3
281	March 11, 2011 at 06:57:14	35.758	140.992	30.2	6.3
282	March 11, 2011 at 07:14:59	36.648	141.811	25.0	6.3
283	March 11, 2011 at 07:25:33	37.916	144.621	15.0	6.1
284	March 11, 2011 at 07:28:12	36.802	141.911	24.0	6.1
285	March 11, 2011 at 08:12:04	36.606	141.557	19.8	6.2
286	March 11, 2011 at 08:15:40	37.034	144.612	27.8	6.2
287	March 11, 2011 at 08:19:24	36.200	142.000	19.9	6.5
288	March 11, 2011 at 08:31:07	37.428	141.200	25.0	6.1
289	March 11, 2011 at 10:10:34	39.248	142.779	28.9	6.0
290	March 11, 2011 at 11:36:39	39.276	142.521	11.6	6.5
291	March 11, 2011 at 15:13:14	35.997	141.796	18.9	6.2
292	March 11, 2011 at 18:59:15	37.037	138.355	10.0	6.2
293	March 11, 2011 at 19:02:58	39.372	142.900	24.8	6.1
294	March 11, 2011 at 19:46:49	40.472	139.070	10.0	6.6
295	March 11, 2011 at 20:11:22	39.025	142.645	8.7	6.3
296	March 12, 2011 at 01:34:10	38.748	142.853	24.5	6.0
297	March 12, 2011 at 01:46:20	37.354	141.998	25.4	6.2
298	March 12, 2011 at 01:47:16	37.588	142.682	24.8	6.8
299	March 12, 2011 at 10:53:30	39.075	142.352	24.9	6.1
300	March 12, 2011 at 13:15:41	37.261	141.175	37.5	6.4

N	DATE (UTC)	Lat	Lon	H (km)	Mw
301	March 12, 2011 at 17:19:23	36.573	142.645	4.3	6.0
302	March 12, 2011 at 22:12:46	37.662	141.959	14.3	6.3
303	March 12, 2011 at 23:24:50	37.981	141.849	24.8	6.1
304	March 13, 2011 at 01:26:07	35.742	141.731	24.5	6.2
305	March 13, 2011 at 02:23:37	36.354	142.287	24.9	6.2
306	March 13, 2011 at 11:37:31	37.348	142.416	24.8	6.0
307	March 14, 2011 at 06:12:36	37.800	142.500	14.0	6.0
308	March 15, 2011 at 13:27:56	37.500	142.200	28.0	6.0
309	March 15, 2011 at 13:31:46	35.200	138.500	9.0	6.0
310	March 15, 2011 at 15:23:54	40.300	143.200	19.0	6.1
311	March 17, 2011 at 04:13:56	40.140	142.150	29.0	6.2
312	March 19, 2011 at 09:56:51	36.810	140.375	24.9	6.1
313	March 22, 2011 at 07:18:47	37.249	143.956	26.5	6.6
314	March 22, 2011 at 09:19:05	37.334	141.861	27.0	6.4
315	March 22, 2011 at 09:44:29	39.863	143.436	15.5	6.6
316	March 22, 2011 at 13:31:28	-33.085	-15.979	11.9	6.1
317	March 22, 2011 at 15:03:46	35.786	141.572	16.4	6.1
318	March 24, 2011 at 08:21:01	39.120	142.155	36.8	6.1
319	March 24, 2011 at 13:55:12	20.705	99.949	10.0	6.8
320	March 25, 2011 at 11:36:24	38.763	141.942	39.2	6.4
321	March 27, 2011 at 22:23:58	38.402	142.102	17.1	6.1
322	March 29, 2011 at 10:54:33	37.417	142.269	13.8	6.1
323	March 30, 2011 at 05:29:55	36.135	142.433	30.3	6.0
324	March 31, 2011 at 07:15:30	38.954	142.017	39.6	6.2
325	April 07, 2011 at 13:11:24	17.431	-93.978	167.4	6.5
326	April 07, 2011 at 14:32:41	38.253	141.640	49.0	7.1
327	April 09, 2011 at 12:57:49	30.013	131.810	21.3	6.1
328	April 11, 2011 at 08:16:13	37.007	140.477	13.1	7.1
329	April 11, 2011 at 23:08:16	35.406	140.542	13.1	6.2
330	April 12, 2011 at 05:07:42	37.000	140.700	10.6	6.0
331	April 13, 2011 at 19:57:23	39.587	143.357	11.2	6.1
332	April 21, 2011 at 01:54:41	40.306	143.629	7.0	6.0
333	April 21, 2011 at 13:37:03	35.617	140.452	42.9	6.1
334	April 23, 2011 at 10:12:48	39.164	142.892	38.9	6.0
335	April 30, 2011 at 08:19:16	6.800	-82.300	8.0	6.2

N=identification number assigned to each event. Date in Coordinate Universal Time (UTC). Latitude and longitude are preceded by a minus sign if south of the equator or west of the prime meridian. H=depth (in kilometers) of hypocenter. Mw=moment magnitude. See text for other details.